Università degli studi di Padova

Dipartimento di Fisica e Astronomia "Galileo Galilei"

Corso di Laurea Magistrale in Fisica

Gravitational Lensing by Vector Perturbations

Relatori:
Prof. Sabino Matarrese (UNIPD),
Prof. Carlo R. Contaldi (ICL), Prof. Alan Heavens (ICL)

Laureanda: Arianna Renzini

Anno Accademico 2015/2016

Declaration of Intent

Our intent is to investigate the physics of gravitational lensing by vector type perturbations in cosmology and if possible shed some light on their observability, as little has been said in the past.
In order to do so, we first outline the fundamentals of gravitational lensing in the context of General Relativity, and present insightful mathematical tools in the weak lensing limit. Then, we review cosmological perturbation theory, and examine the decomposition of spacetime perturbations into scalar, vector and tensor components. We find that the Kerr metric, which pertains to a rotating mass in asymptotically flat space, may add a vector type perturbation to the flat case, and thus study in detail gravitational lensing in Kerr. We obtain a lensing map and carefully define its validity; then, we apply the tools mentioned above in the Kerr spacetime to gauge the effects rotation may have on light bending.
At this point, we explore possible Kerr-like lenses in the sky, such as rotating galaxies, and discuss to what extent our map may describe lensing around such objects. We predict the magnitude of the effect galaxy rotation may have on background lensing and compare this to lens survey data to ultimately assess whether it may be observable.

Contents

Chapter 1

Review of Gravitational Lensing

1.1 Introduction to Gravitational Lensing

At the core of the revolution brought about by Einstein's theory of General Relativity is the notion that energy, i.e. matter, curves space and time. One of the many effects of this phenomenon is that the trajectories of free falling massive and massless particles (geodesics) cannot be straight lines in the proximity of a body. Thus, light travelling through space is bent according to the mass distribution it encounters. This is known as gravitational lensing.

Ever since the mathematical description of lensing, astrophysicists have been using it to map our Universe more precisely and to infer properties of the universe such as the nature and distribution of massive objects. Truly, nothing we observe from Earth is exactly where we see it, as no path in space can ever be perfectly straight; hence, if we can figure out what type of distortions have been impressed on an image of a specific light source, we learn a lot about what lies between us and the source. Vice versa, if we consider a well known massive body and observe lensing around it, it is then possible to map out the true positions of the light sources on the background.

Figure 1.1: Image from the NASA/ESA Hubble Space Telescope of the galaxy cluster MACS J1206. Note the strong lensing of the background galaxies.

There are different approaches to the study of gravitational lensing, depending mainly on whether the effect is *weak* and can be analysed as a statistical effect, or *strong*. Look at Figure 1.1: given a picture of the sky, weak lensing effects will invariably be present, but only careful data analysis can reveal whether there is a global behaviour which may be indicative of a specific mass distribution between observer and lens. Strong lensing on the other hand is immediately recognisable, as the background is heavily warped; this effect can only arise when lensing mass and background objects are almost perfectly aligned, and thus is quite rare to observe. In extreme cases, light from the same source may propagate past the mass on several different paths which come around different sides of the lens giving rise to multiple images of the source.

We will review the relativistic calculations which describe the effect in the simplest setup possible, using the Schwarzschild spacetime. We will then outline the vast field of weak gravitational lensing highlighting the tools we'll need in subsequent chapters.

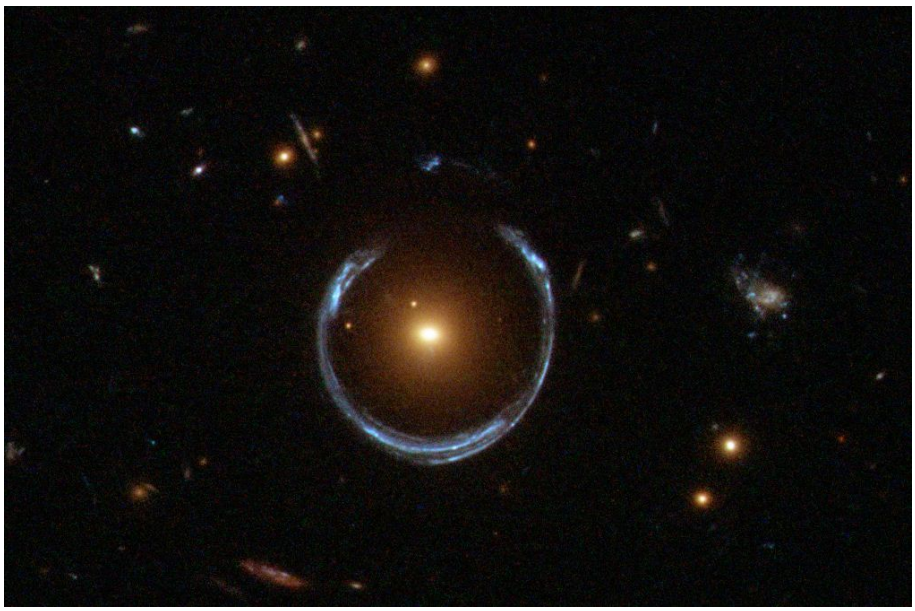

Figure 1.2: In this photo, taken with the Hubble Space Telescope's Wide Field Camera 3, the gravity of the luminous red galaxy LRG $3-757$ has distorted the light from a much more distant blue galaxy. This phenomenon is known as *Einstein ring*, as it was first predicted by Albert Einstein in 1936, in a paper published on *Science*. In this paper he also stated that

> *There is no hope of observing this phenomenon directly. First, we shall scarcely ever approach closely enough to such a central line. Second, the angle* [spanned by the ring] *will defy the resolving power of our instruments.*
>
> – *Science*, vol 84 p 506, 1936

We are all very glad he was wrong.

1.2 Lensing in the Schwarzschild Solution

We review the Schwarzschild solution to Einstein's equations and the trajectories of massless particles in this spacetime, to familiarise ourselves with the formalism and more importantly as it will be of great use later, to compare it with a more complicated scenario. We will use geometric units ($c = G = 1$) throughout.

The Schwarzschild metric is [1]

$$ds^2 = -\left(1 - \frac{2m}{r}\right) dt^2 + \left(1 - \frac{2m}{r}\right)^{-1} dr^2 + r^2 \left(d\theta^2 + \sin^2\theta \, d\phi^2\right) \ ; \tag{1.1}$$

it constitutes the unique, maximally symmetric, static solution to Einstein's equations:

$$G_{\mu\nu} \equiv R_{\mu\nu} - \frac{g_{\mu\nu}}{2} R = 8\pi \, T_{\mu\nu} \ . \tag{1.2}$$

Note that $r = 2m$ is a coordinate singularity and is associated with the event horizon of a black hole of mass m, whereas $r = 0$, origin of coordinates, is a spacetime singularity. The spacetime is asymptotically flat.

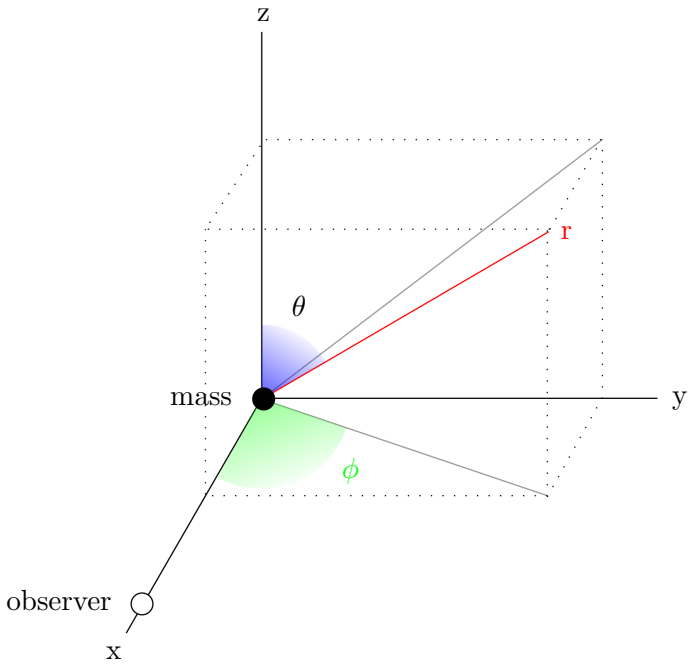

Figure 1.3: Spherical polar coordinates.

Consider now a static, spherically symmetric mass m sitting on a point O in space: outside the mass, spacetime is described by the Schwarzschild metric 1.1, choosing O as the origin of the coordinate system, as per Birkhoff's theorem. Define a generic, affinely parametrised worldline

$$x^\mu(\tau) = (t(\tau), r(\tau), \theta(\tau), \phi(\tau)) \ ,$$

where we've chosen spherical polar coordinates. τ is in general an affine parameter; we will take it to be equal to the proper time of the observer, and dotting in this chapter designates

derivatives with respect to proper time to avoid complications. Since the metric is diagonal and $t-$ and $\phi-$ independent, it is quite straightforward, starting from the Lagrangian

$$\mathcal{L} = g_{\mu\nu}\frac{dx^\mu}{d\tau}\frac{dx^\nu}{d\tau} \ , \tag{1.3}$$

to write down the equations of motion for each coordinate. The most efficient way to do this is recognising the four Killing vectors of this spacetime, namely

$$k_t^\mu = \begin{pmatrix}1\\0\\0\\0\end{pmatrix} \ , \quad L_1^\mu = \begin{pmatrix}0\\0\\\sin\phi\\\frac{\cos\phi}{\tan\theta}\end{pmatrix} \ , \quad L_2^\mu = \begin{pmatrix}0\\0\\\cos\phi\\-\frac{\sin\phi}{\tan\theta}\end{pmatrix} \ , \quad L_3^\mu = \begin{pmatrix}0\\0\\0\\1\end{pmatrix} \ , \tag{1.4}$$

and working out the conserved charges associated to them. One could alternatively write down the geodesic equations, but these would be second order in τ, so needlessly complicated. k_t is the time-like Killing vector, and as such is associated to the energy

$$E = -k_{t\,\mu}\dot{x}^\mu \ , \tag{1.5}$$

while the conserved charges associated to the space-like Killing vectors arise from rotation invariance, and are then the three components of angular momentum $\vec{L}$. One can always choose a frame of reference such that

$$\vec{L} = \begin{pmatrix}L_{1\,\mu}\,\dot{x}^\mu\\L_{2\,\mu}\,\dot{x}^\mu\\L_{3\,\mu}\,\dot{x}^\mu\end{pmatrix} = \begin{pmatrix}0\\0\\l\end{pmatrix} \ , \tag{1.6}$$

which implies

$$\dot{t} = E\left(1-\frac{2m}{r}\right)^{-1} \ , \qquad \dot{\theta} = 0 \ , \qquad \dot{\phi} = \frac{l}{r^2} \ . \tag{1.7}$$

The equation for $r(\tau)$ is then derived from the normalisation condition on the 4-velocity

$$g_{\mu\nu}\dot{x}^\mu\dot{x}^\nu = \epsilon = \begin{cases}0, & m = 0\\-1, & m \neq 0\end{cases} \ , \tag{1.8}$$

and is (for the massless case)

$$\dot{r} = \pm\sqrt{E^2 - \left(1-\frac{2m}{r}\right)\frac{l^2}{r^2}} \ . \tag{1.9}$$

The sign of $\dot{r}$ depends on whether one considers an incoming or an outgoing ray with respect to the mass.
We interpret 1.7 and 1.9 as follows: the time coordinate t isn't a constant of the motion, as its variation is proportional to r divided by the radial distance from $2m$ (as per equation 1.7). Intuitively, this implies that the proper time of a stationary observer flows more slowly the closer they are to the Schwarzschild radius, and vice versa faster when they are further away.[1] When $r \to \infty$, $\dot{t} \to E$, which is just the Minkowski space limit: $\frac{dt}{d\tau} = \gamma = E$ for a test mass [2]. The two angular coordinates behave quite differently: ϕ changes with

[1] Assuming the observer lies outside the horizon.

a rate which is inversely proportional to the distance squared, which means that the light ray bends more and more as it approaches the mass, and less and less as it travels on towards the observer; θ on the other hand is a constant of the motion, thus the whole trajectory $x^i(\tau)$ lies on a fixed plane.

It's worth to fully appreciate this aspect of the Schwarzschild spacetime as it is the only one with this feature. Let us consider light source, lensing mass and observer as point masses in empty space, and take the trajectory of a single photon that leaves the light source along a certain direction, is lensed by the mass, and reaches the observer. Assume both the observer and the light source to be in the asymptotically flat region, and further that the distance of closest approach r_0 of the photon to the mass is much larger than m, in order to use Euclidean geometrical axioms. since the metric is totally symmetric, there is no preferential plane with respect to the mass so one can always choose the plane on which $x^i(\tau)$ lies and reduce the analysis to $2D$. For obvious reasons, this must be the plane containing both the source of light rays and the observer, plus the point P where the lines tangent to the trajectory at the source and at the observer meet - this will appear clearer in Figure 1.4; these three points identify one and one only plane. Note that even in the completely general case in which light source, mass and observer aren't aligned this

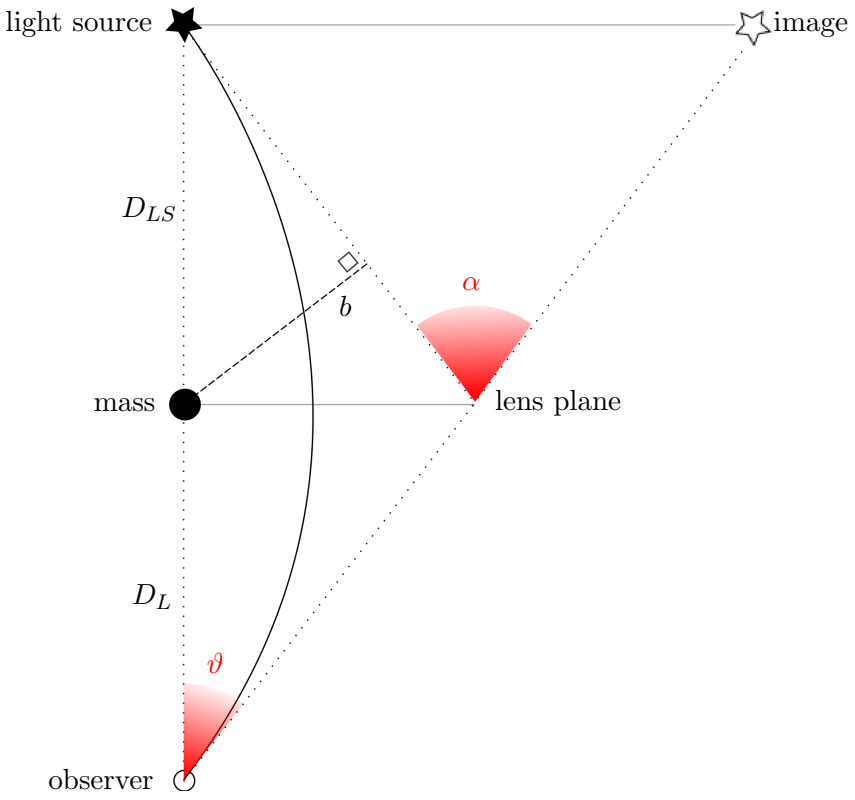

Figure 1.4: Simple example of gravitational lensing in the Schwarzschild spacetime: in this set-up, observer, mass and source are aligned, and the distances between observer and mass (D_L) and mass and light source (D_{LS}) are equal. Note that this last condition is not unreasonable, as the void distribution in our Universe is approximately uniform, so an object in the foreground lensing a light source in the background will probably be roughly equidistant from us and the source.

special plane will necessarily contain the mass itself. To see this, one must forget about the observer (in fact, the latter plays no role in the lensing at all) and realise that all the possible planes of motion are the infinite planes passing through the mass and light source.

Consider the set-up of Figure 1.4: supposing the mass m which appears in the metric 1.1 to be known, one can work out the bend angle α using the equations of motion above. In fact, the total variation of the ϕ coordinate along the geodesic will be [3]

$$\Delta\phi = 2\int_{\phi_1}^{\phi_2} d\phi = 2\int_{\infty}^{r_0} \frac{d\phi}{dr} dr = 2\int_{\infty}^{r_0} \frac{\dot{\phi}}{\dot{r}} dr \ , \tag{1.10}$$

if we consider the source to be at $r \to \infty$, and introduce the distance of closest approach r_0. The latter is defined to be the distance at which $\dot{r}$ changes sign, so

$$r_0 = r(s_0) \mid \dot{r}(s_0) = 0 \quad \to \quad r_0 = \frac{l}{E}\sqrt{1 - 2\frac{m}{r_0}} \tag{1.11}$$

using 1.9. It's important to point out that $r_0 \to \frac{l}{E}$ as $m \to 0$, which is the flat spacetime limit. Then, in flat space $r_0 \equiv \frac{l}{E} \equiv b$, where b is simply the impact parameter associated to the motion. One may extend this result to the Schwarzschild spacetime and define the *apparent impact parameter* [4]

$$b \equiv \left|\frac{l}{E}\right| \ ; \tag{1.12}$$

so 1.11 is effectively a relation between b and r_0 in the Schwarzschild spacetime.
The total bend angle α is simply

$$\alpha = 2\int_{\infty}^{r_0} \left|\frac{\dot{\phi}}{\dot{r}}\right| dr - \pi = 2\int_{\infty}^{r_0} \left(r^2\sqrt{\frac{1}{b^2} - \left(1 - \frac{2m}{r}\right)\frac{1}{r^2}}\right)^{-1} dr - \pi \ , \tag{1.13}$$

once we've substituted 1.7, 1.9 and 1.12 into the left hand side. Note that we're integrating from ∞, as we consider the source to be at a distance $D \gg r_0$, $D \to \infty$ from the lens. This integral may be solved by expanding the integrand in a convenient variable, and then performing a direct integration on every independent term. To do this, first we write down an expression for the distance of closest approach r_0 as a function of the impact parameter by inverting 1.11 (for details see [4], pp. 144-145):

$$r_0 = \frac{2\,b}{\sqrt{3}} \cos\left[\frac{1}{3}\cos^{-1}\left(-\frac{3^{3/2}\,m}{b}\right)\right] \ , \tag{1.14}$$

which expanded in $\frac{m}{b}$ yields

$$r_0 = b\left[1 - \frac{m}{b} - \frac{3}{2}\left(\frac{m}{b}\right)^2 - 4\left(\frac{m}{b}\right)^3 - \frac{105}{8}\left(\frac{m}{b}\right)^4 - 48\left(\frac{m}{b}\right)^5 + \mathcal{O}\left(\frac{m}{b}\right)^6\right] \ . \tag{1.15}$$

The choice of $\frac{m}{b}$ as an expansion parameter is quite natural: we assume the impact parameter to be much larger than the Schwarzschild radius $2m$, i.e. the coordinate singularity of the metric 1.1. The same goes for the parameter $h = \frac{m}{r_0}$, as previously mentioned,

which we will use to expand the integral 1.13. Following the procedure in [3], we substitute 1.11 in 1.13 and change variable to $x = \frac{r_0}{r}$ to obtain

$$\alpha = 2\int_0^1 \frac{dx}{\sqrt{1-2h-x^2+2h\,x^3}} - \pi \ ; \tag{1.16}$$

now we expand the integrand in h and integrate with the help of **Wolfram *Mathematica*** to obtain

$$\alpha = 4h + h^2\left(-4+\frac{15\pi}{4}\right) + h^3\left(\frac{122}{3}-\frac{15\pi}{2}\right) + h^4\left(-130+\frac{3465\pi}{64}\right) + \mathcal{O}(h^5)\ . \tag{1.17}$$

We prefer to express the bend angle as an expansion in $\frac{m}{b}$, since (we will see) b can be very easily rewritten as a function of observable angles. Then, substituting 1.15 in 1.17 and expanding in $\frac{m}{b}$ we obtain

$$\alpha = 4\left(\frac{m}{b}\right) + \frac{15\pi}{4}\left(\frac{m}{b}\right)^2 + \frac{128}{3}\left(\frac{m}{b}\right)^3 + \frac{3465\pi}{64}\left(\frac{m}{b}\right)^4 + \frac{3584}{5}\left(\frac{m}{b}\right)^5 + \mathcal{O}\left(\frac{m}{b}\right)^6 \ , \tag{1.18}$$

which is commonly known as the Schwarzschild series [5].

Given an observation of α, in the special case that the source, the lens and the observer are aligned, we can test General Relativity or estimate the mass of the lens. A historically valuable example of the former are Arthur Eddington's measurements of star positions during the solar eclipse in May 1919. On the other hand, we can identify the alignment of lens and light source due to the presence of *Einstein rings* around the lensing body, and via relativistic calculations, it is possible to estimate the mass of the lens. An Einstein ring is given by the deformation of light from a background galaxy or star into the shape of a ring around the lensing mass, as may be seen in Figure 1.2.

Of course, it is uncommon to observe perfectly aligned lenses and sources; the more typical case is shown in 1.5, where the light source is slightly misaligned with respect to the mass and observer. As mentioned before, we can work in two dimensions on the plane passing through the mass, the source and the observer as this will necessarily be the plane on which the trajectory lies.
Note that in Figure 1.5 the point P doesn't lie on the lens plane anymore, and a displacement d occurs between the intersections of the tangents to the motion and the lens plane - this will be key in our analysis. Further note that the light source subtends an angle β on the observer's sky, which is a priori unknown but can be written as a function of the observable angle ϑ, as we will see; thus it is possible, using the equations of motion, to trace the light ray back to the point of origin and map the position of the light source in the sky, from the point of view of the observer. To do this, we follow [6].
We work out the displacement d as a function of the geometry; use Figure 1.6 for reference. Let us choose an arbitrary coordinate system: we pick an (xy) plane, or "equatorial plane", different from the motion plane, and take the x axis to be the optical axis. The reason for this choice will become apparent in section 3, where we generalise the geometry to a case where the motion does not occur on a single plane.
Project d and the angles of interest onto the equatorial plane and the vertical (xz) plane. Notice how the tangents to the motion intersect the lens plane in points A and B, and

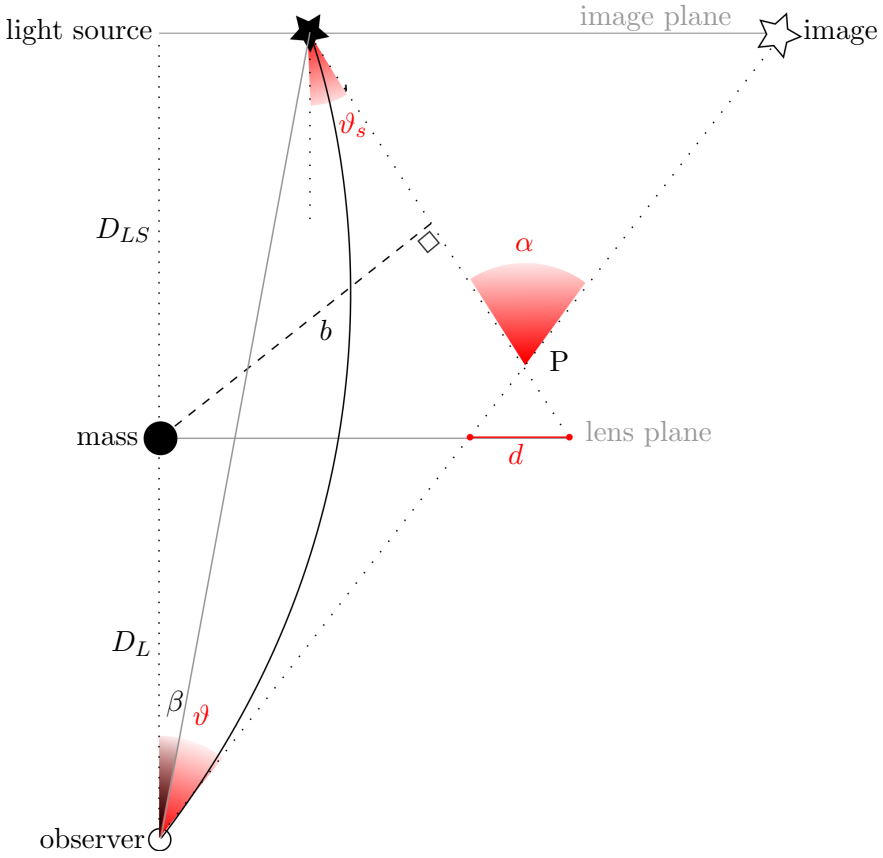

Figure 1.5: Lensing with displacement in the Schwarzschild spacetime.

d lies entirely on the motion plane. The components of A and B in this particular frame are

$$\begin{aligned} A_x &= 0 \ , & A_y &= D_L \tan\vartheta \cos\varphi \ , & A_z &= D_L \tan\vartheta \sin\varphi \ ; \\ B_x &= 0 \ , & B_y &= A_y + q\, d_y \ , & B_z &= A_z + q\, d_z \ . \end{aligned} \tag{1.19}$$

$q = \pm 1$ is a necessary sign as these expressions depend on whether P lies on the observer's side of the lens plane, or on the opposite side. Looking at Figure 1.5, we see that

$$\alpha = \vartheta + \vartheta_s \ , \tag{1.20}$$

and thus q depends on whether $\vartheta \gtrless \vartheta_s$, specifically

$$q = \begin{cases} +1, & \vartheta > \vartheta_s \\ -1, & \vartheta < \vartheta_s \end{cases} \ . \tag{1.21}$$

We can read off the equation for d from the motion plane:

$$d = q\left(D_L \tan\beta + D_{LS} \tan\vartheta_s - D_L \tan\vartheta\right) \ , \tag{1.22}$$

where β is the unknown angle spanned by the light source on the observer's sky. We now need a lens equation that will give us β as a function of the observable angles on the

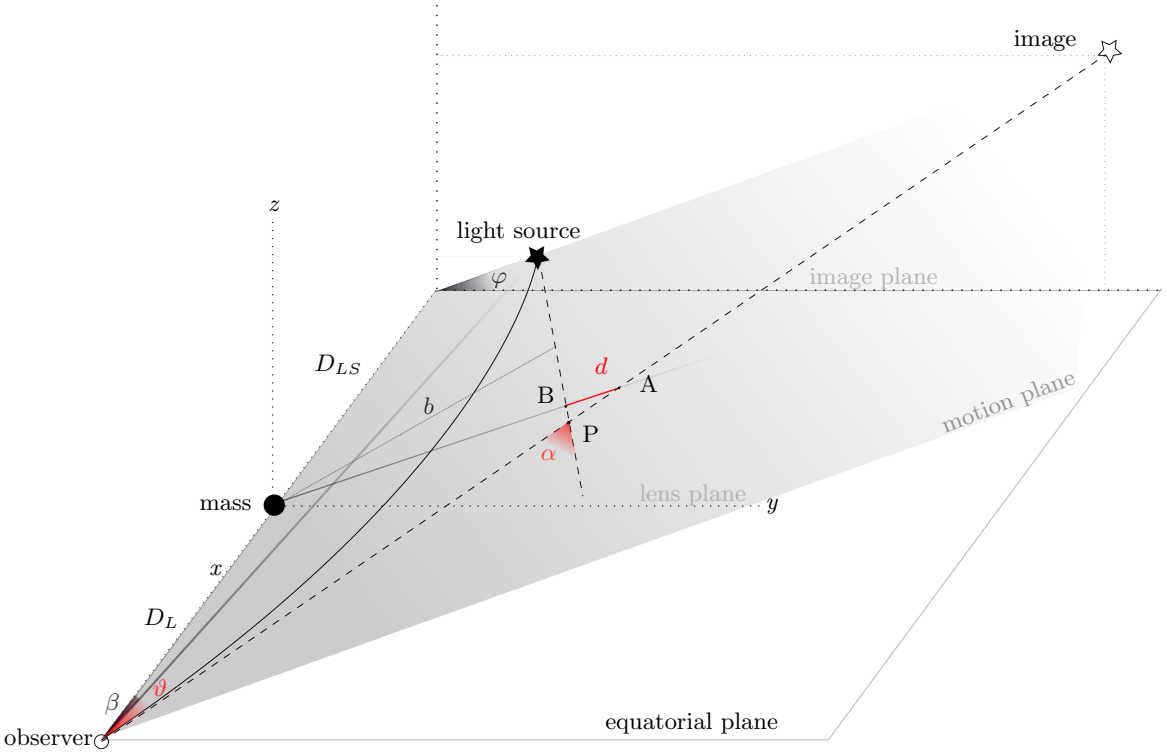

Figure 1.6: $3D$ view of lensing in the Schwarzschild metric.

motion plane.

Writing down an exact lens equation is tricky, even in this simple case; see [7] for a quick review of exact and approximate equations. [6] references a specific lens equation from [7] which we can motivate briefly.
Consider the impact parameter b; it may be defined arbitrarily with respect to the incoming or outgoing tangents to the ray, and in the asymptotic approximation [2] the incoming and outgoing impact parameters will have the same value. The outgoing impact parameter is simply $b = D_L \sin\vartheta$, and if we equate this to the incoming impact parameter drawn in Figure 1.5 we can easily derive a lens equation using Pythagoras' Theorem a number of times:

$$D_S \tan\beta = D_L \frac{\sin\vartheta}{\cos\vartheta_s} - D_{LS} \tan\vartheta_s \ . \tag{1.23}$$

Then, substituting in 1.22 one obtains

$$d = D_L \sin\vartheta \left[\frac{1}{\cos\vartheta_s} - \frac{1}{\cos\vartheta}\right] \ , \tag{1.24}$$

which, projecting in the frame of Figure 1.6, simply decomposes in

$$d_y = D_L \sin\vartheta \cos\varphi \left[\frac{1}{\cos\vartheta_s} - \frac{1}{\cos\vartheta}\right] \ , \qquad d_z = D_L \sin\vartheta \sin\varphi \left[\frac{1}{\cos\vartheta_s} - \frac{1}{\cos\vartheta}\right] \ . \tag{1.25}$$

[2] The asymptotic approximation implies taking $r \to \infty$ both backwards and forwards along the motion.

Thus, remembering the relation between ϑ and ϑ_s 1.20, one obtains an expression for the displacement as a function of the two observable angles ϑ and φ which pinpoint the position of the image with respect to the observer, and of the angle α which we've calculated integrating geodesics in Schwarzschild 1.18. Note how all the relativistic aspects of the geometry have been encapsulated in the angle α; asymptotic flatness is key to use Euclidean geometry and thus obtain the lens equation above.

1.3 Weak Lensing

The general field of weak gravitational lensing encompasses all those lensing effects that can only be measured statistically, averaging across multiple lenses [8]. We'll briefly review how these are commonly treated, and will ultimately focus on the distorting effects brought about by inhomogeneous matter distributions.

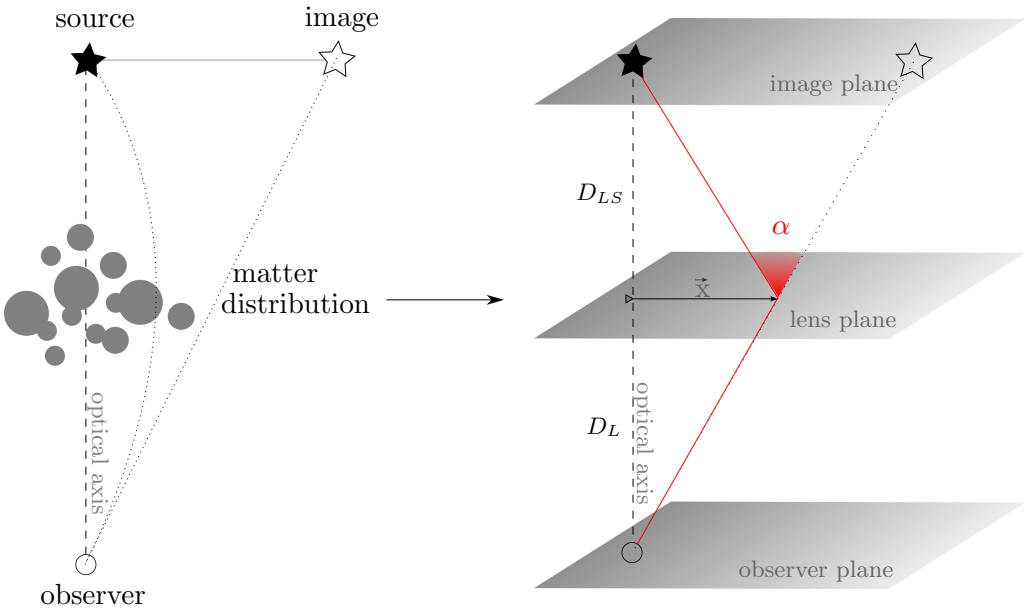

Figure 1.7: Weak lens approximation.

Consider a matter distribution along the observer's line of sight, as in Figure 1.7. If the matter is localised such that the physical distances between the lenses is negligible compared to the distance between observer and lens (D_L), lens and source (D_{LS}), as is usually the case in our universe (i.e. galaxy clusters, etc...), then effectively the deflection occurs in a very short section of the light path; we can then assume the matter distribution to be planar and use the so-called *thin lens approximation* [9]. Then, the lens is fully described by the surface density of the distribution

$$\Sigma(\boldsymbol{x}) = \int \rho(\boldsymbol{x}, z)\, dz \ , \tag{1.26}$$

where $\boldsymbol{x}$ is a two-dimensional vector on the lens plane. Let us truncate the expansion 1.18 at first order, taking the bend angle by a single mass to be

$$\alpha = \frac{4m}{b} \ ; \tag{1.27}$$

we can then extend this formula to the general case of a planar mass distribution by integrating on the lens plane [10]. Consider the contribution of an infinitesimal part of the surface mass $dm = \Sigma(\boldsymbol{y})\, d^2y$ to the bend angle, $\boldsymbol{y} \in$ *lens plane*; note that the impact parameter with respect to dm is $|\boldsymbol{x} - \boldsymbol{y}|$, so the integrated bend angle is

$$\boldsymbol{\alpha}(\boldsymbol{x}) = 4\, D_L \int \Sigma(\boldsymbol{y})\, \frac{(\boldsymbol{x} - \boldsymbol{y})}{|\boldsymbol{x} - \boldsymbol{y}|^2}\, d^2y \tag{1.28}$$

and is a function of the position $\boldsymbol{x}$, where the light ray intersects the lens plane.

The geometry represented on the right hand side of Figure 1.7 is just like that in Figure 1.4; then, just as before, we can look at the general case where the source is not aligned with the optical axis - the geometry will simply be that of Figure 1.5. In this first order approximation in the observable angles, the displacement d is negligible and we simply take $\boldsymbol{x} = \boldsymbol{\beta} D_L$, and then $|\boldsymbol{x}| \approx b$, as $\sin \boldsymbol{\beta} \approx \boldsymbol{\beta}$. Note how we've made $\boldsymbol{\beta}$ a two dimensional angle: it corresponds to the direction of the incoming ray in $3D$ space, and is measured with respect to the optical axis. Also, from 1.20 we get $\alpha \approx \beta_s$ and the lens equation 1.23 reduces to

$$D_S\, \boldsymbol{\vartheta} = D_L\, \boldsymbol{\beta} - D_{LS}\, \boldsymbol{\alpha} \ , \tag{1.29}$$

which is a simple, explicit equation that relates image position and source position. It's useful to further simplify it by rescaling the bend angle,

$$\tilde{\boldsymbol{\alpha}} = \frac{D_{LS}}{D_S}\, \boldsymbol{\alpha} \ , \tag{1.30}$$

and considering the distances $D_S \approx D_L$; thus leaving us with [10]

$$\boldsymbol{\vartheta} = \boldsymbol{\beta} - \tilde{\boldsymbol{\alpha}} \ . \tag{1.31}$$

Note how this equation does not have a unique solution; in fact, gravitational lensing may produce effects such as multiple images and Einstein rings as mentioned before.

Lensing Potential. It is useful to associate a potential-like function to the mass distribution, and rewrite the bend angle as a result of its action. To do this, simply look at the integral expression for α 1.28; firstly, it's useful to rewrite the various ingredients as functions of observable angles, as we will be taking derivatives with respect to these: the infinitesimal mass $dm = D_L^2\, \Sigma(\boldsymbol{\gamma})\, d^2\gamma$, and the relative impact parameter $D_L\, |\boldsymbol{\beta} - \boldsymbol{\gamma}|$. We also combine 1.28 with 1.30 to work with adimensional quantities; thus the integral expression for the re scaled bend angle is

$$\tilde{\boldsymbol{\alpha}}(\boldsymbol{\beta}) = 4\, \frac{D_{LS} D_L}{D_S} \int \Sigma(\boldsymbol{\eta})\, \frac{(\boldsymbol{\beta} - \boldsymbol{\eta})}{|\boldsymbol{\beta} - \boldsymbol{\eta}|^2}\, d^2\eta \equiv \boldsymbol{\nabla} \Phi(\boldsymbol{\beta}) \ , \quad \text{where} \tag{1.32}$$

$$\Phi(\boldsymbol{\theta}) = 4\, \frac{D_{LS} D_L}{D_S} \int \Sigma(\boldsymbol{\eta}) \ln\left(|\boldsymbol{\beta} - \boldsymbol{\eta}|\right)\, d^2\eta \tag{1.33}$$

is the *lensing potential* of a thin lens.
Taking the Laplacian of $\Phi(\boldsymbol{\beta})$ we get a scalar quantity:

$$\nabla^2 \Phi(\boldsymbol{\beta}) = 8\pi\, \frac{D_{LS} D_L}{D_S}\, \Sigma(\boldsymbol{\beta}) = 2\, \frac{\Sigma(\boldsymbol{\beta})}{\Sigma_c} \equiv 2\, \kappa(\boldsymbol{\beta}) \ , \quad \text{where} \tag{1.34}$$

$$\Sigma_c \equiv \frac{1}{4\pi}\frac{D_S}{D_{LS}D_L} \tag{1.35}$$

is the *critical surface density*. 1.34 is the $2D$ Poisson equation, which proves itself extremely useful when estimating the surface mass density of a lens from lensing measurements.

Distortion Matrix. Up to now, we've shown how a mass distribution modifies the path travelled by light emitted by a point source. Of course, all sources are extended in nature, and their image will not only be shifted, but also distorted by the lens. Ultimately, it is the distortion of the lensed image that gives us precious insight about the mass distribution along the line of sight: spotting correlations between the shapes and orientations of background sources is the typical way astrophysicists put these tools we're reviewing to good use.
All the information regarding the distortion of an infinitesimal source is contained in the Jacobian of the lens equation

$$\mathcal{D}_{ij} = \frac{\partial \vartheta_i}{\partial \beta_j} \ , \tag{1.36}$$

which is known as the *distortion matrix*.
Taking now 1.31 and rewriting it with explicit $\boldsymbol{\beta}$ dependence:

$$\boldsymbol{\theta}(\boldsymbol{\beta}) = \boldsymbol{\beta} - \boldsymbol{\nabla}\Phi(\boldsymbol{\beta}) \ , \tag{1.37}$$

we get a simple expression for $\mathcal{D}$

$$\mathcal{D}_{ij} = \delta_{ij} - \frac{\partial^2 \Phi}{\partial\beta_i\,\partial\beta_j} \ . \tag{1.38}$$

The $\mathcal{D}$ associated to 1.31 is evidently symmetric, and has thus $4-1=3$ degrees of freedom. These degrees are associated to two distinct fields: the scalar field κ (namely, the convergence) and the $2-$dimensional vector field $\boldsymbol{\gamma}$, which quantifies shear. We can thus classify the nature of distortion, distinguishing between the two effects as shown in Figure 1.8.
The distortion matrix is easily decomposed in diagonal and traceless parts, and we can identify the components of κ and γ_i in the thin lens approximation:

$$\mathcal{D}_{ij} = \begin{pmatrix} 1-\kappa & 0 \\ 0 & 1-\kappa \end{pmatrix} + \begin{pmatrix} -\gamma_1 & -\gamma_2 \\ -\gamma_2 & \gamma_1 \end{pmatrix} \ , \quad \boldsymbol{\gamma} = \begin{pmatrix} \gamma_1 \\ \gamma_2 \end{pmatrix} \ . \tag{1.39}$$

Note that in the weak lensing regime, both $|\kappa|$ and $|\gamma_i|$ are subcritical, typically $\ll 1$. The traceless part of the distortion matrix $\mathcal{D}$ constitutes the shear tensor Γ.

One can repeat this decomposition with a more complicated lens equation; in general, the distortion matrix won't be symmetric. The asymmetric contribution will result in a rotation of the image, and it may be quantified by the parameter ρ [11]. We can summarise all this by rewriting the distortion matrix as

$$\mathcal{D}_{ij} = \begin{pmatrix} 1-\kappa-\gamma_1 & -\gamma_2-\rho \\ -\gamma_2+\rho & 1-\kappa+\gamma_1 \end{pmatrix} \ . \tag{1.40}$$

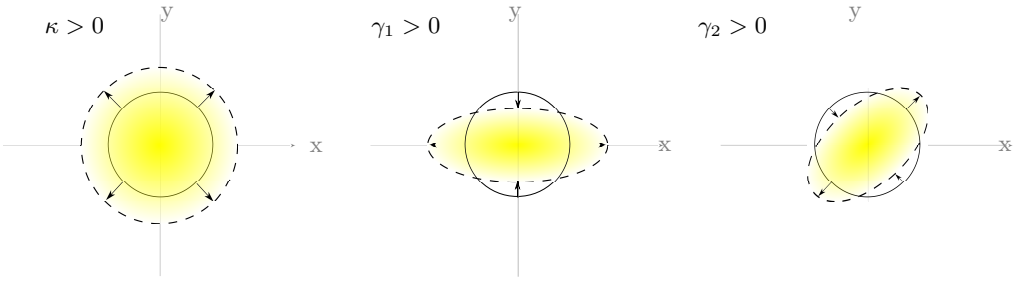

Figure 1.8: The effect of the convergence and shear fields on an image. $\kappa > 0\,(< 0)$ induces an isotropic expansion (contraction) of the image; $\gamma_1 > 0\,(< 0)$ stretches (contracts) the image along x and contracts (stretches) it along y, $\gamma_2 > 0\,(< 0)$ does the same along the $x = \pm y$ directions.

E- and B- Mode Decomposition in Weak Lensing. Typically, weak lensing can only account for dilation and shearing effects, characterised by their symmetry around the lens. In general, not all distortions will be symmetric, so it's convenient to catalogue them into different types; this is often done via the so-called E- and B- *mode* decomposition, where the E-mode is an effect brought about by the shear field $\boldsymbol{\gamma}$, and the B-mode encompasses all distortions that are not symmetric around the lens - see Figure 1.9 as an example.

To give the reader an overview of the subject, we will introduce the general notions of E- and B- modes of the shear field on the celestial sphere, following Bartelmann's review [12].
Let us introduce the orthonormal coordinate basis on the sphere $\{e_1,\, e_2\}$:

$$e_1 = \partial_\theta \ , \qquad e_2 = \sin^{-1}\theta\, \partial_\phi \ ; \tag{1.41}$$

from this basis, one can construct the helicity basis $\{e_+,\, e_-\}$:

$$e_\pm = \frac{1}{\sqrt{2}} \left(e_1 \pm i\, e_2\right) \ . \tag{1.42}$$

Now look at the symmetric, traceless, rank-2 tensor field Γ expressed in 1.39,

$$\Gamma = \begin{pmatrix} -\gamma_1 & -\gamma_2 \\ -\gamma_2 & \gamma_1 \end{pmatrix} \ ; \tag{1.43}$$

this tensor field defines the spin-(± 2) fields $p_{\pm 2}$,

$$p_{\pm 2} := \left(\Gamma_{ij}\, \theta^i \otimes\, \theta^j\right)\, (e_\pm, e_\pm) = \frac{1}{2}\left(\gamma_1 \pm i\gamma_2\right) \ . \tag{1.44}$$

Thus, these fields may be decomposed into spin-(± 2) spherical harmonics,

$$p_{\pm 2} = \sum_{l,\,m} p_{\pm 2,\, l,\, m}\, {}_{\pm 2}Y_{l,\,m} \ , \tag{1.45}$$

where $p_{\pm 2,\, l,\, m}$ are the expansion coefficients, and ${}_{\pm 2}Y_{l,\,m}$ are the *spin-weighted spherical harmonics*, defined by the differential equation

$$\nabla_\pm \left({}_sY_{l,\,m}\right) = \sqrt{\frac{(l \pm s)\,(l \mp s + 1)}{2}}\, {}_{s\pm 1}Y_{l,\,m} \tag{1.46}$$

such that

$$\nabla_{\pm}^2 \left(Y_{l,m}\right) = \frac{1}{2}\sqrt{\frac{(l+2)!}{(l-2)!}}\, {}_{\pm 2}Y_{l,m} \ , \qquad \nabla_+ \nabla_- Y_{l,m} = -\frac{l\,(l-1)}{2}\, Y_{l,m} \ . \tag{1.47}$$

$\nabla_\pm$ takes the divergence of the argument with respect to $e_\pm$, respectively.
Then, one may define the spin-0 fields

$$q_\pm := \nabla_\pm^2\, p = \frac{1}{2}\sum_{l,\,m} p_{\pm 2,\,l,\,m}\sqrt{\frac{(l+2)!}{(l-2)!}}\, Y_{l,\,m} \ , \tag{1.48}$$

which will be independent of the orientation of the coordinate frame in which they are measured. We may call the expansion coefficients

$$q_{\pm,\,l,\,m} := \frac{1}{2}\, p_{\pm 2,\,l,\,m}\sqrt{\frac{(l+2)!}{(l-2)!}} \ . \tag{1.49}$$

Let us show how one can use these to define parity-conserving and parity-changing modes of the field: if the system undergoes the parity transformation $\{e_1,\, e_2\} \to \{e_1,\, -e_2\}$, it appears clear looking at the Γ tensor that this implies

$$\gamma_1 \to \gamma_1 \ , \qquad \gamma_2 \to -\gamma_2 \tag{1.50}$$

for the shear field. The $\gamma_{1,\,2}$ components may be combined from the spin-± 2 fields $p_{\pm 2}$ turning 1.44 around,

$$\gamma_1 = p_2 + p_{-2} \ , \qquad \gamma_2 = -i\,(p_2 - p_{-2}) \ ; \tag{1.51}$$

hence the following linear combinations of the spherical harmonic coefficients

$$a_{E,\,l,\,m} = -(p_{2,\,l,\,m} + p_{-2,\,l,\,m}) \ , \qquad a_{B,\,l,\,m} = -i\,(p_{2,\,l,\,m} - p_{-2,\,l,\,m}) \tag{1.52}$$

identify an E-mode, which conserves parity, and a B-mode which changes it. The terminology arises from the similarity with the electric and magnetic fields, as the former is a gradient field and as such is invariant under parity changes, whereas the latter isn't as it constitutes a curl field.
Substituting 1.49 into 1.52 one obtains

$$a_{E,\,l,\,m} = -2\sqrt{\frac{(l+2)!}{(l-2)!}}\,(q_{+,\,l,\,m} + q_{-,\,l,\,m}) \ , \tag{1.53}$$

$$a_{B,\,l,\,m} = -2i\sqrt{\frac{(l+2)!}{(l-2)!}}\,(q_{+,\,l,\,m} - q_{-,\,l,\,m}) \ ; \tag{1.54}$$

then we can build the E- and B- modes

$$E = \sum_{l,\,m} a_{E,\,l,\,m}\, Y_{l,\,m} \ , \qquad B = \sum_{l,\,m} a_{B,\,l,\,m}\, Y_{l,\,m} \ . \tag{1.55}$$

Now let us see what happens to these coefficients in the weak lensing case. From [12] we know that

$$p_{\pm 2} = \nabla_{\mp}^2\, \Phi \ , \tag{1.56}$$

where Φ is the lensing potential introduced previously. Let us take this result without further motivation, and refer the reader to Bartelmann's review for a complete derivation. We may decompose Φ in spherical harmonics,

$$\Phi = \sum_{l,m} \Phi_{l,m} Y_{l,m} \ ; \tag{1.57}$$

then, using the previous relations shown for spherical harmonics, we find

$$\nabla^2_{\pm} \Phi = \frac{1}{2} \sum_{l,m} \sqrt{\frac{(l+2)!}{(l-2)!}} \Phi_{l,m} {}_{\mp 2}Y_{l,m} \ , \tag{1.58}$$

which, comparing with 1.45, yields

$$p_{\pm 2,l,m} = \frac{1}{2} \sqrt{\frac{(l+2)!}{(l-2)!}} \Phi_{l,m} \ . \tag{1.59}$$

This implies, remembering equation 1.52, that $a_{B,l,m} \equiv 0$, as there is a degeneracy in the spin; so weak lensing alone can't create a B-mode distortion pattern.
So, since weak lensing isn't expected to give rise to B-modes, their presence in cosmological surveys is typically taken to be a symptom of some non-lensing contamination. However, we've seen we can generally expect a rotation field ρ to appear in the distortion matrix, which breaks its symmetry. This is of principal interest for us and we'll be investigating the ρ field of a particular lens in Chapter 3.

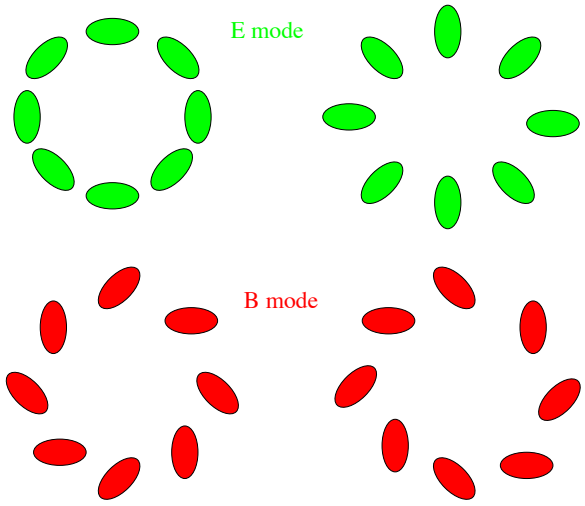

Figure 1.9: An illustration of possible E- and B- type patterns, borrowed from [13]. Note the axial symmetry of the E-mode, and asymmetry of the B-mode.

Chapter 2

Cosmological Perturbation Theory and Vector Perturbations

2.1 Introduction to Perturbation Theory

Cosmological perturbation theories have been developed primarily to describe structure formation and evolution in the universe as a result of primordial density fluctuations. The linear perturbation analysis of spatially homogeneous and isotropic cosmological models was pioneered by Lifshitz in 1946, and was then revisited and extended in the following years by numerous scientists; for a detailed historical overview, we recommend Kodama and Sasaki's Cosmological Perturbation Theory paper, [14].
Perturbation theories are an invaluable tool for cosmologists and are as such widely used for a variety of purposes. Ultimately, the observation of cosmological perturbations in our Universe is the most direct approach we have to explore early physics, before last scattering. In fact, the primary application of perturbation theory is the study of anisotropies in the Cosmic Microwave Background, which are traced back to higher redshifts, $z \gg 1100$, and the consequences these have on large-scale structure. They are also a key element when it comes to fixing initial conditions for numerical simulations of structure formation.

In the context of General Relativity, it is straightforward to associate energy density fluctuations with perturbations of the spacetime metric: a perturbation of the metric has a direct effect on the Einstein tensor $G_{\mu\nu}$ which, through the Einstein equations 1.2, affects the energy-momentum tensor $T_{\mu\nu}$. We will write down explicitly the equations which link metric perturbations to the energy they carry.

Let us follow the Kodama-Sasaki review of cosmological perturbation theory and lay out the formalism for this section. Consider a 4-dimensional spatially homogeneous and isotropic spacetime, i.e. the *Robertson-Walker* spacetime, which is described by the metric

$$ds^2 = g_{\mu\nu}\, dx^\mu\, dx^\nu = -dt^2 + a(t)^2\, d\Sigma(x^i)^2 \ , \tag{2.1}$$

where $d\Sigma(x^i)^2$ is the time independent metric of 3-dimensional space,

$$d\Sigma^2 = \gamma_{ij}\, dx^i\, dx^j = \frac{dr^2}{1 - k\, r^2} + r^2\, d\Omega_2^2 \ , \tag{2.2}$$

k is the curvature of the spacetime and $d\Omega_2^2$ is the metric on the 2-sphere. $k = 0$ corre-

sponds to a flat universe, $k = +/- 1$ to a curved closed/open universe. As usual, Latin indices run from 1 to 3, Greek indices from 1 to 4. The Riemann curvature tensor of the 3-dimensional subspace is given by

$$R_{ijkl} = k\,(\gamma_{ik}\,\gamma_{jl} - \gamma_{il}\,\gamma_{jk}) \quad , \tag{2.3}$$

as the space is maximally symmetric [1]. The Ricci tensor and scalar follow,

$$R_{ij} = 2\,k\,\gamma_{ij} \quad , \qquad R = 6\,k \quad . \tag{2.4}$$

The plan is to perturb this spacetime, which is generally considered to be a good model for our Universe, keeping the curvature k constant. On this spacetime, it is possible to expand perturbations by harmonic functions and reduce their evolution equations to a set of decoupled, ordinary differential equations, as we will show.
We choose conformal time η as time coordinate to simplify notation,

$$d\eta = \frac{dt}{a(t)} \quad ; \tag{2.5}$$

it is implied that components of vectors and tensors are from now on in the coordinates (η, x^i).

By choosing a maximally symmetric background spacetime, we restrict the energy-momentum tensor $T_{\mu\nu}$ to take the following form:

$$T_{\mu\nu} = (\rho + p)\,u_\mu\,u_\nu + p\,g_{\mu\nu} \quad , \tag{2.6}$$

where ρ and p are solely time dependent functions and are typically associated with the density and pressure of a perfect fluid, and u_μ is the 4-velocity [15].

Let us quickly mention a much-debated issue which arises naturally when approaching spacetime perturbations: gauge invariance. In fact, a change of coordinates affects the spacetime metric and may both generate fictitious *gauge modes* and remove real perturbations [16]. Generally speaking, there are two (related) solutions to the gauge problem, namely either the fixing of a particular gauge or the definition of special gauge-invariant perturbations (*Bardeen variables*). In our analysis, we will choose a gauge and keep track of all metric perturbations.

In this thesis, we aren't particularly concerned with the evolution of density fluctuations and their cosmological implications - our intent here is to review the decomposition of perturbations into scalar, vector and tensor modes and concentrate on the vector type components, as they have been somewhat overlooked in the past.

2.2 Perturbation Decomposition into Scalar, Vector, and Tensor Contributions

The classification of perturbations comes naturally when observing how these react under space coordinate transformations, $x^i \to \tilde{x}^i$; they may have scalar, vector or tensor behaviour. Let us see what this entails.

We work on the 3-dimensional totally symmetric space described by the metric $d\Sigma^2$ in 2.2. A vector $\boldsymbol{v}$ on this space may be decomposed into its own divergence and a divergenceless part,

$$\boldsymbol{v} = \boldsymbol{v}_v + \nabla v_s \ , \qquad \boldsymbol{\nabla} \cdot \boldsymbol{v}_v = 0 \ ; \tag{2.7}$$

we write the elliptic equation

$$\Delta v_s = \nabla \cdot \boldsymbol{v} \ , \qquad \text{where } \Delta = \gamma^{ij}\nabla_i\nabla_j \ , \tag{2.8}$$

which defines the quantity v_s[1]. Thus, we have decomposed $\boldsymbol{v}$ into scalar part v_s and vector part $\boldsymbol{v}_v$ in accordance with how these transform under coordinate changes.
The same can be done for a second rank tensor $\boldsymbol{S}$. Note that we only need to consider symmetric tensors, as the Einstein equations 1.2 cancel out the antisymmetric parts. Then,

$$S^{ij} = S_t^{ij} + \left(\nabla^i\nabla^j s - \frac{1}{3}\gamma^{ij}\Delta s\right) + \left(\nabla^j S_v^i + \nabla^i S_v^j\right) + \frac{1}{3}\mathrm{Tr}(\boldsymbol{S})\,\gamma^{ij} \ ; \tag{2.9}$$

where we have

$$s = \frac{3}{2}\,\Delta^{-1}\,(\Delta + 3\,k)^{-1}\,\left(\nabla_i\nabla_j S^{ij} - \frac{1}{3}\,\Delta\mathrm{Tr}(\boldsymbol{S})\right) \ , \tag{2.10}$$

$$S_v^i = (\Delta + 2\,k)^{-1}\,\left(\delta^i{}_j - \nabla^i\Delta^{-1}\nabla_j\right)\,\left(\nabla_m S^{jm} - \frac{1}{3}\,\nabla^j\mathrm{Tr}(\boldsymbol{S})\right) \ , \tag{2.11}$$

with

$$\mathrm{Tr}(\boldsymbol{S}_t) = 0 \ , \qquad \nabla_j S_t^{ij} = 0 \ . \tag{2.12}$$

As before, we call $\boldsymbol{S}_t$ the tensor type, $\boldsymbol{S}_v$ the vector type, and $(s, \mathrm{Tr}(\boldsymbol{S}))$ the scalar type components of $\boldsymbol{S}$.

In a Robertson-Walker spacetime and with certain constraints, scalar, vector, and symmetric second-rank tensor equations may be decomposed into groups, each of which contains components of only one type. This is true when the equations are covariant with respect to coordinate changes in the 3−dimensional subspace $d\Sigma^2$, linear at most in unknown geometrical quantities and second order at most in the case of differential equations. We provide a revised proof of this in Appendix A. In this case, it is possible to study the three types separately: scalar, vector and tensor perturbations.

It is well known that scalar quantities can be expanded in a complete set of harmonic functions, $Q^{(0)}(\boldsymbol{x})$, satisfying [17]

[1]Note: on our chosen space, 2.8 has a unique solution [14].

$$\Delta\, Q^{(0)} = -\mathsf{k}^2\, Q^{(0)} \ ; \tag{2.13}$$

evidently, $-\mathsf{k}^2$ is an eigenvalue of the Laplace operator Δ on the 3-dimensional subspace, and it takes continuous values when $k \leq 0$ and discrete values when $k > 0$, as shown in [18].
The same can be done for vector modes,

$$\Delta\, Q_i^{(1)} = -\mathsf{k}^2\, Q_i^{(1)} \ , \qquad \text{with } \boldsymbol{\nabla} \cdot \boldsymbol{Q}^{(1)} = 0 \ , \tag{2.14}$$

and tensor modes,

$$\Delta\, Q_{ij}^{(2)} = -\mathsf{k}^2\, Q_{ij}^{(2)} \ , \qquad \text{with } \nabla^i\, Q_{ij}^{(2)} = 0 \ . \tag{2.15}$$

Consider equations 2.7 and 2.9; one can construct vector and symmetric tensor modes from the scalar modes simply by setting

$$\boldsymbol{Q}^{(0)} = -\frac{1}{\mathsf{k}} \boldsymbol{\nabla}\, Q^{(0)} \ , \tag{2.16}$$

$$Q_{ij}^{(0)} = \frac{1}{\mathsf{k}^2} \left(\nabla^i \nabla^j - \frac{1}{3} \gamma^{ij} \Delta \right) Q^{(0)} = \left(\frac{1}{\mathsf{k}^2} \nabla^i \nabla^j + \frac{1}{3} \gamma^{ij} \right) Q^{(0)} \ , \tag{2.17}$$

remembering 2.13. One can also construct tensors from vector modes,

$$Q_{ij}^{(1)} = \frac{1}{\mathsf{k}} \left(\nabla_i\, Q_j^{(1)} + \nabla_j\, Q_i^{(1)} \right) \ . \tag{2.18}$$

Perturbing the metric. As we've pointed out before, the three types of perturbations totally decouple dynamically and may be studied independently; furthermore, due to the homogeneity and isotropy of the 3-dimensional subspace, the expansion coefficients of harmonic functions with different eigenvalues don't mix, so there is no need to sum over the eigenvalues. Let us now perturb the metric 2.1, and call the perturbed metric $\tilde{g}_{\mu\nu}$ such that

$$\tilde{g}_{\mu\nu} = g_{\mu\nu} + h_{\mu\nu} \ , \tag{2.19}$$

and look at the different modes separately.
We know that by a spatial coordinate transformation, the components g_{00}, g_{0j} and g_{ij} of the metric tensor transform as scalar, vector and tensor quantities respectively. then in all generality we may write:

$$\begin{aligned}
\tilde{g}_{00} &= -\, a^2 \left(1 + 2\, A\, Q^{(0)} \right) \ , \\
\tilde{g}_{0j} &= -\, a^2 \left(B\, Q_j^{(0)} + B^{(1)}\, Q_j^{(1)} \right) \ , \\
\tilde{g}_{ij} &= -\, a^2 \left(\gamma_{ij} + 2\, H_L\, Q^{(0)}\, \gamma_{ij} + 2\, H_T\, Q_{ij}^{(0)} + 2\, H_T^{(1)}\, Q_{ij}^{(1)} + 2\, H_T^{(2)}\, Q_{ij}^{(2)} \right) \ .
\end{aligned} \tag{2.20}$$

We may interpret the functions of time A, B, $B^{(1)}$, H_L, H_T, $H_T^{(1)}$, $H_T^{(2)}$ as amplitudes of the perturbation. Specifically, A is the amplitude of perturbation in the ratio of proper- and coordinate- time distance between two neighbouring constant time hypersurfaces. B, $B^{(1)}$ may be seen as amplitudes associated with a perturbation in the rate of deviation of

a constant space-coordinate line from a line normal to a constant time hypersurface. H_L is the amplitude of perturbation of a unit spatial volume; and finally H_T, $H_T^{(1)}$ and $H_T^{(2)}$ are amplitudes related to the distortion of each constant time hypersurface.

A clever gauge choice will considerably simplify 2.20 and make matters easier to handle. As mentioned in the Introduction to this chapter, perturbation theory on curved spaces suffers from gauge ambiguities - we won't concern ourselves with the details and will make a typical gauge choice: the Newtonian gauge, which leaves us with [17]:

$$\begin{aligned} A \equiv \Psi \ , \qquad B = 0 \ , \qquad B^{(1)} \equiv -V \ , \\ H_L \equiv \Phi \ , \quad H_T = 0 = H_T^{(1)} \ , \quad H_T^{(2)} \equiv H \ . \end{aligned} \tag{2.21}$$

Then, reconstructing $h_{\mu\nu}$, we see that in the Newtonian gauge we have

$$\begin{aligned} h_{\mu\nu} = -2\,a^2 \begin{pmatrix} \Psi & 0 & 0 & 0 \\ 0 & & & \\ 0 & & \Phi\,\boldsymbol{\gamma} & \\ 0 & & & \end{pmatrix} Q^{(0)} + a^2\,V \begin{pmatrix} 0 & & \boldsymbol{Q}^{(1)} & \\ & & & \\ {}^T\boldsymbol{Q}^{(1)} & & 0 & \\ & & & \end{pmatrix} + \\ -2\,a^2\,H_T^{(0)} \begin{pmatrix} 0 & 0 & 0 & 0 \\ 0 & & & \\ 0 & & Q^{(2)} & \\ 0 & & & \end{pmatrix} \ , \end{aligned} \tag{2.22}$$

where we've decomposed the perturbation into its three different modes, scalar, vector and tensor. When the metric on the 3-dimensional subspace is simply $\boldsymbol{\gamma} \equiv \mathbb{1}$, we see that the scalar contribution is purely diagonal, the vector contribution only disturbs the $\tilde{g}_{0i}$, $\tilde{g}_{i0}$ terms, and the tensor mode the spatial $\tilde{g}_{ij}$ part.

Perturbing the energy-momentum tensor. Let us see, for the sake of completeness, what happens to the right hand side of Einstein's equations, and then relate this to what we've seen above. Using the same framework as before, we may decompose a general energy-momentum tensor $T_{\mu\nu}$ into scalar, vector and tensor eigenmodes:

$$\begin{aligned} T_{00} =& \rho \ , \\ T_{0i} =& \hat{\mathsf{k}}_i\,v + \omega_i \ , \\ T_{ij} =& p\,\delta_{ij} + \left(\hat{\mathsf{k}}_i\,\hat{\mathsf{k}}_j + \frac{1}{3}\,\delta_{ij}\right)\,\Pi^{(0)} + \left(\hat{\mathsf{k}}_i\,\Pi_j^{(1)} + \hat{\mathsf{k}}_j\,\Pi_i^{(1)}\right) + \Pi_{ij}^{(2)} \ , \end{aligned} \tag{2.23}$$

with

$$\hat{\mathsf{k}} \cdot \boldsymbol{\omega} = 0 \ , \qquad \hat{\mathsf{k}} \cdot \boldsymbol{\Pi}^{(1)} = 0 \ , \qquad \hat{\mathsf{k}}^i\,\Pi_{ij}^{(2)} = 0 \ , \qquad \mathrm{Tr}(\boldsymbol{\Pi}^{(2)}) = 0 \ . \tag{2.24}$$

There are four scalar quantities: the energy density ρ, the scalar velocity v, the isotropic pressure p and the scalar anisotropic stress $\Pi^{(0)}$. Two vectors: the vorticity $\boldsymbol{\omega}$ and the vector anisotropic stress $\boldsymbol{\Pi}^{(1)}$. Lastly, there is one tensor quantity $\boldsymbol{\Pi}^{(2)}$ which is the tensor (traceless) contribution to the anisotropic stress.
We refer the reader to the Kodama-Sasaki review [14], and report only the final result

for a perturbed energy-momentum tensor $T_{\mu\nu}$, in the Newtonian gauge. For the scalar perturbations we have:

$$\begin{aligned}
\tilde{T}^0{}_0 =& -\rho\,(1+\delta\rho^{(0)}\,Q^{(0)})\ ,\\
\tilde{T}^0{}_j =& (\rho+p)\,\delta v^{(0)}\,Q^{(0)}{}_j\ ,\\
\tilde{T}^i{}_j =& p\,(\delta^i{}_j+\delta p^{(0)}\,\delta^i{}_j+\delta\Pi^{(0)}\,Q^{(0)\,i}{}_j)\ ,
\end{aligned} \tag{2.25}$$

where the δ quantities are perturbations of the defining variables of the unperturbed $T_{\mu\nu}$, and are related to the scalar mode simply by some coefficients,

$$\delta\rho^{(0)}=a^{(0)}\,Q^{(0)}\ ,\quad \delta v^{(0)}=b^{(0)}\,Q^{(0)}\ ,\quad \delta p^{(0)}=c^{(0)}\,Q^{(0)}\ ,\quad \delta\Pi^{(0)}=d^{(0)}\,Q^{(0)}\ . \tag{2.26}$$

The same may be obtained for the vector perturbations:

$$\begin{aligned}
\tilde{T}^0{}_0 =& -\rho\ ,\\
\tilde{T}^0{}_j =& (\rho+p)\,(\delta v^{(1)}+V)\,Q^{(1)}{}_j\ ,\\
\tilde{T}^j{}_0 =& -(\rho+p)\,\delta v^{(1)}\,Q^{(1)\,j}\ ,\\
\tilde{T}^i{}_j =& p\,(\delta^i_j+\delta\Pi^{(1)}\,Q^{(1)\,i}{}_j)\ ;
\end{aligned} \tag{2.27}$$

and tensor:

$$\begin{aligned}
\tilde{T}^0{}_0 =& -\rho\ ,\\
\tilde{T}^0{}_j =& 0=\tilde{T}^j{}_0\\
\tilde{T}^i{}_j =& p\,(\delta^i_j+\delta\Pi^{(2)}\,Q^{(2)\,i}{}_j)\ .
\end{aligned} \tag{2.28}$$

2.3 Possible Sources of Vector Perturbations in the Universe

In general, to source a vector type perturbation in the metric describing our Universe we need to perturb matter (i.e. energy) in such a way that the vector modes $Q^{(1)}$ are excited. At second order, scalar density perturbations will do the trick; also bulk flows of energy will produce vector perturbations in spacetime, while gravity waves only generate tensor perturbations. These are of course interesting to study, as they give us insight on early structure formation, but we have precious little data which may be retraced to such sources.
Bulk flows will be the result of significant peculiar velocities associated to energy overdensities. These flows will be characterised principally by the preferential direction of motion, which we may imagine would produce a dipole-like disturbance in spacetime. To be at all physically relevant, these velocities would have to be close to relativistic, otherwise the scalar contribution given by the mass distribution would largely overshadow the vector part; a possible example of bulk flow could be free-streaming relativistic neutrinos.

At first order, topological defects such as cosmic strings may excite vector modes in the metric [11]; they arise when a complex field exits a false vacuum and rolls down to a global one after a symmetry breaking phase transition. These macroscopic strings carry

energy and momentum, and thus necessarily perturb spacetime. These perturbations may be traced back to line-like discontinuities in the Cosmic Microwave Background temperature, via the Kaiser-Stebbins effect [19]: the rapidly changing gravitational field of a string lenses photon trajectories in its vicinity, leaving a particular print in the CMB. The vector-induced signal is theorised to be an order of magnitude greater than the tensor-induced one, so they are a prime source of vector perturbations.
For now, cosmic strings are purely theoretical objects and haven't been observed - rotations in CMB anisotropies would provide a candidate detection for these.

Let us look back at the decomposition 2.22, where, as a result of a careful gauge choice, we had a very simple picture of what the different types of perturbations would do to a spacetime metric. Notice how a vector type perturbation would give rise to off-diagonal, mixed terms of the type $\tilde{g}_{0i}$ essentially generated by a vector $\boldsymbol{Q}^{(1)}$. So, it seems reasonable to assume that if we had a solution $g^{\star}_{\mu\nu}$ to Einstein's equations, asymptotically flat and describing a physical system, which may be written as a background metric $g_{\mu\nu}$ plus a matrix like

$$\boldsymbol{h} = \begin{pmatrix} 0 & \boldsymbol{v} \\ {}^{T}\boldsymbol{v} & 0 \end{pmatrix} \ , \tag{2.29}$$

this could be considered to be a spacetime perturbed by a vector perturbation.
Reviewing the (few) known exact solutions to Einstein's equations in vacuum, we realise that there is a very simple metric which presents off-diagonal terms and which may be interpreted as a vector perturbation of flat space: the Kerr-Neuman metric, which describes a spacetime with a rotating, spherically symmetric charge at the origin. Setting the electromagnetic charge to 0, let us take a look at the structure of the Kerr metric to convince ourselves that indeed it may be the result of a vector perturbation, and leave the full review of the properties of the metric to Chapter 3.

The Kerr Metric as a Vector Perturbation. In order to investigate lensing effects brought about by vector perturbations of spacetime, we take a closer look at one of the simplest metrics which presents a vector-like component, namely the Kerr metric.
The Kerr metric in Boyer-Lindquist coordinates [20] (t, r, θ, ϕ) is of the form,

$$g_{\mu\nu\,Kerr} = \begin{pmatrix} g_{tt} & 0 & 0 & g_{t\phi} \\ 0 & \frac{\Sigma(r,\theta)}{\Delta(r,\theta)} & 0 & 0 \\ 0 & 0 & \Sigma(r,\theta) & 0 \\ g_{t\phi} & 0 & 0 & g_{\phi\phi} \end{pmatrix} \ , \tag{2.30}$$

where

$$\Delta(r) \equiv r^2 - 2\,m\,r + a^2 \ , \quad \Sigma(r,\theta) \equiv r^2 + a^2\,\cos^2\theta \ ,$$

m is a parameter associated to the mass (energy) concentrated at the coordinate origin and a is the mass-scaled angular momentum. Its inverse is also fairly simple to obtain,

$$g^{\mu\nu}_{Kerr} = \begin{pmatrix} g^{tt} & 0 & 0 & g^{t\phi} \\ 0 & \frac{\Delta(r,\theta)}{\Sigma(r,\theta)} & 0 & 0 \\ 0 & 0 & \frac{1}{\Sigma(r,\theta)} & 0 \\ g^{t\phi} & 0 & 0 & g^{\phi\phi} \end{pmatrix} , \tag{2.31}$$

and presents a similar structure. The explicit expressions for all the matrix entries are reported in Appendix B, and they are all functions of (r, θ) only. At a glance, one may be led to believe that as the metric presents a non-zero diagonal + a vector term ${}^T\boldsymbol{v} = (0,\, 0,\, g_{t\phi})$ off the diagonal, it is the result of a scalar + a vector perturbation. Let us see in what sense this is the case.

First of all, supposing the system carries a small angular momentum compared to the total mass, we may expand the metric to first order in a obtaining

$$g_{\mu\nu\, Kerr} = \begin{pmatrix} 1 - \frac{2\,m}{r} & 0 & 0 & -\frac{m\,\sin^2\theta}{r}\,a \\ 0 & \left(1 - \frac{2\,m}{r}\right)^{-1} & 0 & 0 \\ 0 & 0 & r^2 & 0 \\ -\frac{m\,\sin^2\theta}{r}\,a & 0 & 0 & r^2\,\sin^2\theta \end{pmatrix} + \mathcal{O}(a^2) \ . \tag{2.32}$$

On the diagonal, we find the Schwarzschild metric in polar coordinates,

$$g_{\mu\nu\, Schw} = \mathrm{diag}(\left(1 - \frac{2\,m}{r}\right),\, \left(1 - \frac{2\,m}{r}\right)^{-1},\, r^2,\, r^2\,\sin^2\theta) \ ;$$

the off diagonal terms are of the type shown in 2.29, if we identify

$$\boldsymbol{v} = -\begin{pmatrix} 0 \\ 0 \\ \frac{m\,\sin^2\theta}{r} \end{pmatrix} a \ .$$

Both Schwarzschild and Kerr metrics are asymptotically flat, and may be viewed as perturbations of flat Minkowski space, if the defining parameters are small. We see how we may interpret the Schwarzschild spacetime as a scalar perturbation to Minkowski, when m is small, and the Kerr spacetime as a purely vector perturbation of Schwarzschild, at first order in a.
Expanding at higher orders in a we get second order terms in the diagonal of $g_{\mu\nu\, Kerr}$; these may be seen as a further scalar contribution to the perturbed spacetime.
Of course, neither the Schwarzschild nor the Kerr spacetime may model the Universe, so comparing these to cosmological perturbations is slightly unorthodox. However, if we fix a time t and consider small patches of sky, the same basic principles should hold.

Certainly, vector perturbations which may be described by the Kerr metric are only a small part of all possible vector perturbations of spacetime. They are however an interesting test case, and may be used to gauge the B-mode generated by a rotating compact object - this is our ultimate objective.

Chapter 3

Lensing in the Kerr Spacetime

3.1 Introduction and Formalism of the Kerr Metric

The Kerr solution of Einstein's equations 1.2 in vacuum ($T^{\mu\nu} = 0$) was found by Roy Kerr in 1963. It belongs to a 2−parameter family of solutions, (M, J) and thus describes a rotating black hole with mass M and angular momentum J, and is both stationary and axisymmetric [21]. Due to the uniqueness theorems, it is also the only solution to Einstein's equations which describes such a spacetime.
In Chapter 2, we've seen why we're interested in this particular metric: it may be seen as giving rise to a vector type perturbation of flat space, and as it is an exact solution to 1.2, we find it may contain precious insight to the general topic of vector perturbations.

We shall first review the formalism of the Kerr spacetime we'll be using throughout the chapter, then carry out detailed calculations to derive an analytic lensing map around the origin. Then, we'll show what rotation generates in the distortion of the background, and underline all interesting effects.

The explicit form of the Kerr metric is usually expressed in the *Boyer-Lindquist Coordinates* (t, r, θ, ϕ) [22], which are related to Cartesian coordinates (x, y, z) as follows:

$$\begin{aligned} x =& \sqrt{r^2 + a^2}\, \sin\theta\, \cos\phi \ , \\ y =& \sqrt{r^2 + a^2}\, \sin\theta\, \sin\phi \ , \\ z =& r\, \cos\theta \ ; \end{aligned} \tag{3.1}$$

the metric is

$$\begin{aligned} ds^2 =& -\frac{\Delta - a^2 \sin^2\theta}{\Sigma}\, dt^2 + \frac{\Sigma}{\Delta}\, dr^2 + \Sigma\, d\theta^2 + \frac{(r^2 + a^2)^2 - \Delta\, a^2 \sin^2\theta)}{\Sigma}\, \sin^2\theta\, d\phi^2 \\ &+ \frac{4m\, a\, r\, \sin^2\theta}{\Sigma}\, dt\, d\phi \ , \end{aligned} \tag{3.2}$$

$$\Delta(r) \equiv r^2 - 2\, m\, r + a^2 \ , \quad \Sigma(r, \theta) \equiv r^2 + a^2\, \cos^2\theta \ . \tag{3.3}$$

The Kerr metric depends on two parameters, the mass parameter of the black hole m and the mass-scaled angular momentum $a = \frac{J}{m}$, as measured from infinity. Note that

$m = \frac{GM}{c^2}$, but as we equate all constants to 1 throughout the chapter, $c = 1 = G$, we will from now on simply refer to m as the mass; remember however that it has spatial dimension.
At a glance, one can see that the Kerr spacetime is t-independent and thus is stationary, and also ϕ-independent thus axisymmetric. It is not static, as it breaks the time-reversal symmetry, but it is invariant under the simultaneous transformation of $t \to -t$, $\phi \to -\phi$; this is not surprising, as time-reversing a rotating object produces an object rotating in the opposite direction. It further depends on the two coordinates r and θ.

Let's look at the interesting limits of the case:

- $r \to \infty$: 3.2 is reduced to the Minkowski metric (in polar coordinates), hence the Kerr spacetime is asymptotically flat.
- $a \to 0$, $m \neq 0$: 3.2 is reduced to the Schwarzschild metric 1.1; this is consistent with the idea that as a rotating black hole slows down, it transitions continuously to a static black hole.
- $m \to 0$, $a \neq 0$: 3.2 is reduced to the Minkowski metric in spheroidal coordinates, with radius $\rho = \sqrt{r^2 + a^2}$.

The Kerr metric also has interesting singularities: it diverges for $\Delta = 0$ and $\Sigma = 0$. A computation of the Kretschmann scalar $K = R_{\alpha\beta\gamma\delta}R^{\alpha\beta\gamma\delta}$, explicitly [23]

$$K = \frac{48\,m^2}{(r^2 + a^2\,\cos^2\theta)^6}\left(r^6 - 15a^2r^4\cos^2\theta + 15a^4r^2\cos^4\theta - a^6\cos^6\theta\right) \quad , \tag{3.4}$$

shows that $\Sigma = 0$ is a true spacetime singularity, as it is satisfied by the conditions $r = 0$, $\theta = \frac{\pi}{2}$ which cause K to diverge; $\Delta = 0$ on the other hand is a coordinate singularity, and its roots $r_\pm = m \pm \sqrt{m^2 - a^2}$ identify two distinct horizons of the black hole: the inner horizon r_- and the event horizon r_+.

Equations of Motion. We derive the equations of motion for a Kerr null geodesic $x^\mu(\lambda) = (t(\lambda),\, r(\lambda),\, \theta(\lambda),\, \phi(\tau))$ just as we did for the Schwarzschild case, using the Lagrangian 1.3, the normalisation condition 1.8 and the conserved quantities of the spacetime. To find these, we write down the killing vectors for Kerr,

$$k_t^\mu = \begin{pmatrix}1\\0\\0\\0\end{pmatrix} \quad , \qquad m^\mu = \begin{pmatrix}0\\0\\0\\1\end{pmatrix} \quad , \tag{3.5}$$

and recognise that as in the Schwarzschild case the energy E 1.5 and the angular momentum around the z axis $L = m_\mu \dot{x}^\mu$ are conserved. There is a third conserved quantity, the Carter constant Q, which is not related to any isometry of the metric [21]. It is recovered via the *Hamilton-Jacobi* approach; we won't go through it explicitly - for details on the derivation see Roy Carter's argument in [24]. It may be written as [25]

$$Q = \dot{\theta}^2 + \cos^2\theta\left(-a^2E^2 + \frac{L^2}{\sin^2\theta}\right) \quad . \tag{3.6}$$

Given the definitions of E and L, we immediately find that

$$E = -\left(g_{tt}\,\dot{t} + g_{t\phi}\,\dot{\phi}\right) \ , \quad L = g_{\phi\phi}\,\dot{\phi} + g_{t\phi}\,\dot{t} \ , \tag{3.7}$$

which reversed return

$$\dot{t} = \frac{g_{\phi\phi}E + g_{t\phi}L}{g_{t\phi}^2 - g_{tt}g_{\phi\phi}} \ , \quad \dot{\phi} = -\frac{g_{t\phi}E + g_{tt}L}{g_{t\phi}^2 - g_{tt}g_{\phi\phi}} \ ; \tag{3.8}$$

we can do the same with 3.6 to obtain

$$\dot{\theta} = \pm\frac{\sqrt{Q + E^2a^2\cos^2\theta - L^2\mathrm{ctan}^2\theta}}{\Sigma(r,\theta)} \ . \tag{3.9}$$

The equation for $r(\lambda)$ is simply obtained from the normalisation condition on the 4-velocity:

$$\dot{r} = \pm\sqrt{-\frac{g_{tt}\dot{t}^2 + g_{\theta\theta}\dot{\theta}^2 + g_{\phi\phi}\dot{\phi}^2 + 2g_{t\phi}\dot{t}\dot{\phi}}{g_{rr}}} \ . \tag{3.10}$$

These equations show how the geodesic motion depends on two coordinates, r and θ, plus the three constants of motion E, L and Q which remain fixed throughout. We can immediately make matters more simple by dividing these by a chosen constant, in our case E, and reparametrising the affine parameter $\hat{\lambda} \equiv E\lambda$ to get (now writing out the terms explicitly)

$$\begin{aligned}
\dot{\hat{t}} =& 1 + \frac{4m\,r\,(a^2 - \hat{L} + r^2)}{\Delta(r)\Sigma(r,\theta)} \ , \\
\dot{\hat{r}} =& \pm\frac{\sqrt{r^4 - (\hat{Q} - \hat{L}^2 - a^2)r^2 + 2m\,((\hat{L} - a)^2 + \hat{Q})r - a^2\,\hat{Q}}}{\Sigma(r,\theta)} \ , \\
\dot{\hat{\theta}} =& \pm\frac{\sqrt{\hat{Q} + a^2\cos^2\theta - \hat{L}^2\,\mathrm{ctan}^2\theta}}{\Sigma(r,\theta)} \ , \\
\dot{\hat{\phi}} =& \frac{2\,a\,m\,r + \hat{L}(r^2 - 2m\,r)\,\mathrm{csec}^2\theta + a^2\hat{L}\mathrm{ctan}^2\theta}{\Delta(r)\Sigma(r,\theta)} \ ;
\end{aligned} \tag{3.11}$$

so now we only have two independent constants, namely $\hat{L} = \frac{L}{E}$ and $\hat{Q} = \frac{Q}{E}$. Note that the hat-dot notation implies $\frac{d}{d\hat{\lambda}}$, such that $\dot{\hat{t}} = \frac{dt}{d\hat{\lambda}}$. These are the equations of motion for the null geodesic x^μ which we will be using to work out the observable bend angle of a light ray lensed by a rotating object.

It is hard to integrate analytically these equations directly and work out the trajectory of a bent light ray. We will work in a particular regime to make matters a little simpler, the *quasi-equatorial regime*: we constrain the motion to evolve close to the equatorial plane, which is a uniquely defined plane due to the axisymmetric symmetry of the spacetime and corresponds to the coordinate angle $\theta = \frac{\pi}{2}$. It will appear useful to change coordinates, so that effectively the equatorial plane lies at a coordinate angle $\zeta = 0$ and motion occurs at perturbed values of the latter. In this new coordinate, the Kerr equations of motion become

$$
\begin{aligned}
\hat{\dot{t}} =& 1 + \frac{4m\,r\,(a^2 - \hat{L} + r^2)}{\Delta(r)\Sigma(r,\zeta)} \ , \\
\hat{\dot{r}} =& \pm \frac{\sqrt{r^4 - (\hat{Q} - \hat{L}^2 - a^2)r^2 + 2m\,((\hat{L} - a)^2 + \hat{Q})r - a^2\,\hat{Q}}}{\Sigma(r,\zeta)} \ , \\
\hat{\dot{\zeta}} =& \pm \frac{\sqrt{\hat{Q} + a^2 \sin^2\zeta - \hat{L}^2\,\tan^2\zeta}}{\Sigma(r,\zeta)} \ , \\
\hat{\dot{\phi}} =& \frac{2\,a\,m\,r + \hat{L}(r^2 - 2m\,r)\,\sec^2\zeta + a^2\hat{L}\tan^2\zeta}{\Delta(r)\Sigma(r,\zeta)} \ ,
\end{aligned}
\tag{3.12}
$$

with $\Sigma(r,\zeta) = r^2 + a^2\,\sin^2\zeta$.

Note that this is a sensible constraint to impose, which doesn't undermine the value of this map. In fact, the equatorial plane is the plane on which the total bend angle $\boldsymbol{\alpha}$ is most appreciable, and as we are limiting ourselves to the case where the observer lies on the equatorial plane, and the mass is rotating at sub-critical speed, the effects due to rotation will be very small, so it makes sense to assess them where they are most visible.

3.2 Light Bending in the Kerr Metric

Before we dive into the chapter, let us offer the reader an intuitive picture of what one may expect to see when observing lensing around a compact object which is rotating, and in what this case differs from lensing around an object which is not rotating and may be described by the Schwarzschild metric. In Figure 3.1 we represent the same scenario in both cases: light rays are emitted from a source at the same angle, but on opposite sides of the optical axis; in Schwarzschild space (a) lensing is symmetric around the mass m, whereas in Kerr (b) we have asymmetric lensing. This is due to the angular momentum J of the mass, which breaks the symmetry of the spacetime and 'pulls' *prograde* rays towards m, and 'pushes' *retrograde* rays away so that rays emitted at the same angle passing the mass from different sides will have different paths and will cross the optical axis in different points.

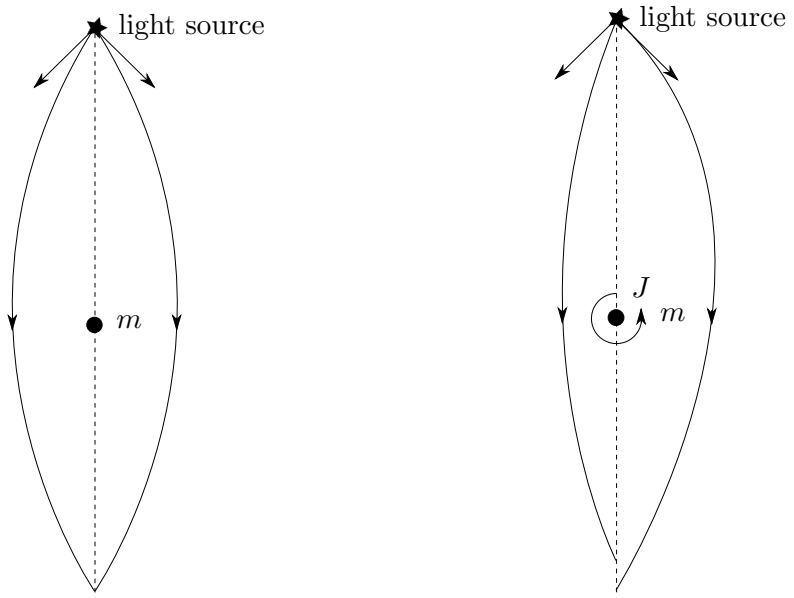

(a) Schwarzschild (b) Kerr

Figure 3.1: A simple illustration of lensing in the two metrics mentioned above. Note how rays which leave the light source at the same angle with the optical axis are bent differently in the Kerr case, depending on what side of the axis they approach the lens.

We will obtain the bend angle and lens equation for a light ray gravitationally lensed by a spherically symmetric, rotating compact object, in the the quasi-equatorial regime. The recipe is the same as in Section 1.3, and follows the guidelines of [6] and [26]; as in the Schwarzschild case, we are assuming that observer and light source lie in the asymptotically flat region, and don't disturb the metric. Furthermore, we assume that the light source doesn't lie far off the equatorial plane, which is the plane horizontal to the angular momentum, $\vec{L}$.
The geometry is quite tricky, as a lensed photon's trajectory doesn't lie on a plane ($\dot{\theta} \neq 0$). Effectively, this means that the two tangents to the motion, at the observer and at the light source, lie on separate planes in space and never meet. We will refer to the line tangent to the motion at the observer as the *outgoing line*, and to the tangent at the source as the *ingoing line*. The outgoing line intersects the lens plane in A, the ingoing

line intersects the lens in B.

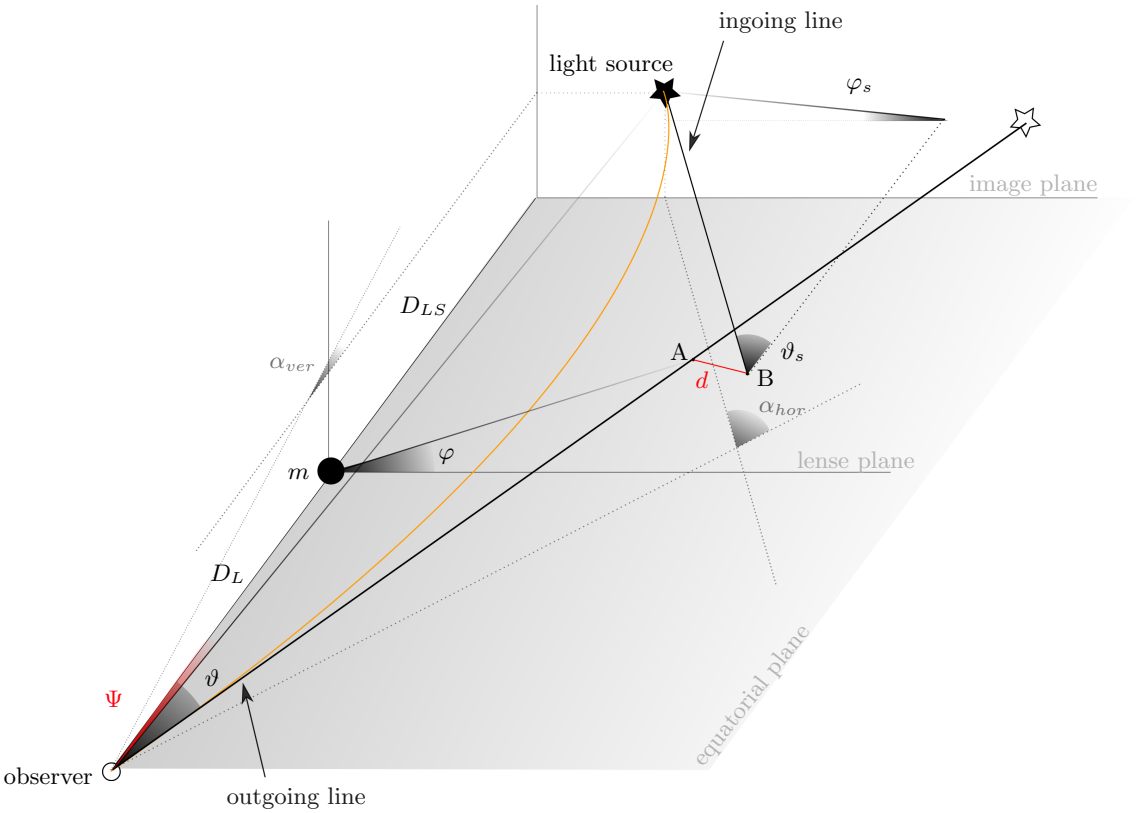

Figure 3.2: $3D$ view of lensing in the Kerr metric. To draw this diagram, it is essential for the geometry to be asymptotically flat, and we may assume $b \gg m$ such that we are measuring angles in the flat region.

Looking at Figure 3.2, we list the angles of interest as follows:

- **Image position:** The position of the image is fixed by the two angles (ϑ, φ). $\boldsymbol{\vartheta}$ is the 2-dimensional angle subtended by the outgoing line and the optical axis x and ϑ is its amplitude, φ is the angular position of A on the lens plane. We choose their domains carefully: we set $0 < \vartheta < \frac{\pi}{2}$, which spans only half of the image plane, but we can easily recover the other half by flipping the sign of the angular momentum J. The same goes for $0 < \varphi < \frac{\pi}{2}$
- **Source position:** The position of the source is pinpointed by (ϑ_s, φ_s), which have the domains: $-\frac{\pi}{2} < \vartheta_s < \frac{\pi}{2}$; $0 < \varphi_s < 2\pi$. ϑ_s quantifies the deviation of the incoming line with respect to the optical axis direction and is the amplitude of $\boldsymbol{\vartheta}_s$, φ_s quantifies the deviation of the incoming line with respect to the equatorial plane. Effectively, the quasi-equatorial regime implies that φ_s is small.
- **Bend angle:** Since the motion does not occur on a plane, there is no physical angle α as in the Schwarzschild case. Thus, we must project the incoming and outgoing lines on the equatorial plane (xy) and vertical plane (xz), where they form the angles α_{hor} and α_{ver} respectively.

To calculate the bend angles α_{hor} and α_{ver} as functions of the observable angles (ϑ, φ), we need to integrate the equations of motion 3.12 setting the appropriate boundary conditions. Also, we rewrite $\hat{L}$ and $\hat{Q}$ as functions of (ϑ, φ) - much as we did for $\frac{L}{E}$ in the Schwarzschild case - by considering their values at infinity. We do this in full in Appendix B, obtaining

$$\hat{L} = -D_L \sin\vartheta \cos\varphi \ , \qquad \hat{Q} = D_L^2 \sin^2\vartheta \sin^2\varphi \ . \tag{3.13}$$

In the quasi-equatorial regime, these reduce to

$$\hat{L} = \mathsf{s}\, b \cos\varphi \ , \qquad \hat{Q} = b^2 \sin^2\varphi \ , \tag{3.14}$$

where $b \equiv D_L \sin\vartheta$ is the impact parameter just as in the Schwarzschild case; s is the sign of the angular momentum, and is either $+1$ for prograde motion, or -1 for retrograde motion. These will be immediately substituted in 3.12.

We proceed to work out the two components of the bend angle starting from the equations of motion, in the quasi-equatorial regime.

3.2.1 Horizontal Bend Angle α_{hor}

The horizontal component of the bend angle is obtained exactly as α in the Schwarzschild case; in fact, the geometry in Figure 3.3 is the same as the one in Figure 1.5. The equation for α_{hor} is again

$$\alpha_{hor} = 2\int_{\infty}^{r_0} \left|\frac{\dot{\phi}}{\dot{r}}\right| dr - \pi \equiv \vartheta_1 + \vartheta_{s,1} \ ,^{1} \tag{3.15}$$

where we need to substitute in 3.12 with the explicit terms 3.14. We have

$$\frac{\dot{\phi}}{\dot{r}} = \pm \frac{2amr + br\,(-2m+r)\,\mathsf{s}\cos\varphi\sec^2\zeta + a^2 b\mathsf{s}\cos\varphi\,\tan^2\theta}{\Delta(r)\sqrt{r\,(b^2(2m-r) + r^3 + a^2(2m+r)) - ab\,(4mr\mathsf{s}\cos\varphi + ab\sin\varphi^2)}} \ .$$

To integrate this, we must resort to careful simplifications, which must maintain the correct dependencies of the various quantities from the observable angles - this will become of importance later, when we work out the distortion matrix $\mathcal{D}$. As we are in the quasi-equatorial regime, we may

- Expand around 0 to first order in the coordinate ζ, as we expect it to remain around the equatorial value throughout the whole trajectory;
- Consider φ to be small, as we are only slightly off the equatorial plane;
- Consider a to be small, so we keep second order terms φ^2, ζ^2 and mixed terms $\varphi\zeta$ only if they aren't multiplied by a.

Thus, we're left with

[1] Note: $\vartheta_{s,1}$ may be negative, in which case $\vartheta_1 > \alpha_{hor}$.

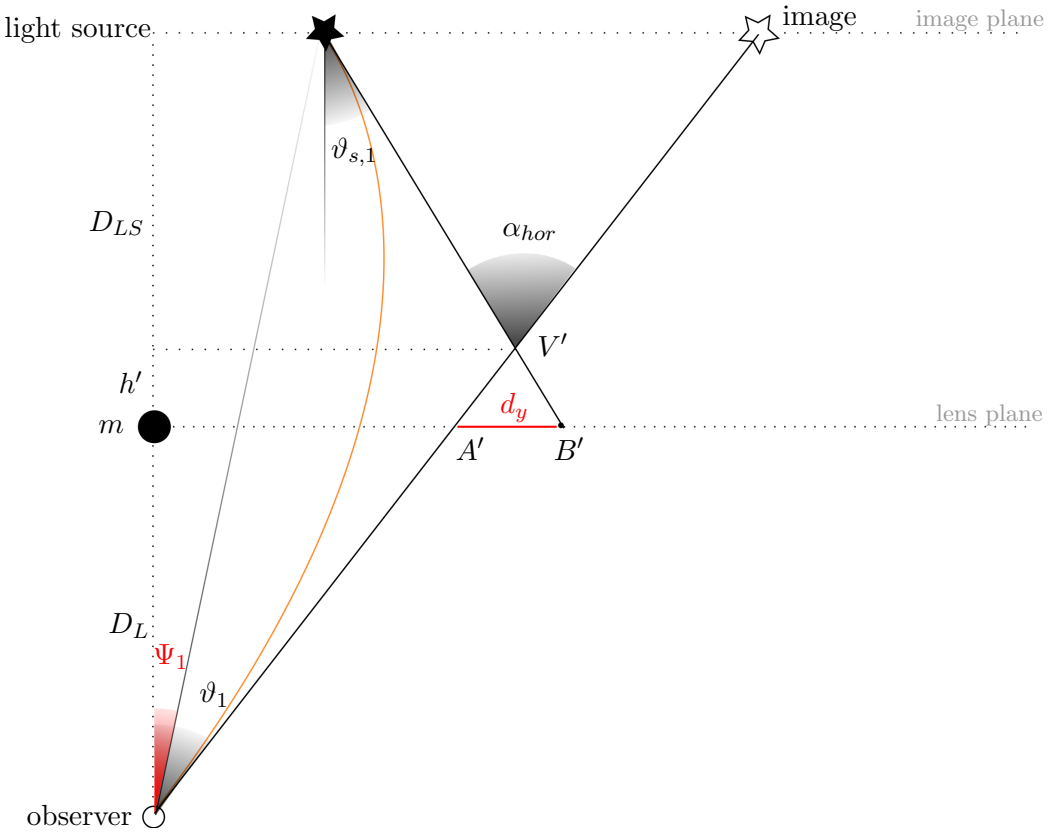

Figure 3.3: View of the equatorial plane (i.e. the (xy) plane) of our set up. Note the *displacement triangle* (d_y, V') of base d_y and vertex V'. ϑ_1 and $\vartheta_{s,1}$ are the components on this plane of the angles $\boldsymbol{\vartheta}$, $\boldsymbol{\vartheta}_s$ respectively. These are in general 2-dimensional angles in space, and their amplitudes are related to those of their projections as

$$\tan\vartheta = \frac{\tan\vartheta_1}{\cos\varphi} \ , \qquad \tan\vartheta_s = \frac{\tan\vartheta_{s,1}}{\cos\varphi_s} \ . \tag{3.16}$$

$$\frac{\dot\phi}{\dot r} = \frac{r^{1/2}\,(2\,a\,\mathsf{s}\,m - 2\,b\,m\,\cos\varphi + b\,r\,\cos\varphi)}{\Delta\,\sqrt{r^3 + b^2\,(2\,m\,\mathsf{F}^2 - \mathsf{G}\,r)}} \ , \tag{3.17}$$

where we've called

$$\mathsf{F} \equiv 1 - \mathsf{s}\frac{a}{b} \ , \qquad \mathsf{G} \equiv 1 - \frac{a^2}{b^2} \ , \tag{3.18}$$

to shorten the expression. Note how the terms involving $\cos\theta$ and $\tan\theta$ don't contribute at first order, so the deflection on the equatorial plane only depends on the position r, with a correction $\cos\varphi$ given by the rise off the plane. This expression is effectively second order in φ, as terms φ^3 have been suppressed.
To perform the integration of 3.17 we first need to relate b and r_0. We do this by solving the equation of motion for r from 3.12; it is a cubic equation in r_0 and has one real solution

$$r_0 = \frac{2\,b}{\sqrt{3}}\sqrt{\mathsf{G}}\,\cos\left[\frac{1}{3}\,\cos^{-1}\left(-3^{3/2}\,\frac{\mathsf{F}^2}{\mathsf{G}^{3/2}}\,\frac{m}{b}\right)\right]\ , \tag{3.19}$$

which Taylor expanded in $\frac{m}{b} \ll 1$ yields

$$r_0 = b\left(\sqrt{\mathsf{G}} - \frac{\mathsf{F}^2}{\mathsf{G}}\left(\frac{m}{b}\right) - \frac{3\,\mathsf{F}^4}{2\,\mathsf{G}^{5/2}}\left(\frac{m}{b}\right)^2 - \frac{4\,\mathsf{F}^6}{\mathsf{G}^4}\left(\frac{m}{b}\right)^3 - \frac{105\,\mathsf{F}^8}{8\,\mathsf{G}^{11/2}}\left(\frac{m}{b}\right)^4 + \mathcal{O}\left(\frac{m}{b}\right)^5\right)\ . \tag{3.20}$$

Next, we change the variable to $x = \frac{r_0}{r}$ and rewrite the expression as a function of x and $h = \frac{m}{r_0}$, so

$$\alpha_{hor} = 2\int_0^1 \frac{2\,a\,h\,x + 2\,b\,h\,x\cos\varphi - b\cos\varphi}{\left(1 - 2\,h\,x + \left(\frac{a}{m}\right)^2 h^2\,x^2\right)\sqrt{\mathsf{G}\,(1-x^2) - 2\,\mathsf{F}^2\,h\,(1-x^3)}}\,dx - \pi\ .$$

Let us keep F and G as implicit functions of b for the time being, expand the integrand in small h and integrate as we did in the Schwarzschild case with the help of ***Wolfram Mathematica***. Thus we obtain an expression for α_{hor} as an expansion in h:

$$\alpha_{hor} = \left[\mathsf{a}_0\,\pi + 4\,\mathsf{a}_1\,h - (4\mathsf{a}_{2,1} + \pi\,\mathsf{a}_{2,2})\,h^2 + \mathcal{O}(h^3)\right]\ , \tag{3.21}$$

where

$$\begin{aligned}
\mathsf{a}_0 &= \frac{\cos\varphi}{\sqrt{\mathsf{G}}} - 1\ , \\
\mathsf{a}_1 &= \frac{\mathsf{F}^2\cos\varphi + \mathsf{G} - \mathsf{F}\mathsf{G}}{\mathsf{G}^{3/2}}\ , \\
\mathsf{a}_{2,1} &= \frac{\mathsf{F}^2\,(\mathsf{F}^2\cos\varphi + \mathsf{G} - \mathsf{F}\mathsf{G})}{\mathsf{G}^{5/2}}\ , \\
\mathsf{a}_{2,2} &= \frac{\mathsf{G}\,(3\,\mathsf{F}^2 + 2\,\mathsf{G})(1-\mathsf{F}) + \cos\varphi\,\left(\frac{15}{4}\,\mathsf{F}^4 - \frac{1}{2}\left(\frac{a}{m}\right)^2\mathsf{G}^2\right)}{\mathsf{G}^{5/2}}\ .
\end{aligned} \tag{3.22}$$

We want to write the bend angle as a series expansion in $\frac{m}{b}$, so we substitute 3.20 and 3.18 into 3.21 and re-expand in $\frac{m}{b}$ to finally get

$$\begin{aligned}
\alpha_{hor} = {} & 4\,\cos\varphi\,\left(\frac{m}{b}\right) + \left(\cos\varphi\,\frac{15\pi}{4} + 4\,\mathsf{s}\,\frac{a}{m}\,(1 - 4\,\cos\varphi)\right)\left(\frac{m}{b}\right)^2 + \\
& + \left(\frac{128}{3} + 5\pi\,\mathsf{s}\,\frac{a}{m}\,(1 - 3\cos\varphi) + 4\cos\varphi\,\left(\frac{a}{m}\right)^2\right)\left(\frac{m}{b}\right)^3 + \mathcal{O}\left(\left(\frac{m}{b}\right)^4\right)\ .
\end{aligned} \tag{3.23}$$

This result agrees with with the Schwarzschild case 1.18, as the latter is recovered by simply setting $a = 0$ and choosing the plane $\varphi = 0$ as the equatorial plane (choice which one can and must make to recover the Schwarzschild series, as the angle α lies geometrically on such plane).

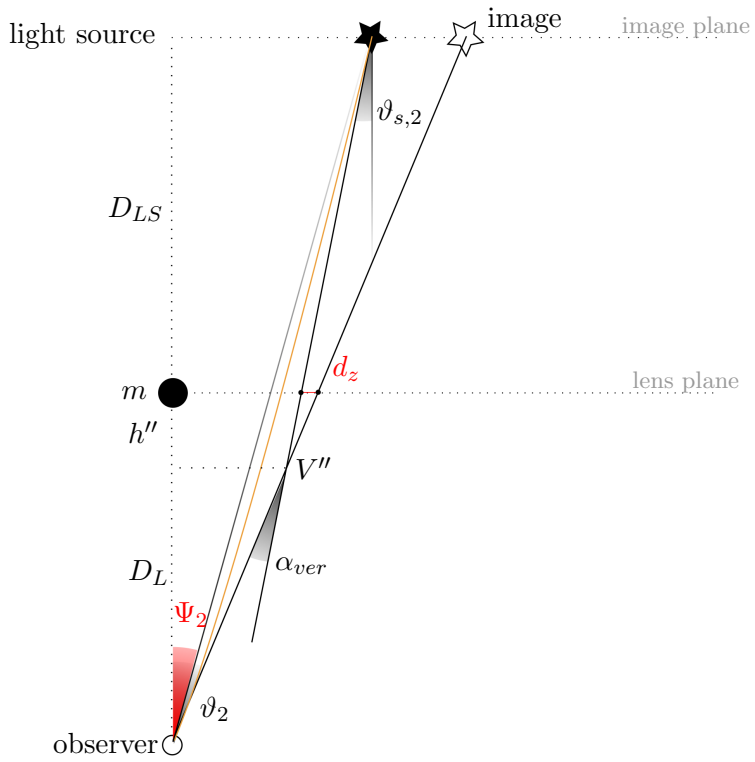

Figure 3.4: View of the vertical plane (i.e. the (xz) plane) of our set up. Note the *displacement triangle* (d_z, V'') of base d_z and vertex V''. ϑ_2 and $\vartheta_{s,2}$ are the components on this plane of the angles $\boldsymbol{\vartheta}$, $\boldsymbol{\vartheta}_s$ respectively. Their amplitudes are related to the other angles as

$$\tan\vartheta_2 = \tan\vartheta\,\sin\varphi \;\;, \qquad \tan\vartheta_{s,2} = \tan\vartheta_s\,\sin\varphi_s \;\;. \tag{3.24}$$

3.2.2 Vertical Bend Angle α_{ver}

Obtaining the vertical component of the bend angle as an expansion in $\frac{m}{b}$ is a little involved, as we need to integrate equations of motion with explicit ζ dependence which persists at first order. We follow the procedure in [26] and take the first order expansion of $\hat{\dot{\theta}}$ in both φ and ζ:

$$\hat{\dot{\zeta}} = \pm\frac{b}{r^2}\sqrt{\varphi^2 - \mathsf{G}\,\zeta^2} + \mathcal{O}(2) \;\;; \tag{3.25}$$

then we write

$$\frac{d\zeta}{dr} = \frac{\hat{\dot{\zeta}}}{\hat{\dot{r}}} = \pm\frac{b}{r^2}\frac{\sqrt{\varphi^2 - \mathsf{G}\,\zeta^2}}{\sqrt{1 - \frac{b^2}{r^2}\,\mathsf{G} + \frac{2\,m\,b^2}{r^3}\,\mathsf{F}^2}} = \pm\,i(r)\,\sqrt{\frac{\varphi^2}{\mathsf{G}} - \zeta^2} \;\;, \tag{3.26}$$

where the denominator is simply the first order of $\hat{r}$ in φ, ζ, so

$$i(r) = \frac{b\sqrt{\mathsf{G}}}{\sqrt{r^4 + b^2\, r\,(2\,m\,\mathsf{F}^2 - \mathsf{G}\,r)}} \ .$$

This leaves us with a differential equation for ζ which may be solved; specifically

$$\zeta(r) = \frac{\varphi}{\sqrt{\mathsf{G}}}\,\sin\left(\pm I(r) + p\right) \ , \qquad I(r) = \int_{r_0}^{r} i(r')\,dr' \ , \tag{3.27}$$

where p is a constant of integration. We're interested in the two asymptotic values of ζ (r $\to \infty$), as we're considering the source and the observer to be in the asymptotically flat region of space:

$$\zeta_{\pm} = \frac{\varphi}{\sqrt{\mathsf{G}}}\,\sin\left(\pm I(\infty) + p\right) \ ;$$

we can then eliminate p and relate the 2 asymptotic values to each other,

$$\zeta_{-} = \frac{\varphi}{\sqrt{\mathsf{G}}}\,\sin\left[-2\,I(\infty) + \sin^{-1}\left(\frac{\sqrt{\mathsf{G}}}{\varphi}\,\zeta_{+}\right)\right] \ . \tag{3.28}$$

It is well motivated in [26] that $\zeta_{-} \equiv \zeta_i$ and $\zeta_{+} \equiv \zeta_f$, where $\zeta_{i/f}$ are the initial and final values of the coordinate ζ respectively; furthermore, these are related to the observables ϑ, φ, ϑ_s, φ_s such that:

$$\sin\zeta_i = \sin\varphi_s\,\sin\vartheta_s \approx \varphi_s\,\sin\vartheta_s \ , \qquad \sin\zeta_f = \sin\varphi\,\sin\vartheta \approx= \varphi\,\sin\vartheta \tag{3.29}$$

at first order in φ and φ_s. Putting this together with 3.28 we get φ_s as a function of φ,

$$\varphi_s = \frac{\varphi}{\sqrt{\mathsf{G}}\,\sin\vartheta_s}\,\sin\left[-2\,I(\infty) + \sin^{-1}\left(\sqrt{\mathsf{G}}\,\sin\vartheta\right)\right] \ . \tag{3.30}$$

From Figure 3.4 it is further clear that

$$\alpha_{ver} = \vartheta_2 - \vartheta_{s,2} \ , \tag{3.31}$$

where $\alpha_{ver} > 0$ always, if we take $\vartheta_{s,2}$ as shown in Figure 3.4 to be positive. In fact, when $\vartheta_2 \equiv \vartheta_{s,2}$ we have no deflection on the (xz) plane, and the case where $\vartheta_{s,2} > \vartheta_2$ is nonphysical as it corresponds to the deflection of the light ray.
Then, we have all the ingredients necessary to derive α_{ver} as a result of the geometry and the Kerr equations of motion, as soon as we solve the integral $I(\infty)$. The latter may be written as an $\frac{m}{b}$ series just like the integral in α_{hor} - changing variable from r to $x = \frac{r_0}{r}$,

$$I(\infty) = \int_{r_0}^{\infty} \frac{b\sqrt{\mathsf{G}}}{\sqrt{r^4 - b^2\,\mathsf{G}\,r^2 + 2\,m\,b^2\mathsf{F}^2\,r}}\,dr = \int_0^1 \frac{\sqrt{\mathsf{G}}}{\sqrt{\mathsf{G}\,(1-x^2) - 2\,\mathsf{F}^2\,h\,(1-x^3)}}\,dx \ ,$$

where $h = \frac{m}{r_0}$ again. We expand in h, integrate in x and write h as an $\frac{m}{b}$ series, then we collect terms to get

$$I(\infty) = \frac{\pi}{2} + 2\,\left(\frac{m}{b}\right) + \left(\frac{15\pi}{8} - 4\,\mathsf{s}\,\frac{a}{m}\right)\,\left(\frac{m}{b}\right)^2 + \left(\frac{64}{3} - \frac{15\pi\,\mathsf{s}\,a}{2\,m} + 5\,\left(\frac{a}{m}\right)^2\right)\,\left(\frac{m}{b}\right)^3 + \mathcal{O}\left(\frac{m}{b}\right)^4 \ . \tag{3.32}$$

Putting together 3.16, 3.24, 3.30, we finally get

$$\begin{aligned}\alpha_{ver} &= \vartheta_2 - \text{atan}\left(\tan\varphi_s\ \tan(\alpha_{hor}-\theta_1)\right)\\ &\approx \vartheta_2 - \text{atan}\left(\frac{\varphi\ \sin\left[-2\,I(\infty)+\sin^{-1}\left(\sqrt{\mathsf{G}}\,\sin\vartheta\right)\right]}{\sqrt{\mathsf{G}}\,\cos\left(\alpha_{hor}-\theta_1\right)}\right)\ ,\end{aligned} \tag{3.33}$$

where we have taken the first order expansion in φ_s.
This expression is essentially first order in φ, whereas our expression for α_{hor} is second order. This doesn't worry us too much, as we're working in the quasi-equatorial regime, so invariably $\alpha_{ver} \ll \alpha_{hor}$ and its contribution will be less appreciable.

3.2.3 Image Position Ψ

As may be seen in Figure 3.2, the 2-dimensional angle $\boldsymbol{\Psi}$ pinpoints the position of the image on the image plane with respect to the observer. Ultimately, we want to write $\boldsymbol{\Psi}$ as a function of the observable angles, so as to work out both the true position of the source and the distortion matrix $\mathcal{D}$ as depicted in 1.40. A straightforward geometrical argument shows that the two components of $\boldsymbol{\Psi}$, Ψ_1 on the (xy) plane and Ψ_2 on the (xz) plane, depend on $\boldsymbol{\vartheta}$ as follows:

$$\begin{aligned}\tan\Psi_1 &= \tan\vartheta_1 - \left(\frac{D_{LS}}{h'}+\mathsf{q_y}\right)\frac{d_y}{D_S}\ ,\\ \tan\Psi_2 &= \tan\vartheta_2 - \left(\frac{D_{LS}}{h''}+\mathsf{q_z}\right)\frac{d_z}{D_S}\ ,\end{aligned} \tag{3.34}$$

where $\mathsf{q_y}$ and $\mathsf{q_z}$ are the signs associated to d_y, d_z respectively:

$$\mathsf{q_y} = \begin{cases}+1, & \vartheta_1 > \vartheta_{s,1}\\ -1, & \vartheta_1 < \vartheta_{s,1}\end{cases}\ , \qquad \mathsf{q_z} = \begin{cases}+1, & \vartheta_2 > \vartheta_{s,2}\\ -1, & \vartheta_2 < \vartheta_{s,2}\end{cases}\ . \tag{3.35}$$

The distances d_y, h', d_z, h'' are all positive definite; d_y, d_z are given through a lens equation specific for lensing in a Kerr spacetime where the observer lies on the equatorial plane, while h', h'' may be worked out through geometrical considerations. Let us address both of these.

Lensing displacement in the Kerr spacetime. From [6] we take the expressions for d_y and d_z, given as functions of the observable angles ϑ, φ and the angles associated to the position of the source ϑ_s, φ_s. They're obtained in detail within the Aazami paper considering constants of motion in the asymptotically flat region; they are[2]

$$d_y = D_L\ \sin\vartheta\ \cos\varphi\ \left|\frac{1}{\cos\vartheta_s}-\frac{1}{\cos\vartheta}\right|\ , \tag{3.36}$$

$$\begin{aligned}d_z = \Bigg|&-D_L\ \tan\vartheta\ \sin\varphi + \frac{D_L\ \sin\vartheta}{1-\sin^2\vartheta_s\ \sin^2\varphi_s}\times\\ &\left(\cos\varphi\ \sin\vartheta_s\ \tan\vartheta_s\ \sin\varphi_s\ \cos\varphi_s + \sqrt{\sin^2\varphi - \sin^2\vartheta_s\ \sin^2\varphi_s}\right)\Bigg|\end{aligned} \tag{3.37}$$

[2]Note: in paper [6] they allow d_y and d_z to have signs, and therefore omit the moduli.

By inserting the expressions for ϑ_s (3.16, 3.24) and φ_s (3.30) we obtain the total displacement as a function of observable angles (ϑ, φ).

It's quite easy to verify that, switching off rotation, the displacement 1.25 for the Schwarzschild case is recovered. In fact, the expression for d_y is the same; as for d_z, setting $a = 0$ implies $\varphi_s \equiv \varphi$, so the parenthesis in 3.37 becomes

$$\frac{\cos^2\varphi\,\sin^2\vartheta_s\,\sin\varphi - \sin\varphi\cos^2\vartheta_s}{\cos\vartheta_s} = \sin\vartheta\,\frac{1-\sin^2\vartheta_s\,\sin^2\varphi}{\cos\vartheta_s} \quad ,$$

so d_z reduces to

$$d_z|_{a=0} = D_L\,\sin\vartheta\,\sin\varphi\left(\frac{1}{\cos\vartheta_s} - \frac{1}{\cos\vartheta}\right) \quad ,$$

which agrees with 1.25.

h' and h''. The heights h' and h'' of the two displacement triangles, (d_y, V') and (d_z, V'') are key in the lens equations 3.34. We use the geometric rule for scalene triangles which states that: given the angle β and its opposite side L, the ratio $\frac{\sin\beta}{L}$ is constant throughout the triangle. We also use the notion that $\sin(\pi/2-\beta) = \cos\beta$. Then we easily obtain a formula for the heights, looking at the geometry in Figures 3.3 and 3.4:

$$h' = d_y\,\frac{\cos\vartheta_1\,\cos\vartheta_{s,1}}{\sin\alpha_{hor}} \quad , \tag{3.38}$$

$$h'' = d_z\,\frac{\cos\vartheta_2\,\cos\vartheta_{s,2}}{\sin\alpha_{ver}} \quad . \tag{3.39}$$

Now, we have all the quantities in 3.34 as functions of observables. The last thing we need to write down is the amplitude ϑ and φ as functions of the components of $\boldsymbol{\vartheta}$, ϑ_1 and ϑ_2, since we'll need to differentiate the lens equations in order to obtain the distortion matrix $\mathcal{D}$. These are simply

$$\tan\varphi = \frac{\tan\vartheta_2}{\tan\vartheta_1} \quad , \qquad \tan\vartheta = \frac{\tan\vartheta_1}{\cos\varphi} \quad , \tag{3.40}$$

where we may input the first equation in the second to get the explicit $\vartheta_{1,2}$ dependence for ϑ.

Coding all this into a ***Wolfram*** **Mathematica** notebook, we get an analytical map for quasi-equatorial gravitational lensing, as observed by an observer on the equatorial plane.

3.2.4 Distortion matrix $\mathcal{D}$: Image Shearing and Rotation

As a result of the previous sections, we have all the ingredients necessary to obtain the distortion matrix $\mathcal{D}_{ij} = \frac{\partial\Psi_i}{\partial\vartheta_j}$, which will be decomposed as in 1.40. We see that the components of the shear field $\boldsymbol{\gamma}$ and the rotation field ρ are [3]

$$\gamma_1 = \frac{1}{2}\left(\frac{\partial\,\Psi_2}{\partial\,\vartheta_2} - \frac{\partial\,\Psi_1}{\partial\,\vartheta_1}\right) \quad , \qquad \gamma_2 = -\frac{1}{2}\left(\frac{\partial\,\Psi_1}{\partial\,\vartheta_2} + \frac{\partial\,\Psi_2}{\partial\,\vartheta_1}\right) \quad , \tag{3.41}$$

[3] Note: we aren't actually interested in the convergence field, as it is related to the mass distribution of the lens which we are considering to be a point mass.

$$\rho = \frac{1}{2}\left(\frac{\partial\,\Psi_2}{\partial\,\vartheta_1} - \frac{\partial\,\Psi_1}{\partial\,\vartheta_2}\right) \ . \tag{3.42}$$

The shear field is a complex spin-2 field, and may be written as [27]

$$\gamma_{ab} = \gamma \begin{pmatrix} \cos\,2\omega & \sin\,2\omega \\ \sin\,2\omega & -\cos\,2\omega \end{pmatrix} \tag{3.43}$$

Thus, we can also characterise the shear field through its modulus, γ, and the rotation angle ω; explicitly,

$$\gamma = \sqrt{\gamma_1^2 + \gamma_2^2}\ , \qquad \omega = \ \frac{1}{2}\,\cos^{-1}\left(\frac{\gamma_1}{\gamma}\right). \tag{3.44}$$

These quantities are important, as it is straightforward to quantify the shear field's distorting action on an elliptic source as direct function of these. This works as follows: given an ellipse $\mathcal{E}$ with major axis a and minor axis b, its *ellipticity* is defined as

$$\epsilon = \frac{a-b}{a+b}\ .$$

As stated in [8], at first order in $\boldsymbol{\vartheta}$ the ellipticity (when $\kappa \approx 0$) is just[4]

$$\epsilon = \gamma\ . \tag{3.45}$$

Furthermore, the action of the shear field leaves the total surface area $A = \pi\,a\,b$ of $\mathcal{E}$ invariant. Keeping this in mind, one can write down the new a', b' of the deformed $\mathcal{E}$ as functions of the original ellipticity, a, b and γ. In the simplest case where $\mathcal{E}$ is a circle of radius R, the deformation of $\mathcal{E}$ will transform a and b as:

$$a' = R\sqrt{\frac{1+\gamma}{1-\gamma}}\ , \qquad b' = R\sqrt{\frac{1-\gamma}{1+\gamma}}\ . \tag{3.46}$$

Then, the image will be rotated by an angle ω, with respect to the y axis.
The action of the rotation field ρ adds onto the shear angle ω, as shown in [28]. Effectively, we may consider the asymmetric distortion matrix $\mathcal{D}$ as the product of a symmetric $\mathcal{D}_s$ and a rotation matrix $\mathcal{R}$,

$$\mathcal{R} = \begin{pmatrix} \cos\Phi & \sin\Phi \\ -\sin\Phi & \cos\Phi \end{pmatrix}\ ,$$

which implies that the shear field gets rotated in every point by an angle $\frac{\Phi}{2}$, $\tan\Phi = -\rho$ (when $\kappa = 0$). So the total rotation X that an ellipse undergoes in every point of the sky is $X \approx \omega + \rho/2$.

In the end, we have a ***Wolfram*** **Mathematica** code with explicit functions $\boldsymbol{\gamma}\,(\boldsymbol{\vartheta}, a, m)$, $\rho\,(\boldsymbol{\vartheta}, a, m)$ and $\gamma\,(\boldsymbol{\vartheta}, a, m)$, $\omega\,(\boldsymbol{\vartheta}, a, m)$. We can test the code by inputting values of $(\boldsymbol{\vartheta}, a, m)$ and see how the functions behave, and in particular verify that as $a \to 0$ we see Schwarzschild-like behaviour. We can also draw a map of the sky and visualise the distortion of elliptical background sources by a rotating compact mass.

[4]Note: this only holds in the weak lensing case, when $|\boldsymbol{\gamma}| \ll 1$.

3.3 Reality Check: Recovery of Schwarzschild and Numerical Examples

In this Section, we implement the tools developed up to now and verify that the results are compatible and coherent with what is expected. Throughout this whole section, the distances D_L and D_{LS} are taken to be equal and $D_L = 100$ Mpc.

3.3.1 On the Equatorial Plane

It is trivial yet instructive to compare our Kerr map to the Schwarzschild one in Chapter 1 when the source lies on the equatorial plane. In fact, in this case the motion occurs on a single plane, and both $\vartheta_2 \equiv 0$, $\varphi \equiv 0$. Then we can analytically compare 1.18 to 3.23, and see the contribution due to a:

$$\alpha_{equ} = 4\left(\frac{m}{b}\right) + \left(\frac{15\pi}{4} - 12\,\mathsf{s}\,\frac{a}{m}\right)\left(\frac{m}{b}\right)^2 + \left(\frac{128}{3} - 10\pi\,\mathsf{s}\,\frac{a}{m} + 4\left(\frac{a}{m}\right)^2\right)\left(\frac{m}{b}\right)^3 + \dots \,. \tag{3.47}$$

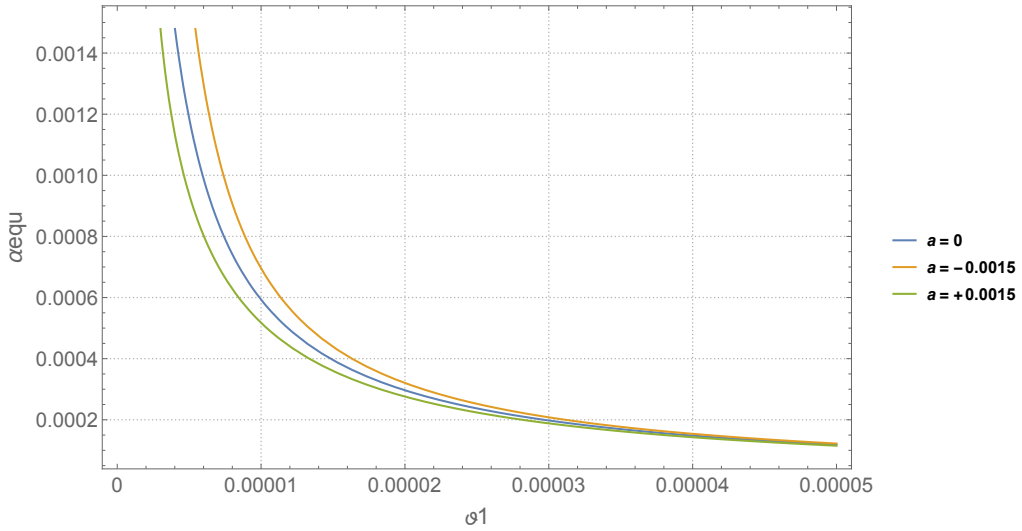

Figure 3.5: A plot of the bend angle α as a function of $\theta_1 \propto b$ in the case motion happens on the equatorial plane, in three different cases: $a = 0$, which is the Schwarzschild case, $\mathsf{s} > 0$ and $\mathsf{s} < 0$, which is equivalent to describing prograde and retrograde motion. We've inputted $m \sim 10^{12}\, M_\odot$ as mass parameter[5]. Note: in the plot, a does not correspond to the parameter a as it appears in 3.47, rather, it is a rescaled quantity: $\mathsf{a} = a\,\frac{R_g}{m}$, with $R_g \sim 100$ kpc. We will justify this rescaling in Chapter 4, when we look at a possible application of this lensing map.

Evidently, at first order in a, $\alpha_{equ} > \alpha_{Schw}$ when the sign of the angular momentum is $\mathsf{s} < 0$, which implies retrograde motion with respect to the travelling light ray, and vice versa $\alpha_{equ} < \alpha_{Schw}$ when $\mathsf{s} > 0$, for prograde motion; see Figure 3.5.

[5]Remember: $m = \frac{G\,M}{c^2}$, $c \equiv 1 \equiv g$.

3.3.2 Region of Validity

To make a proper use of the map we've constructed, it is essential to fully understand its region of validity on the image plane, spanned by the angles (ϑ, φ), where ϑ is the modulus of $\boldsymbol{\vartheta}$. For this discussion, we will use these angles and not $(\vartheta_1, \vartheta_2)$ to make our case.

First of all, consider the expansions we've done in Section 3.2: we've considered φ to be small, which implies that we'll be looking at a wedge of the sky. The map cannot be used around the z axis, where $\varphi \to \frac{\pi}{2}$.
We assess the error committed in our approximations by looking at the Schwarzschild bend angle $\boldsymbol{\alpha}$, which we know very well, and comparing it to the bend angle we find by setting $a = 0$. In other words, we compare the angle α calculated in Chapter 1, 1.18 to the amplitude we get setting $a = 0$,

$$\hat{\alpha}|_{a=0} = \sqrt{\alpha_{hor}^2|_{a=0} + \alpha_{ver}^2|_{a=0}} \ . \tag{3.48}$$

The Schwarzschild case is spherically symmetric, so the amplitude of the bend angle is the same around the origin, at fixed impact parameter b. It may be decomposed on any chosen orthogonal planes, and recalling the formalism we used in Chapter 1 and specifically looking at Figure 1.6, we may fix an orthogonal base and call φ the rise of the motion plane off of the (xy) plane. Thus, the physical bend angle α may be decomposed in its horizontal and vertical components via multiplication by $\cos\varphi$, $\sin\varphi$ in order; but the amplitude itself is φ independent. Yet, we see that $\hat{\alpha}|_{a=0}$ does not remain constant at constant b, varying φ, as there is a spurious φ dependence in the components α_{hor} and α_{ver}. The approximation must break down at a certain order of φ, so

$$\hat{\alpha}|_{a=0} = \alpha + \text{const.}\, \varphi^n + \mathcal{O}(\varphi^{n+1}) \ . \tag{3.49}$$

Then we fix b and look at

$$\ln\left(\frac{\hat{\alpha}|_{a=0}}{\alpha} - 1\right) = n \ \ln\varphi + \text{const.} \ ; \tag{3.50}$$

performing a parametric plot with **Wolfram** ***Mathematica*** we find $n \approx 4$. This agrees with an expansion of the true components of $\boldsymbol{\alpha}$ up to third order in φ, in fact we can write

$$\alpha'_{hor} = \alpha\, \cos\varphi \approx \alpha\left(1 - \frac{\varphi^2}{2} + ...\right) \ ,$$

$$\alpha'_{ver} = \alpha\, \sin\varphi \approx \alpha\left(\varphi - \frac{\varphi^3}{6} + ...\right) \ ,$$

and take

$$\alpha' = \sqrt{(\alpha'_{hor})^2 + (\alpha'_{ver})^2} \approx \alpha\sqrt{1 - \frac{\varphi^4}{12}} \approx \alpha\left(1 - \frac{\varphi^4}{24}\right) \ , \tag{3.51}$$

where the second and third order terms in φ have cancelled out. Thus, we conclude that our estimate of the total bend angle $\boldsymbol{\alpha}$ is accurate up to fourth order in φ, and we will choose our values of $(\vartheta_1, \vartheta_2)$ accordingly when mapping out a wedge of the sky.

3.3.3 The Point-Mass Model

To do a robust reality check and compare our results with literature, we first need to choose a comparison model. So, we look at the canonical point-mass lens, which is effectively a first order Schwarzschild lens, and constitutes a differentiable off-the-plane map. In this case, the 2-dimensional deflection angle $\boldsymbol{\alpha}$ is written out as a function of the impact parameter $\boldsymbol{b}$, which is in turn a function of the 2-dimensional observable angle $\boldsymbol{\vartheta}$ [29]:

$$\boldsymbol{\alpha} = 4\,m\,\frac{\boldsymbol{b}}{|\boldsymbol{b}|^2}\ , \qquad \boldsymbol{b} = D_L\,\boldsymbol{\vartheta}\ . \tag{3.52}$$

One can immediately see, comparing with 1.18, that this is just the extension in 3-dimensional space of the first order expansion in $\frac{m}{b}$ of the bend angle α calculated in the Schwarzschild metric. Inserting 3.52 in the lens equation 1.29 one obtains an easy expression for the image position $\boldsymbol{\Psi}$ as a function of $\boldsymbol{\vartheta}$,

$$\boldsymbol{\Psi} = \boldsymbol{\vartheta} - \vartheta_E^2\,\frac{\boldsymbol{\vartheta}}{|\boldsymbol{\vartheta}|^2}\ , \qquad \vartheta_E^2 = 4\,m\,\frac{D_{LS}}{D_L\,D_S}\ , \tag{3.53}$$

where ϑ_E is known as the Einstein angle. The distortion matrix $\mathcal{D}$ is then simply,

$$\mathcal{D} = \begin{pmatrix} 1 + \vartheta_E^2\,\frac{\vartheta_1^2-\vartheta_2^2}{|\boldsymbol{\vartheta}|^4} & 2\,\vartheta_E^2\,\frac{\vartheta_1\,\vartheta_2}{|\boldsymbol{\vartheta}|^4} \\ 2\,\vartheta_E^2\,\frac{\vartheta_1\,\vartheta_2}{|\boldsymbol{\vartheta}|^4} & 1 - \vartheta_E^2\,\frac{\vartheta_1^2-\vartheta_2^2}{|\boldsymbol{\vartheta}|^4} \end{pmatrix}\ , \tag{3.54}$$

so in this case we have

$$\kappa \equiv 0\ , \qquad \gamma_1 = -\vartheta_E^2\,\frac{\vartheta_1^2-\vartheta_2^2}{|\boldsymbol{\vartheta}|^4}\ , \qquad \gamma_2 = 2\,\vartheta_E^2\,\frac{\vartheta_1\,\vartheta_2}{|\boldsymbol{\vartheta}|^4}\ , \qquad \rho \equiv 0\ . \tag{3.55}$$

We will use this as a reference and compare our results to this first order solution.

3.3.4 The Action of $\boldsymbol{\gamma}$ and ρ

We finally look at the effects of rotation on the distortion matrix $\mathcal{D}$, and proceed to map them out in the region of the sky our map is valid.
We choose unrealistic values for parameters (a, m) to enhance the effect of rotation on the distorted background; we discuss possible physical values for these parameters in Chapter 4 where we treat the case of rotating galaxies.
The following plots have been produced using the *Python* package, making use of the formulas relevant to the distortion of an elliptical source presented in subsection 3.2.4, considering these sources to be circular.
Notice the differences between the plots of the action of the shear and shear + rotation fields on the same patch of sky in the point mass and in the Kerr case, Figures 3.6 and 3.7 respectively: one can clearly see that in the Kerr case the shear field is asymmetrical with respect to the z axis, and in particular weaker for retrograde rays, and stronger for prograde rays, compared to the point mass case. The inputted mass parameter for these plots is of course the same, to allow the comparison.

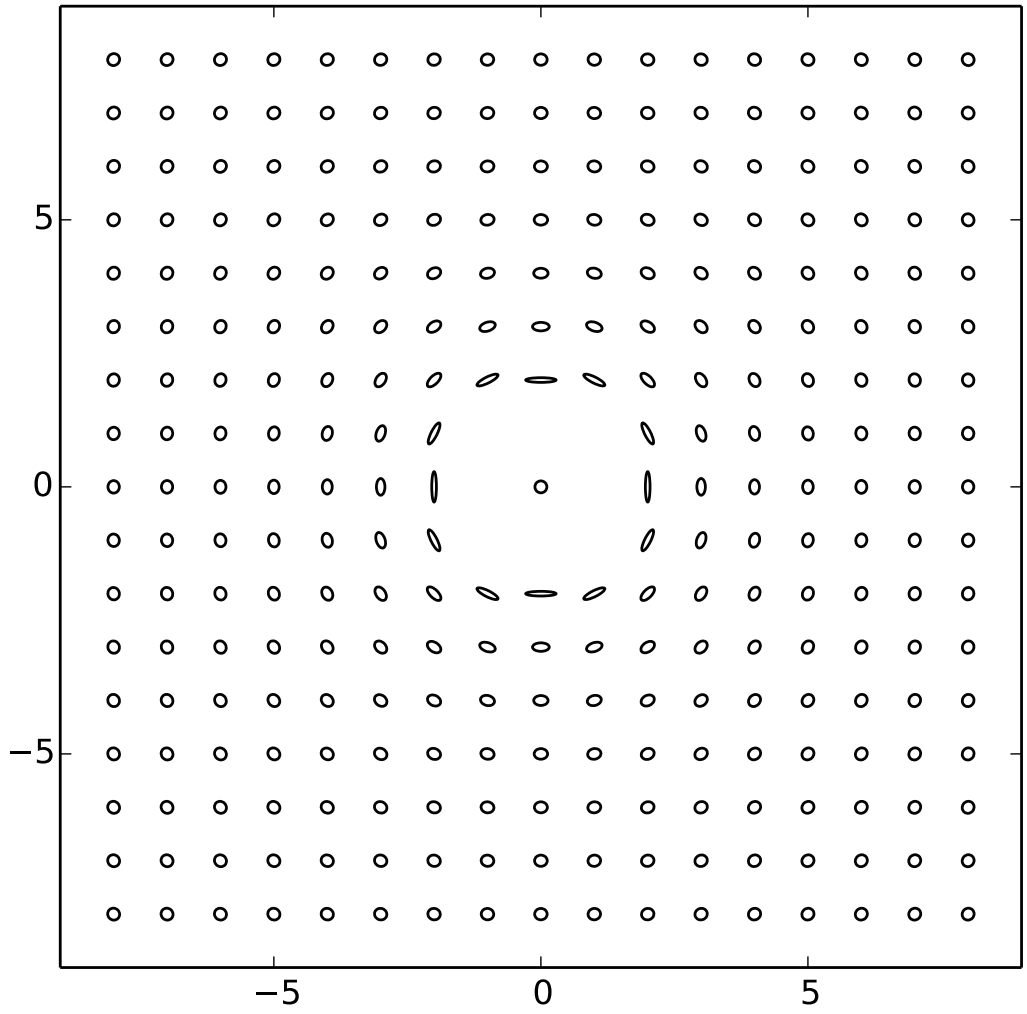

Figure 3.6: We map the effect of the shear field generated by a point mass on a background of circular sources, in a region of 5 square arcminutes on the sky. The effect is symmetric and decreases rapidly with b. For this picture, we've used a value for the Einstein angle of $\vartheta_E = 10^{-4} \sim 10$ arcsec, which corresponds to a mass of $5 \cdot 10^{12}\, M_\odot$.

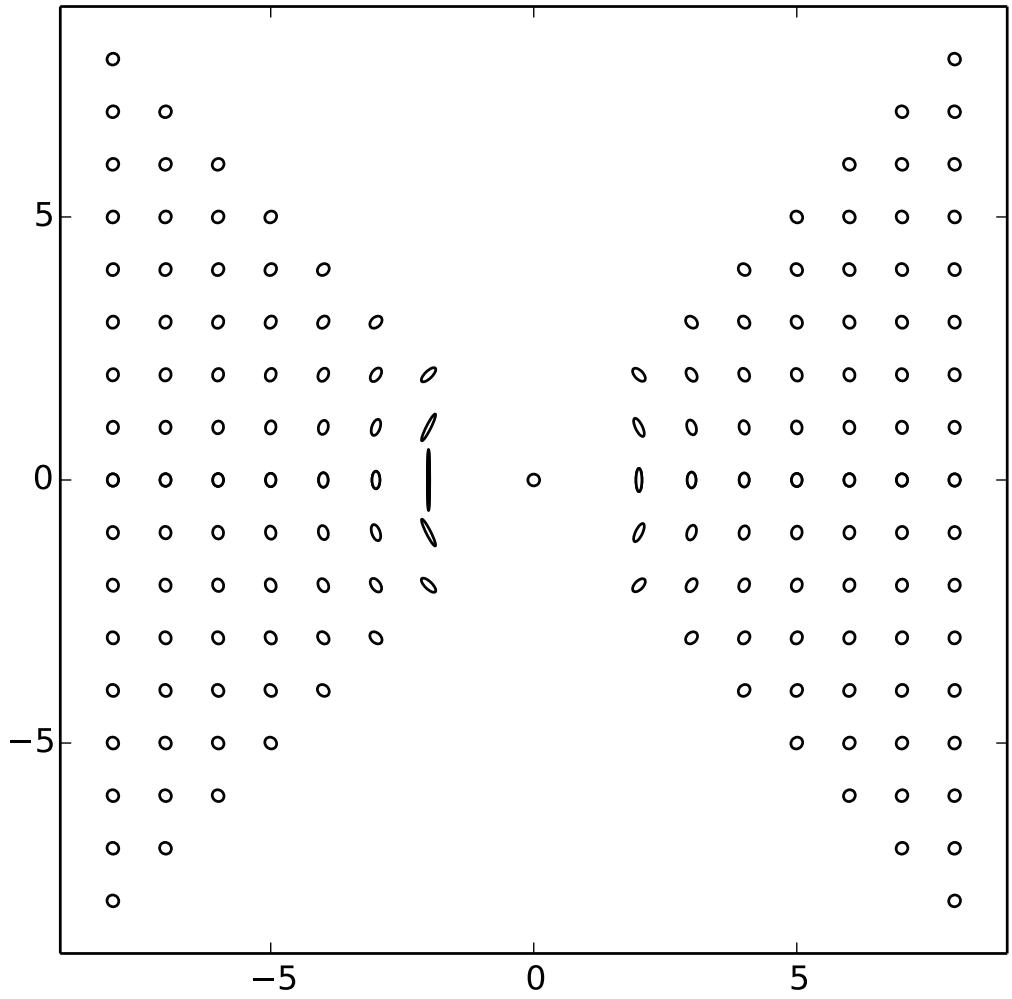

Figure 3.7: We take a region of 5 square arcminutes of the sky around a Kerr lens, and plot the effect of distortion brought upon a grid of circular sources. To produce a substantial effect, we input the values $m = 5{\cdot}10^{12}\, M_{\odot}$, $\mathsf{a} = 0.015$ (for a description of the a parameter, see the caption of Figure 3.5). These are rather nonphysical values, but it is instructive to produce an image with an effect visible to the naked eye. Note the asymmetry with respect to the z axis: the modulus of the shear field is different depending on what side the the light approaches the lens, and one may also notice slight changes of inclination in the rotation angle. However, the effect of the shear field $\boldsymbol{\gamma}$ largely overshadows that of ρ, so we will have a closer look at the latter. It's important to point out that the distortion which may be observed closest to the point mass is unrealistic: for such values of b, one would expect also an overall arching of the image, as in an Einstein ring. Closer to the lens, the weak lensing approximation breaks down as $\gamma > 1$.

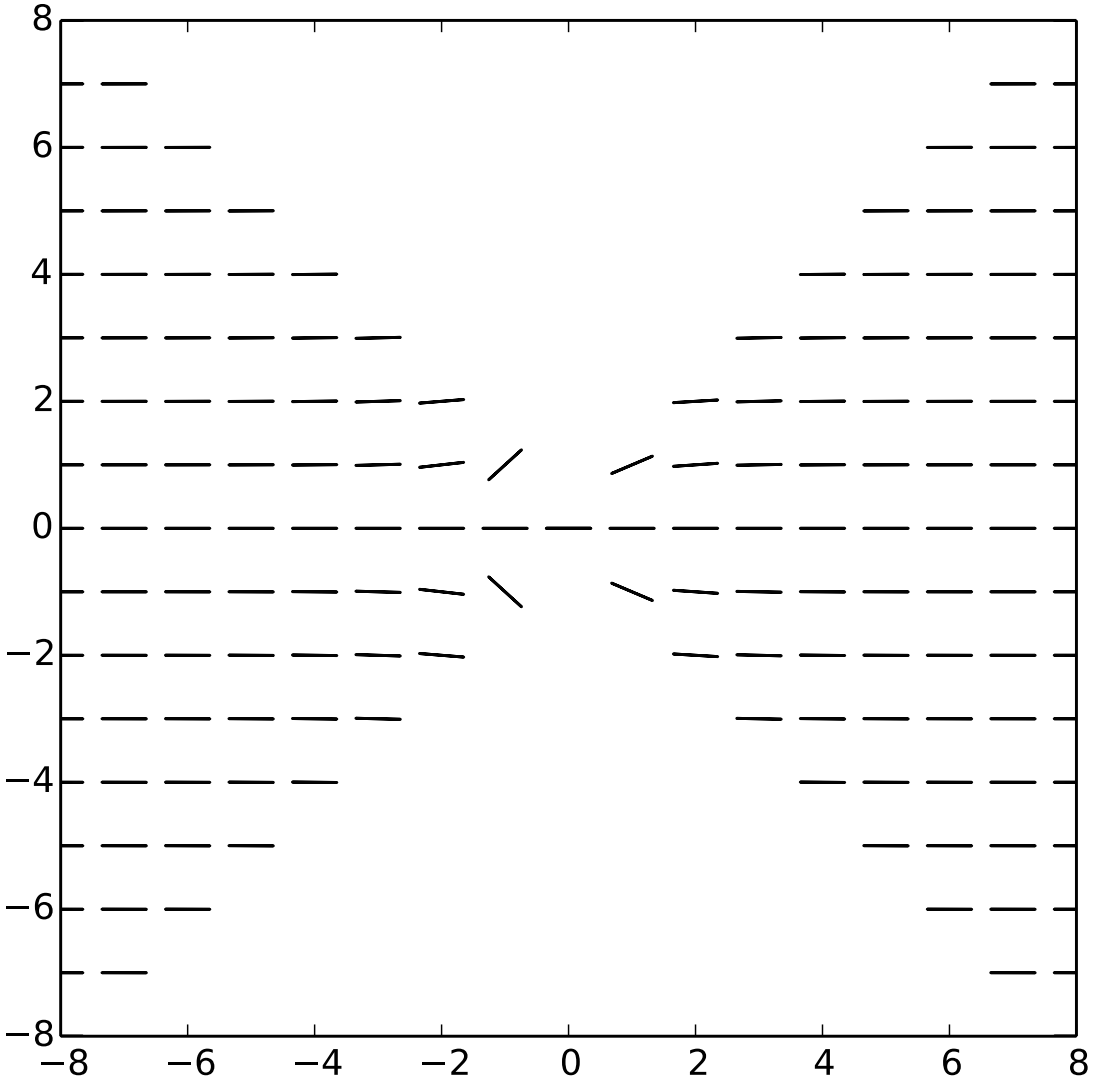

Figure 3.8: We plot out just the effect of the ρ field on a grid of vectors, to better visualise its effect. Note how the effect is not axially symmetric with respect to z, and as such it behaves just like a B-mode, described in Chapter 1.3. The values inputted for this plot are $m = 10^{12}\, M_{\odot}$, $\mathsf{a} = 0.015$.

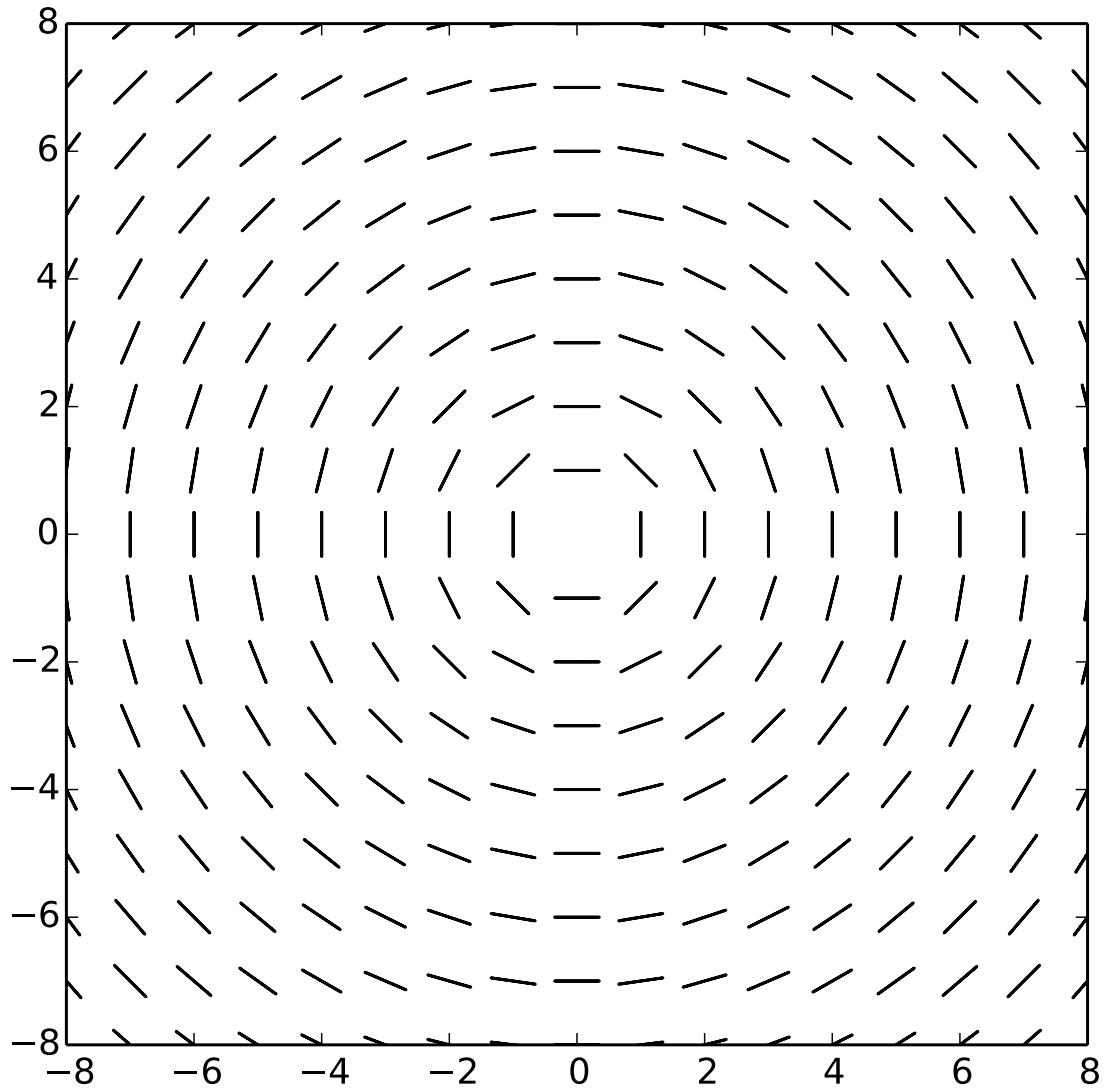

Figure 3.9: A representation of the action of ω on a field of vectors - extending the action on the z axis by continuity. The parameters for this plot are $\mathsf{a} = 0.0015$, $m = 10^{12}\, M_{\odot}$.

The rotation angles ω and ρ. It is instructive to discuss the two angles which contribute to image distortion, at fixed parameters. Effectively, ω quantifies the inclination of the major axis of the distorted ellipse with respect to the y axis; as such, it is exactly 0 on the equatorial plane, $\frac{\pi}{4}$ along the diagonal ($y = z$, i.e. $\vartheta_1 = \vartheta_2$) and, if our map were extendable, $\frac{\pi}{2}$ on the z axis. Extending the analysis to all four quadrants of the sky around the lens, clearly ω may span $[0, 2\pi]$ - see Figure 3.9. ρ, as explained at the end of Chapter 3.2.4, is essentially the rotation angle (at first order in the observable angles) which is to be added to ω in the presence of an asymmetric mode. We see that it is a tiny contribution to ω in Figure 3.10.

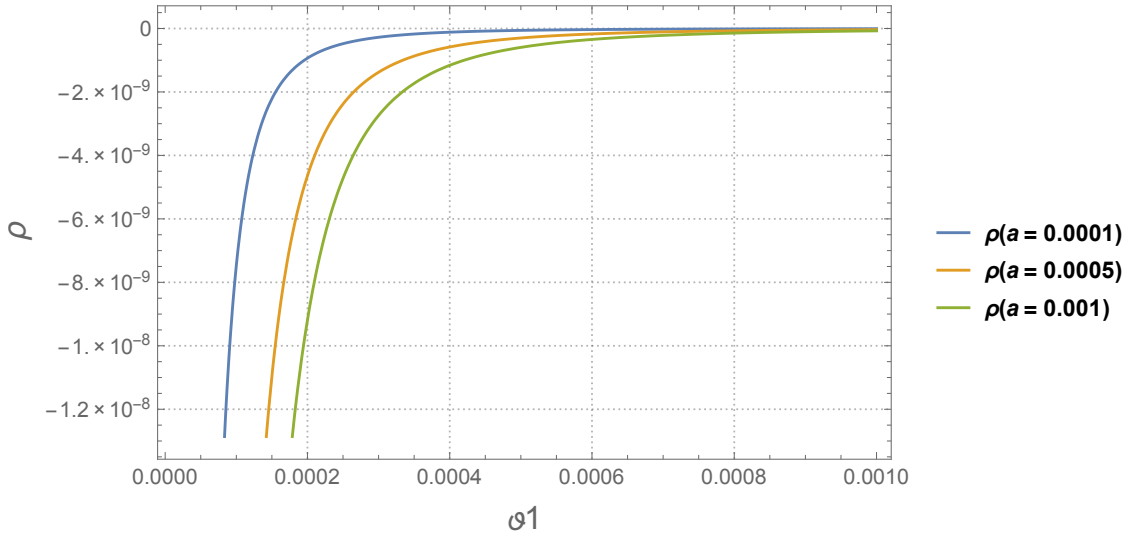

Figure 3.10: A plot of ρ at different values of the rescaled rotation parameter a, keeping the impact and mass parameters fixed ($\vartheta = 0.0003$, $m = 10^{12}\, M_{\odot}$).

γ in Schwarzschild and Kerr. To check that the map behaves smoothly, we look at the shear field in both cases, and interpret the action of the rotation represented by the parameter a. Also, we verify that the modulus of the shear field γ is symmetric around the origin when we shut off rotation.
One may see from Figure 3.11 that rotation modifies continuously the behaviour of the two components of the shear field, γ_1 and γ_2. In particular, for positive a and in the first quadrant[6], we have less negative values for both γ_1 and γ_2, compared to the $a = 0$ case. We remind the reader that the distorting action of the separate components of the shear field is illustrated in Figure 1.8.

[6]The first quadrant is identified by $\vartheta_1 > 0$, $\vartheta_2 > 0$.

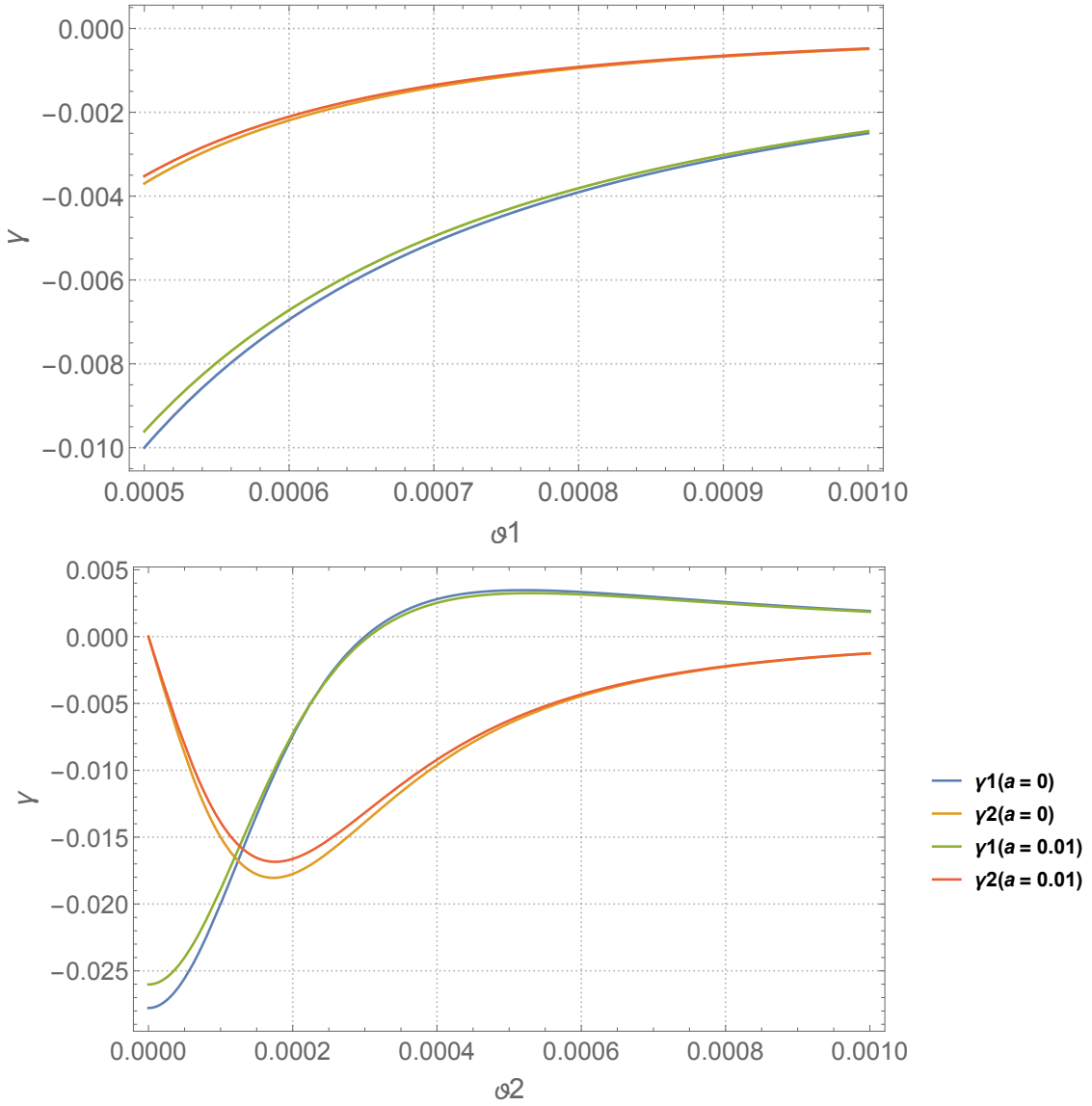

Figure 3.11: Top: a comparative plot of the components of the shear field γ_1, γ_2 at fixed values of ϑ_2, m ($\vartheta_2 = 10^{-6}$ rad for γ_1, $\vartheta_2 = 10^{-3}$ rad for γ_2), varying ϑ_1 respecting the region of validity, in the two cases $a = 0$ (Schwarzschild) and $a \neq 0$ (Kerr). Bottom: a plot of γ_1, γ_2 at fixed values of ϑ_2, m ($\vartheta_1 = 0.0003$), varying ϑ_2 respecting the region of validity, in the two cases $a = 0$ and $a \neq 0$. $m = 10^{12}\, M_\odot$ for all lines. The choice of all parameters was made bearing in mind the interpretive value of the plots.

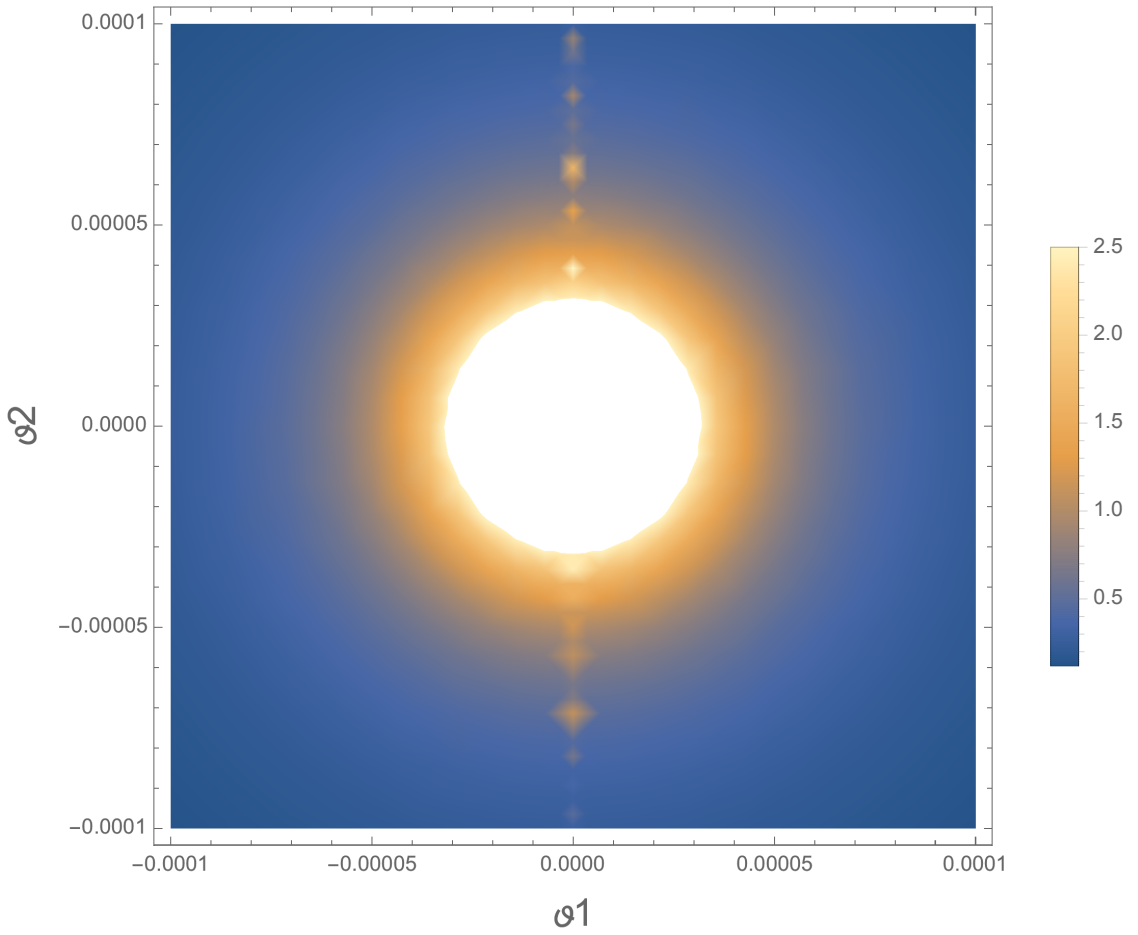

Figure 3.12: A density plot of the modulus of the shear field $\gamma(\boldsymbol{\vartheta}, a = 0, m)$. Note the radial symmetry; disregard the ϑ_2 axis, which corresponds to the z axis: the map breaks down along z, as we've discussed.

ρ as a function of (a, m). We study the behaviour of the ρ field as a function of rotation and mass, so as to get a better idea of what influences the asymmetric part of the distortion matrix most.

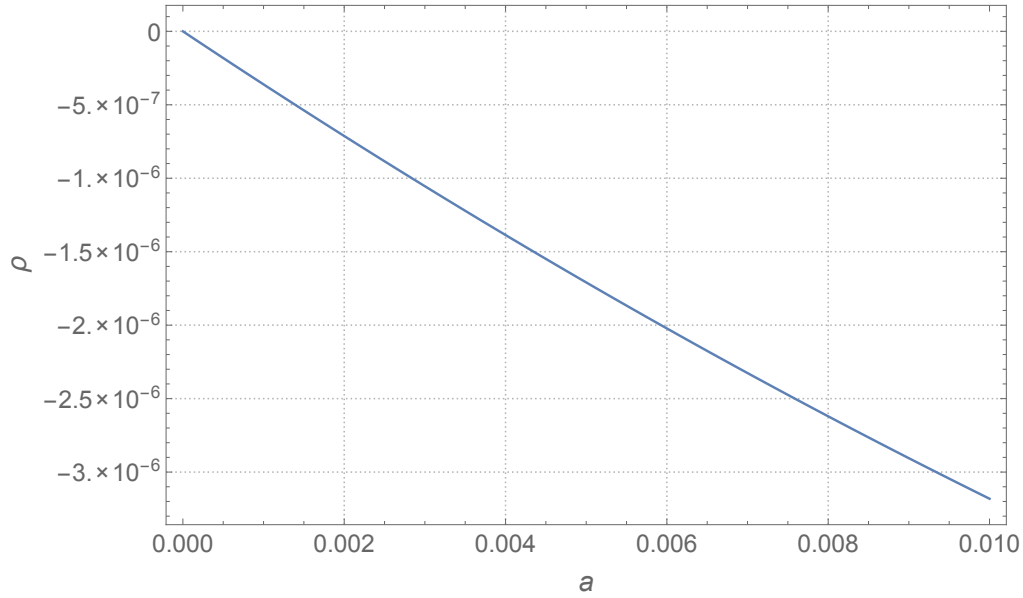

Figure 3.13: A plot of ρ as a function of the rescaled rotation parameter a, keeping $\boldsymbol{\vartheta} = (10^{-4}, 10^{-6})$ rad, $m = 10^{12}\, M_{\odot}$ fixed. Note the approximately linear behaviour in the range of a we've selected.

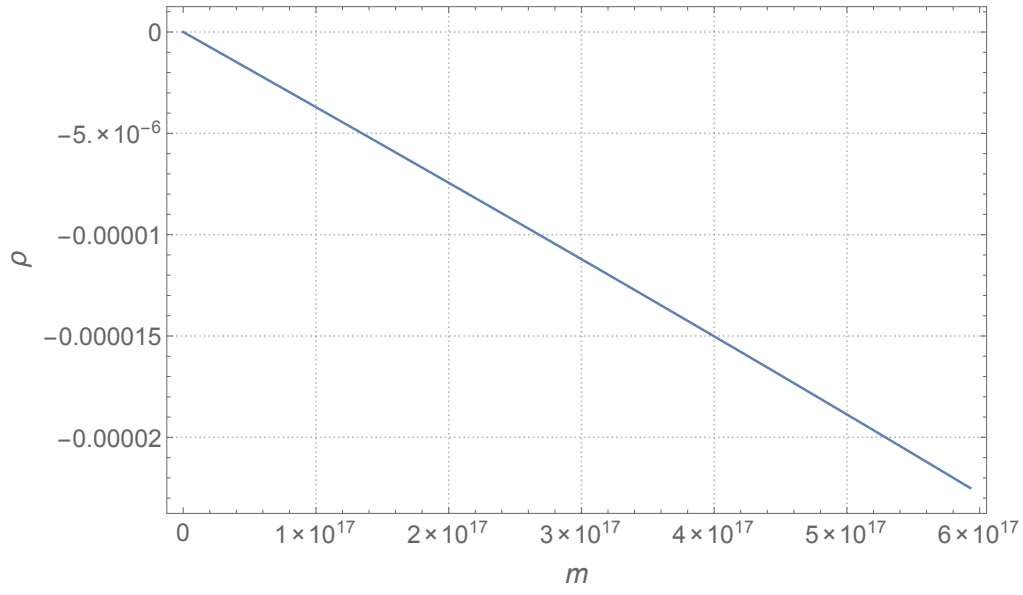

Figure 3.14: A plot of ρ as a function of the mass parameter m, keeping $\boldsymbol{\vartheta} = (10^{-4}, 10^{-6})$ rad, $\mathsf{a} = 0.00015$ fixed. Note the approximately linear behaviour in the range of m we've selected. m is expressed in metres in this plot.

Chapter 4

Discussion: $\frac{|B|}{|E|}$ for Rotating Galaxies

4.1 Rotating Galaxies and the Kerr Metric

As mentioned in Chapter 3, the Kerr metric isn't a static solution to Einstein's equations 1.2 and thus Birkhoff's theorem isn't applicable to the spacetime it defines. This implies that one may not in general describe the spacetime outside a rotating object with such metric, as one could describe a static star with the Schwarzschild metric. However, we have chosen to model rotating galaxies with the Kerr metric, well aware that this approximation breaks down in certain regions of spacetime. Let us review the main features of rotating galaxies, and then discuss the applicability of the Kerr metric to the case.

Rotating Galaxies. Rotating galaxies have an overall angular momentum, which is a residual product of galaxy formation. A good example of rotating galaxies are spiral galaxies such as the Milky Way: they are roughly in the shape of a flattened disk, as the centrifugal force spreads the stars out on the equatorial plane. They are particularly useful to us, as the equatorial plane is easy to spot and well defined (see Figure 4.1). Plus, they are certainly not uncommon: in fact, they are the most widespread type of galaxy in the overdense regions of the Universe.
The stars of the spiral disk travel in nearly circular orbits around the galactic centre, and their velocity v_c depends on their distance R from the galactic centre. A plot of $v_c(R)$ is called a *circular speed curve*, and it is nearly constant for spiral galaxies, even for R well beyond the R_g of the visible galaxy[30]; this implies the presence of a co-rotating dark matter halo. Typical circular speeds are $200 < v_c < 300\,km\,s^{-1}$, but it must be noted that the dark matter halo is somewhat slower than the luminous matter.
For a disk-like mass distribution,

$$v_{c,disk}\,(R) = \sqrt{\frac{G\,M(R)}{R}}\ ;$$

adding the dark matter component, one must include a damping factor λ, such that

$$v_c\,(R) = \lambda\sqrt{\frac{G\,M(R)}{R}}\ ,$$

Figure 4.1: This Hubble image released on the 25/1/2016 shows spiral galaxy LO95 0313-192, which is located roughly one billion light-years away, on the left; on the right, LOY2001 J031549.8-190623. Notice their spiral structure and thin disk shape.

(typically for a spiral galaxy one has $\lambda \sim 0.05$, when including the effect of dark matter). The fact that v_c is empirically shown to be roughly constant gives information regarding the mass distribution $M(R)$.
To describe a spiral galaxy as a compact disk, we then need it's maximum radius R_{max} and total mass $M(R_{max})$, plus it's angular momentum J which will depend on these and the circular velocity. Up to form factors, $J = R_{max}\, M\, v_c$.

The main issue we encounter when describing a rotating galaxy through the Kerr metric is that the galaxy is a large, spread out object with $R_{max} \gg R_{Schw}$, where $R_{Schw} = \frac{2\,M\,G}{c^2} \equiv 2\,M_\bullet$. As we've done throughout Chapters 1 and 3, we assume that the impact parameter b is much larger than the Schwarzschild radius; thus, we're looking at a region of space which is well away from the Kerr horizon, and we don't expect it to be sensitive to the difference in nature between a Kerr black hole and a spinning spiral galaxy.
The fact that a galaxy is significantly more spread out than a black hole also means that its angular momentum may be much greater, at fixed mass. In fact, if we look at the mass-scaled angular momentum a as it is defined for the Kerr metric,

$$a = \frac{J}{M_\bullet} = \frac{J}{2\,R_{Schw}} \ ,$$

we find that it isn't a small parameter at all, and it makes no sense to look at first order contributions to the bend angle in it. To use it properly and obtain an expansion parameter, we should scale it by the radius of the galaxy R_g. In fact, if we take g_{tt} of the Kerr metric and expand it in $\frac{1}{R}$, restricting it to the equatorial plane ($\theta = \frac{\pi}{2}$) for simplicity:

$$g_{tt} = -\frac{R^2 + a^2 - 2\,M_\bullet\,R}{R^2 + a^2} \approx -1 + \frac{2\,M_\bullet}{R} - \frac{2\,a^2\,M_\bullet}{R^3} + ... \tag{4.1}$$

Then we see that the first Kerr contribution is of the order

$$\frac{a^2\,M_\bullet}{R^3} = \left(\frac{a}{R}\right)^2 \left(\frac{M_\bullet}{R}\right) \ ,$$

and since $M_\bullet \ll R_g < R$ as discussed before, we can use $\tilde{a} = \frac{a}{R_g}$ as an expansion parameter.

The Milky Way. In various simulations found in both the previous chapter and this one we use Milky Way-like parameters. The values of mass and radius typically associated to our own Galaxy are roughly

$$M_{MWay} = 10^{12}\,M_\odot \ , \qquad R_{MWay} = 100\,kpc \ . \tag{4.2}$$

The circular speed at solar radius R_0 is well known to be

$$v_c\,(R_0) = 220 \pm 15\,km\,s^{-1} \ ; \tag{4.3}$$

assuming the circular speed to be constant throughout the disk, we then input

$$v_{c,\,MWay} = 200\,km\,s^{-1} \tag{4.4}$$

in our calculations. Lastly, we need the rescaled angular momentum parameter $\tilde{a}$, which is found to be

$$\tilde{a}_{MWay} = 0.0015 \ , \tag{4.5}$$

inputting the quantities shown above. We've omitted error calculations in our simulations as these are highly preliminary tests and are only meant to assess the order of magnitude of the rotational effect, nothing more.

4.2 Measurability of E- and B- Modes of a Rotating Galaxy

Let us imagine we have a rotating lens, which produces a B-mode in the lensing pattern of background light sources. It is useful to estimate what the magnitude of the signal would be, and whether it would be at all discernible within present and/or future data. The two main projects which may provide useful observations for our purposes are the *Planck* space observatory and the *Euclid* space mission.

Planck is a space observatory which was operated by the European Space Agency (ESA) from 2009 to 2013. Its objectives included high resolution detections of both the total intensity and polarisation of primordial CMB anisotropies, surveys of the gravitational lensing of the CMB, detection of active galactic nuclei (AGNs) and infrared sources, plus a plethora of observations regarding our own Galaxy and Solar System [31]. *Planck*'s results exceeded expectations and data is available to use. *Planck* data is accurate enough to investigate background shearing; however, we exclude that it may be useful to distinguish the rotation field from the shear field.

Euclid is an exciting mission which has just recently passed it's preliminary design review, at the end of 2015, and is the natural continuation of *Planck*. Its primary goals are measuring the effects of weak gravitational lensing, baryonic acoustic oscillations and redshift-space distortion patterns in our Universe, so as to ultimately provide unprecedented quality data for the study of dark energy and dark matter [32]. The launch date is planned in 2020, and run time will be 6 years.

Also, the *Large Synoptic Survey Telescope* (LSST) may provide precious data regarding rotating lenses. LSST will be a wide field reflecting telescope, boasting the largest digital camera ever constructed (3.2 gigapixel CCD) [33]. It will map the entire available sky every few nights, delivering high definition images aimed for weak gravitational lensing measurements in the deep sky, the detection of transient optical events (e.g. novae and supernovae) and the general mapping of our Solar System and Galaxy. The telescope is currently being constructed on Cerro Pachòn, a mountain in the Coquimbo Region, Northern Chile; engineering completion is anticipated in 2019, and the run of the first ten-year survey is expected to commence in January 2022.

Euclid Simulations. To gauge our possibilities, we look at simulations of the shear power spectrum in the *Euclid Definition Study Report* [34]; see Figure 4.2 as an example. In this case, the region with highest sensitivity is around an amplitude of $10^{-5} \sim 10^{-4}$, with a sigma of 0.5%. Going through a rapid back-of-the-envelope calculation, considering the power spectrum to be roughly constant and averaging over the channels between $l \sim 10^3$ and $l \sim 10^4$, we estimate that according to the simulation for Euclid data in Figure 4.2 we could whittle down the sigma to 10^{-8}.
The shear power spectrum will be proportional to the modulus of the shear field squared, γ^2, and the same goes for the ρ power spectrum, ρ^2. For the latter to be distinguishable from the former, we need ρ^2 to be at least comparable to σ_{γ^2}. To check this, we take the squared ratio of the amplitude of the rotation field ρ and the shear field γ obtained through our map, inputting the parameters 4.2, 4.5 motivated above - a plotted example may be seen in Figure 4.3. Let's take $\frac{\rho^2}{\gamma^2} \sim 10^{-9}$ as a working value; then, multiplying by the simulated shear power spectrum in Figure 4.2 we'd get a value for the rotation power spectrum of $\rho^2 \sim 10^{-14}$, which is utterly negligible compared to $\sigma_{\gamma^2} \sim 10^{-8}$ obtained above.

Galaxy Stacking. We may be able to observe the lensing effect of galaxy rotation by stacking data of similar sources to build a significant signal. There are numerous galaxy catalogues where information such as mass, circular velocity and radius are stored; it is worth while to check whether we have knowledge of enough galaxies that fit the bill in order to stack them and observe a curl-like distortion.
Thanks to detailed spectroscopic analysis, it is possible to determine circular velocity and orientation of a spiral galaxy. This is simply done by measuring the redshift of its stars, on one side and the other of the rotation axis. We may consider future data from LSST or *Euclid*: the former should photograph around 100 galaxies per square arcminute, the latter about a third of this. Suppose a tenth of the galaxies in every square is a foreground galaxy and acts as a lens, and the rest lie on the background. Then, around a lens a circle of radius r (in arcminutes) will contain $\mathsf{n} = \mathsf{N}\,\pi\mathsf{r}^2$ galaxies, where we take $\mathsf{N} = 100$ for LSST. The variance of the shear field $\boldsymbol{\gamma}$, σ_γ, is dominated by the intrinsic ellipticity variance of

the lensed sources, which is typically $\sigma_e \approx 0.3$ [35]. We assume the σ_ρ of the rotation field to be roughly the same as σ_γ; then, for a single lens we should be sensitive to perturbations of order $\frac{\sigma_\gamma}{\sqrt{\mathsf{n}}}$. By stacking the lensing data, we can refine this by a factor $\frac{1}{\sqrt{\mathsf{M}}}$, where M is the number of stacked lenses. Then roughly

$$\sigma_\rho \sim \frac{0.3}{\mathsf{r}\sqrt{\mathsf{M}\,\mathsf{N}\,\pi}} \ .$$

One immediately realises that in order to get σ_ρ of the order of ρ_{galaxy} derivable with our map, one would need to stack a considerably large amount of spiral galaxies, and one would need to know beforehand their orientation - see Figure 4.4 as an example. These prerequisites combined bring us to a deadlock: current resolutions are not sufficient to discern the spiral structure of most galaxies and extrapolate their signed angular momentum.

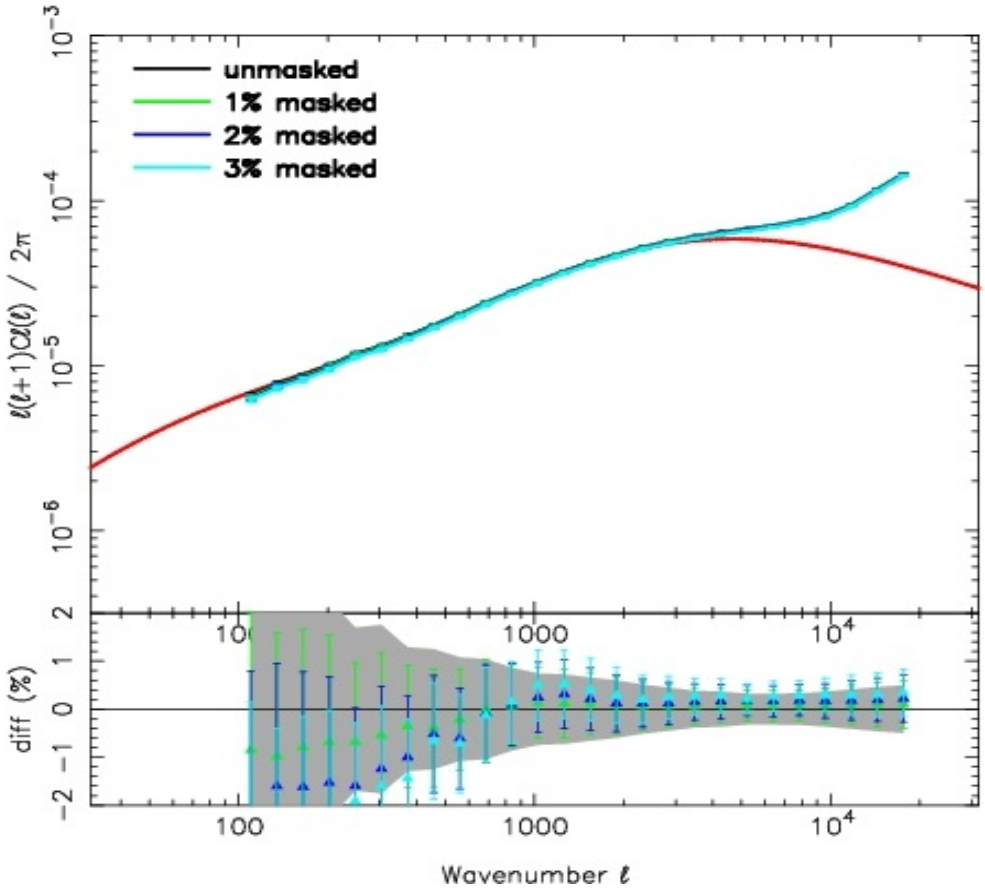

Figure 4.2: Simulated unmasked shear power spectrum and masked power spectra for a survey, drawn from the *Euclid Definition Study Report* [34]. The masking method is one of the tools developed by the *Euclid* collaboration to take into account the effect of foreground stars, glitches and cosmic rays on the shear power spectrum. The lower panel shows the percentage difference between the unmasked and masked power spectra as compared with the theoretically expected power spectrum; the grey region shows the 1σ error on the unmasked power spectrum.

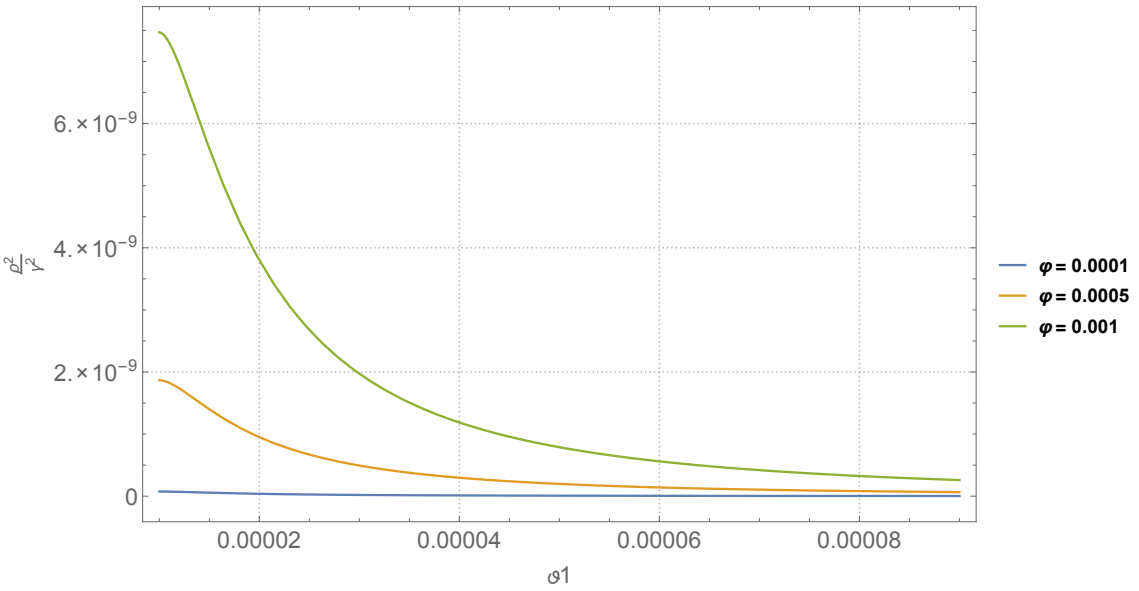

Figure 4.3: A plot of the ratio $\left(\frac{\rho}{\gamma}\right)^2$ as a function of ϑ_1 for different fixed φ, with the following parameters: $m = 10^{12}\, M_{\odot}$, $\tilde{a} = 0.0015$, $R_g = 100\, Kpc$. These are the parameters associated to the Milky Way, previously motivated.

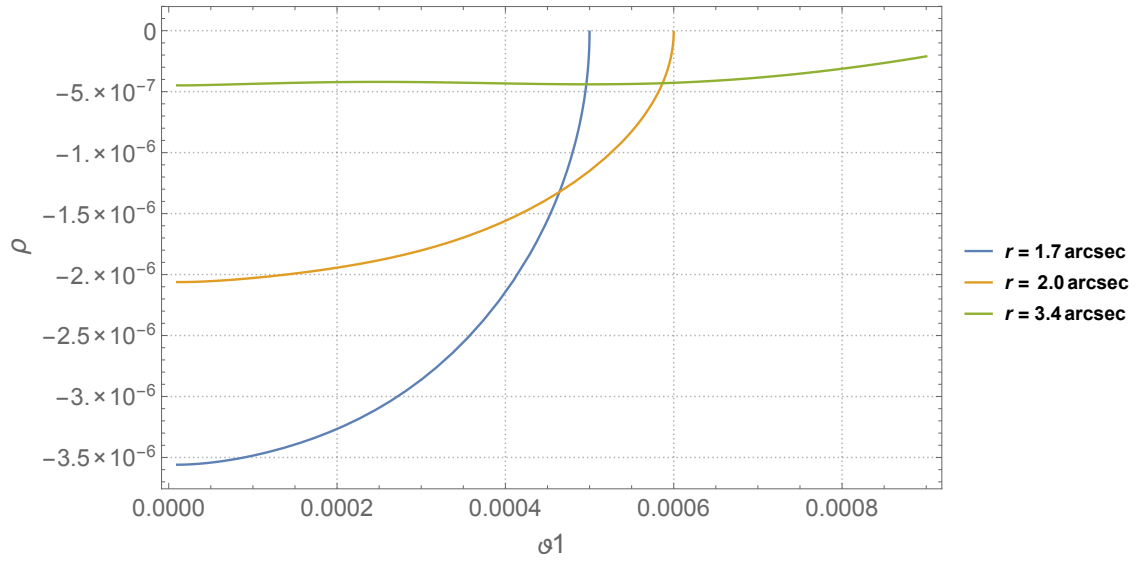

Figure 4.4: A plot of the ρ field as a function of ϑ_1 for different fixed r, with mass and angular momentum parameters associated to the Milky Way.

Chapter 5

Conclusions

We've successfully developed a differentiable lensing map in the Kerr spacetime, and obtained expressions for the shear and rotation fields. This calculation has value in itself, as an instructive result which doesn't appear in the literature. The action of a Kerr-like object on a background of circular sources is illustrated in Figures 3.7 and 3.8, where we've used nonphysical parameters to enhance the effect, as it is very small. We've also verified the trend of these fields with respect to the parameters of the case, (a, m).
We believe this to be a good example of the lensing effect induced by a vector perturbation on a background of light sources. From a theoretical point of view, this is precious information as there are few instances of lensing models by vector perturbations in the literature.

We approximate rotating galaxies with the Kerr metric (well aware of the caveats of the case), to estimate the possible effect these may have on background radiation. Comparing our results with *Euclid* simulations, we find that it is highly unlikely to be able to distinguish the rotation field from the shear field, and/or noise.
Thus, we conclude that the experimental applications of this map are as of now quite limited, given the sensibility expectations for current and near-future experiments. We await highly futuristic data to put this work to good use.

Appendix A

Proof of Decomposition Theorem

Following Appendix B of [14], we outline the proof of the following theorem:

Th. *A covariant linear differential equation of second order at most on the invariant n-space Σ with intrinsic metric γ_{ij} can be decomposed into mutually decoupled equations, each of which contains only one type of components of the unknowns.*

Before we proceed, let us recall the Riemann and Ricci tensors,

$$R^i{}_{jkm} = \nabla_k \Gamma^i{}_{jm} - \nabla_m \Gamma^i{}_{jk} + \Gamma^i{}_{kl}\,\Gamma^l{}_{jm} - \Gamma^i{}_{ml}\,\Gamma^l{}_{jk} \ , \tag{A.1}$$

$$R_{ij} = R^l{}_{ilj} \ ; \tag{A.2}$$

let us remind the reader that the Riemann tensor A.1 is defined by

$$[\nabla_i, \nabla_j]\ v_k = R^l{}_{kij}\, v_l \ , \tag{A.3}$$

and it contains all the information regarding curvature of the manifold it pertains to. We will make use of the following relations valid for scalar functions f, vector functions $\boldsymbol{v}$, and tensor functions $\boldsymbol{T}$, remembering $\Delta = \gamma^{ij}\,\nabla_i\nabla_j$:

$$(\nabla_i\Delta - \Delta\nabla_i)\, f = -R_{ij}\,\nabla^j f \ , \tag{A.4}$$

$$(\nabla_i\Delta - \Delta\nabla_i)\, v_j = 2\,R_i{}^k{}_j{}^m\,\nabla_k\, v_m - R_{ik}\,\nabla^k v_j + (\nabla_k\, R_i{}^k{}_j{}^m)\, v_m \ , \tag{A.5}$$

$$\begin{aligned}(\nabla_i\Delta - \Delta\nabla_i)\, T_{jk} =& 2\,R_i{}^m{}_j{}^p\,\nabla_m\, T_{pk} + 2\,R_i{}^m{}_k{}^p\,\nabla_m\, T_{jp} - R_{im}\,\nabla^m T_{jk} + \\ &+ (\nabla_m\, R_i{}^m{}_k{}^p)\, T_{jp} + (\nabla_m\, R_i{}^m{}_j{}^p)\, T_{pk} \ .\end{aligned} \tag{A.6}$$

Proof. All the scalar, vector and tensor quantities obtainable by operating differential operators of the second order at most on f, $\boldsymbol{v}$ and symmetric $\boldsymbol{T}$ are the following:

Scalar:

$$\begin{aligned}&f \ , \qquad \boldsymbol{\nabla}\cdot\boldsymbol{v} \equiv \Delta\, v \ , \qquad \gamma_{ij}\, T^{ij} \equiv t \ , \qquad \Delta\, t \ , \\ &\nabla_i\,\nabla_j\,\left(T^{ij} - \frac{1}{n}\,\gamma^{ij}\, t\right) \equiv \frac{n-1}{n}\,(\Delta + n\,k)\,\Delta\, s \ .\end{aligned} \tag{A.7}$$

Vector:

$$\begin{aligned}
&\nabla_i f\ , \qquad v^i \equiv v_v^i + \nabla^i v\ , \qquad \Delta\, v^i \equiv \Delta\, v_v^i + \nabla^i \left[\Delta v + (n-1)\, k\, v\right]\ , \\
&\nabla_i t\ , \qquad \nabla_i \Delta\, t\ , \\
&\nabla_j \left(T^{ij} - \frac{1}{n}\,\gamma^{ij}\, t\right) \equiv \left[\Delta + (n-1)\, k\right] T_v^i + \frac{n-1}{n}\,\nabla^i \left(\Delta + n\, k\right) s\ .
\end{aligned} \tag{A.8}$$

Tensor:

$$\begin{aligned}
&\gamma_{ij}\, f\ , \qquad \left(\nabla_i \nabla_j - \frac{1}{n}\,\gamma_{ij}\,\Delta\right) f\ , \qquad \gamma_{ij}\,\Delta\, f\ , \\
&\gamma_{ij}\,\nabla_k\, v^k \equiv \gamma_{ij}\,\Delta v\ , \\
&\nabla_i\, v_j + \nabla_j\, v_i \equiv \left(\nabla_i\, v_{vj} + \nabla_j\, v_{vi}\right) + 2\left(\nabla_i \nabla_j - \frac{1}{n}\,\gamma_{ij}\,\Delta\right) v + \frac{2}{n}\,\gamma_{ij}\,\Delta v\ , \\
&T^{ij} \equiv T_t^{ij} + \left(\nabla^i\, T_v^j + \nabla^j\, T_v^i\right) + \left(\nabla^i\,\nabla^j - \frac{1}{n}\gamma^{ij}\,\Delta\right) s + \frac{1}{n}\, t\,\gamma^{ij}\ , \\
&\gamma^{ij}\, t\ , \qquad \gamma^{ij}\,\Delta t\ , \qquad \nabla^i\,\nabla_k\, T^{jk} - \frac{2}{n}\,\nabla^i\,\nabla^j\, t \\
&\gamma_i j\,\nabla_k\,\nabla_m\, T^{km}\ , \qquad \Delta T_{ij}\ .
\end{aligned} \tag{A.9}$$

As in Chapter 2, v and v_v^i are respectively the scalar and vector component of $\boldsymbol{v}$, $(s,\, t)$, $\boldsymbol{T}_v$ and $\boldsymbol{T}_t$ are the scalar, vector and tensor components of $\boldsymbol{T}$.
In A.7 all the quantities are expressed in terms of the scalar components of the functions f, $\boldsymbol{v}$, $\boldsymbol{T}$. In A.8, the divergenceless vector parts derive from the divergenceless vector components and the scalar parts from the scalar components of the original variables; this is because $\nabla_i\,\Delta\, v^i = 0$ when $\boldsymbol{v}$ is divergenceless (as may be seen using A.5). Similarly, the divergenceless traceless tensor parts, the divergenceless vector parts, and the scalar parts of all the quantities in A.9 consist only of the corresponding components of the original variables, respectively, since $\nabla_i\,\Delta\, T^{ij} = 0$ when $\boldsymbol{T}$ is traceless and $\nabla_i\, T^{ij} = 0$ from A.6. This also holds for any linear combination of A.7$\sim$ A.8, so it is valid for any covariant linear differential equation of second order at most. This property then implies that the original equation is naturally decomposed into equations containing only one type of components, as v, $\boldsymbol{v}_v$ vanish if $\boldsymbol{v}$ vanishes and s, t, $\boldsymbol{T}_v$, $\boldsymbol{T}_t$ all vanish if $\boldsymbol{T}$ vanishes, as may be seen by inverting 2.7 and 2.9. □

Appendix B

Kerr metric terms and proofs

First of all, we transcribe the full expressions of the components of the Kerr metric in *Boyer-Lindquist* coordinates:

$$g_{tt} = -1 + \frac{2mr}{r^2 + a^2\cos^2\theta} \ , \tag{B.1}$$

$$g_{t\phi} = -\frac{2amr\sin^2\theta}{r^2 + a^2\cos^2\theta} \ , \tag{B.2}$$

$$g_{\phi\phi} = \sin^2\theta\left(a^2 + r^2 + \frac{2a^2mr\sin^2\theta}{r^2 + a^2\cos^2\theta}\right) \ . \tag{B.3}$$

For the inverse metric:

$$g^{tt} = -\frac{a^4 + 2r^4 + a^2r(2m+3r) + a^2\left(a^2 + r(-2m+r)\right)\cos 2\theta}{\left(a^2 + r(-2m+r)\right)\left(a^2 + 2r^2 + a^2\cos 2\theta\right)} \ , \tag{B.4}$$

$$g^{t\phi} = -\frac{4amr}{\left(a^2 + r(-2m+r)\right)\left(a^2 + 2r^2 + a^2\cos 2\theta\right)} \ , \tag{B.5}$$

$$g^{\phi\phi} = \frac{2\left(r(-2m+r) + a^2\cos\theta^2\right)\csc\theta^2}{\left(a^2 + r(-2m+r)\right)\left(a^2 + 2r^2 + a^2\cos 2\theta\right)} \ . \tag{B.6}$$

These may be of use when going through our calculations, and should be held at hand.

Let us show how to rewrite the constants of the motion L (angular momentum around z axis) and Q (Carter constant) used throughout Chapter 3 as functions of observable angles. Following[6], we look at 3.12 in the asymptotically flat region, i.e. taking the $a, m \to 0$ limit:

$$\hat{\dot{t}} = 1 \ , \quad \hat{\dot{r}} = \pm\frac{\sqrt{r^2 - \hat{Q} - \hat{L}^2}}{r} \ , \quad \hat{\dot{\theta}} = \pm\frac{\sqrt{\hat{Q} - \hat{L}^2\,\mathrm{ctan}^2\theta}}{r^2} \ , \quad \hat{\dot{\phi}} = \frac{\hat{L}}{r^2\sin^2\theta} \ . \tag{B.7}$$

The three Cartesian coordinates of the line (x, y, z) can be written as functions of the observable angles (ϑ, φ) and the reparametrised affine parameter $\hat{\lambda}$[1] as follows:

[1]Note: $\hat{\lambda}$ has dimension of length.

$$\begin{aligned} x\left(\hat{\lambda}\right) =& D_L + \left(\hat{\lambda} - \hat{\lambda}_O\right) \cos\vartheta \ , \\ y\left(\hat{\lambda}\right) =& -\left(\hat{\lambda} - \hat{\lambda}_O\right) \sin\vartheta \cos\varphi \ , \\ z\left(\hat{\lambda}\right) =& -\left(\hat{\lambda} - \hat{\lambda}_O\right) \sin\vartheta \sin\varphi \ , \end{aligned} \tag{B.8}$$

where $\hat{\lambda}_O$ is the value of the affine parameter at the position of the observer. This means that the affine parameter has domain

$$\hat{\lambda}_O - \frac{D_L}{\cos\vartheta} \leq \hat{\lambda} \leq \hat{\lambda}_O \ .$$

We convert to the spherical coordinates (r, ζ, ϕ) used in Chapter 3, and write down coordinates and coordinate velocities:

$$\begin{aligned} r\left(\hat{\lambda}\right) &= \sqrt{D_L^2 + (\hat{\lambda} - \hat{\lambda}_O)^2 + 2\, D_L \left(\hat{\lambda} - \hat{\lambda}_O\right) \cos\vartheta} \\ \zeta\left(\hat{\lambda}\right) &= \sin^{-1}\left(\frac{z\left(\hat{\lambda}\right)}{r\left(\hat{\lambda}\right)}\right) \ , \\ \phi\left(\hat{\lambda}\right) &= \tan^{-1}\left(\frac{y\left(\hat{\lambda}\right)}{x\left(\hat{\lambda}\right)}\right) \ ; \end{aligned} \tag{B.9}$$

$$\begin{aligned} \hat{\dot{r}}\left(\hat{\lambda}\right) &= \frac{\left(\hat{\lambda} - \hat{\lambda}_O\right) + D_L \cos\vartheta}{r} \ , \\ \hat{\dot{\phi}}\left(\hat{\lambda}\right) &= -\frac{D_L \cos\varphi \sin\vartheta}{D_L^2 + 2D_L(\lambda - \lambda_O)\cos\vartheta + (\lambda - \lambda_O)^2\cos^2\vartheta + (\lambda - \lambda_O)^2\cos^2\varphi\sin^2\vartheta} \ . \end{aligned} \tag{B.10}$$

We evaluate the values of these at the observer's position:

$$r\left(\hat{\lambda}_O\right) = D_L \ , \qquad \zeta\left(\hat{\lambda}_O\right) = 0 \ , \qquad \hat{\dot{r}}\left(\hat{\lambda}_O\right) = \cos\vartheta \ , \qquad \hat{\dot{\phi}}\left(\hat{\lambda}_O\right) = -\frac{\sin\vartheta\cos\varphi}{D_L} \ . \tag{B.11}$$

Then, we calculate $\hat{L}$ and $\hat{Q}$ at $\hat{\lambda} = \hat{\lambda}_O$ by substituting B.11 into B.7; remember, $\hat{L}$ and $\hat{Q}$ are constants of the motion and as such are the same at any λ. We get

$$\hat{L} = \hat{\dot{\phi}}\, r^2 \cos^2\zeta \Big|_{\hat{\lambda}=\hat{\lambda}_O} = -D_L \sin\vartheta \cos\varphi \ , \tag{B.12}$$

$$\hat{Q} = \left[r^2\left(1 - \hat{\dot{r}}^2\right)\right]\Big|_{\hat{\lambda}=\hat{\lambda}_O} = D_L^2 \sin^2\vartheta \sin^2\varphi \ . \tag{B.13}$$

These are the expressions for the two constants of motion used throughout Chapter 3.

Let us now hint at how to derive the Kerr lens equation, for equatorial observers. We could just as well express Q and L in terms of the light ray at the position of the source: L_s and Q_s. The position of the source with respect to the black hole is pinpointed

by the angles ($\mathcal{B}$, $\mathcal{X}$), and the direction of the light ray at the source is defined by (ϑ_s, φ_s). Then the three Cartesian components of the light ray at the source are

$$x\left(\hat{\lambda}\right) = -\,D_{LS} + \left(\hat{\lambda} - \hat{\lambda}_s\right)\cos\,\vartheta_s\ , \tag{B.14}$$

$$y\left(\hat{\lambda}\right) = D_S\,\tan\,\mathcal{B}\,\cos\,\mathcal{X} - \left(\hat{\lambda} - \hat{\lambda}_s\right)\sin\,\vartheta_s\,\cos\,\varphi_s\ , \tag{B.15}$$

$$z\left(\hat{\lambda}\right) = D_S\,\tan\,\mathcal{B}\,\sin\,\mathcal{X} - \left(\hat{\lambda} - \hat{\lambda}_s\right)\sin\,\vartheta_s\,\sin\,\varphi_s\ , \tag{B.16}$$

where $\hat{\lambda}_s$ is the value of the affine parameter at the source position. Thus the affine parameter range for the line segment is

$$\hat{\lambda}_s \leq \hat{\lambda} \leq \hat{\lambda}_s + \frac{D_{LS}}{\cos\,\vartheta_s}\ .$$

Repeating the same procedure as before, we obtain

$$\begin{aligned}
\hat{L}_s =& -\,D_S\,\tan\,\mathcal{B}\,\cos\,\mathcal{X}\,\cos\,\vartheta_s + D_{LS}\,\sin\,\vartheta_s\,\cos\,\varphi_s\ ,\\
\hat{Q}_s =& D_S^2\left(\tan\,\mathcal{B}\,\sin\,\mathcal{X}\right)^2\left(\cos^2\,\vartheta_s + \sin^2\,\vartheta_s\,\cos^2\,\varphi_s\right) +\\
&-\,2\,D_S\,\tan\,\mathcal{B}\,\sin\,\mathcal{X}\,\sin\,\vartheta_s\,\sin\varphi_s\left(D_{LS}\,\cos\,\vartheta_s + D_S\,\tan\,\mathcal{B}\,\cos\,\mathcal{X}\,\sin\,\vartheta_s\,\cos\,\varphi_s\right) +\\
&+\left(D_S^2\left(\tan\,\mathcal{B}\,\cos\,\mathcal{X}\right)^2 + D_{LS}^2\right)\sin^2\,\vartheta_s\,\sin^2\,\varphi_s\ .
\end{aligned} \tag{B.17}$$

As they are constants of the motion, $\hat{L}_s \equiv \hat{L}$ and $\hat{Q}_s \equiv \hat{Q}$ from equations B.12 and B.13. These conditions provide a quadratic equation in $\tan\,\mathcal{B}\,\sin\,\mathcal{X}$, which yields

$$\begin{aligned}
\tan\,\mathcal{B}\,\cos\,\mathcal{X} =& \frac{D_{LS}\,\tan\,\vartheta_s\,\sin\,\varphi_s}{D_S} + \frac{D_L\,\sin\,\vartheta}{D_S\,\left(1 - \sin^2\,\vartheta_s\,\sin^2\,\varphi_s\right)}\cdot\\
&\cdot\left[\cos\,\varphi\,\sin\,\vartheta_s\,\tan\,\vartheta_s\,\sin\varphi_s\,\cos\,\varphi_s \pm \sqrt{\sin^2\,\varphi - \sin^2\,\vartheta_s\,\sin^2\,\varphi_s}\right]\ .
\end{aligned} \tag{B.18}$$

We take the positive root as in the case of spherical symmetry only the positive root will return the Schwarzschild case when $\varphi \equiv \varphi_s$. This may be rearranged to obtain the lens equation in the Kerr case, much in the same way as we obtained the lens equation for Schwarzschild.

Appendix C

A little more about Kerr geometry

In Chapter 3, we analyse the geodesics of the Kerr metric but we don't give a detailed description of a Kerr black hole, as it is not our object of study. It is instructive however to fully understand the geometry of this type of object, and specifically what happens mathematically close to the origin.

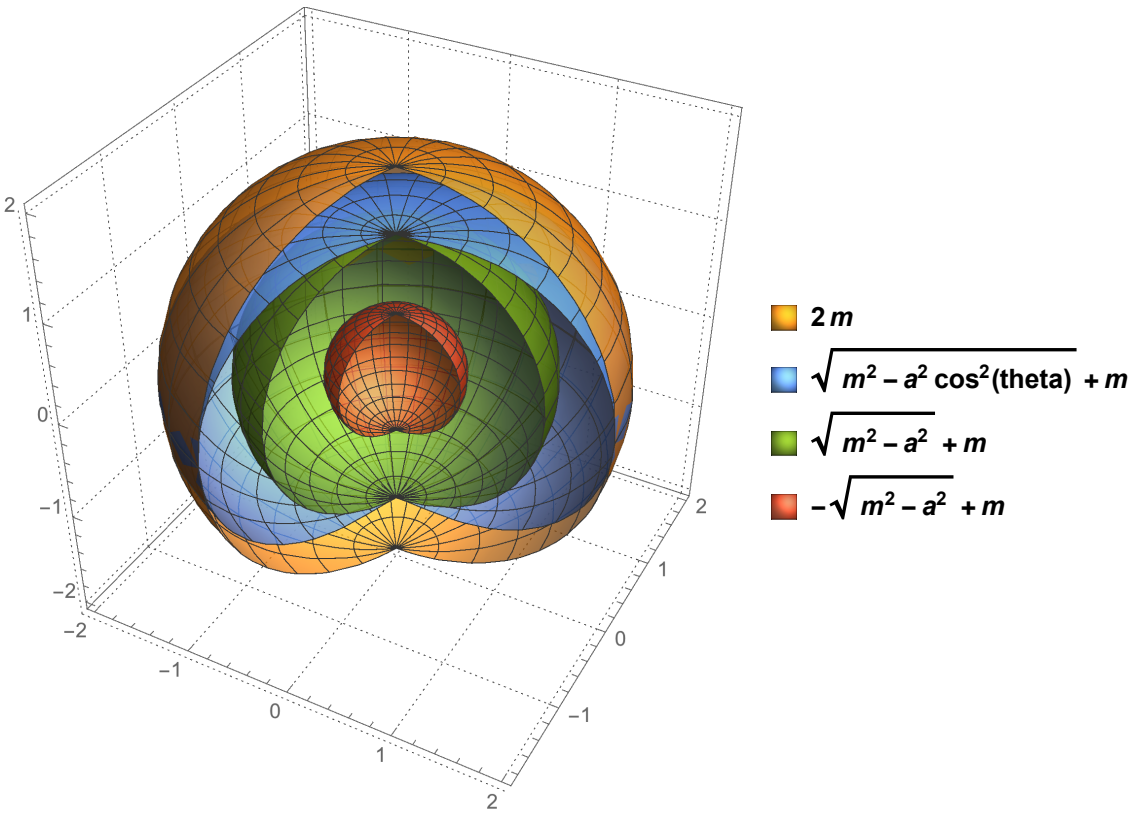

Figure C.1: An illustration of the interesting surfaces in the Kerr metric; dummy values of m and a have been chosen. Note that $r_+ < 2\,m$, so it is perfectly justified to consider the limit $b \gg r_s \equiv 2\,m$ in our calculations.

As previously mentioned, the Kerr metric presents 2 coordinate singularities,

$$r_{\pm} = m \pm \sqrt{m^2 - a^2} \ ,$$

which are called the inner $(-)$ and outer $(+)$ horizons. Although these are fixed radii, when inputting them in the metric 3.2 one does not get the metric on the 2-sphere; we represent them as spheres anyway in Figure C.1 for descriptive purposes.
There is another interesting value of r, which is θ-dependent: $r_e = m + \sqrt{m^2 - a^2 \cos^2\theta}$. At $r = r_e$, the time killing vector k_t^μ (recall it from 3.5) changes nature: at $r > r_e$ it is time-like, at $r < r_e$ space-like. The region within r_e, where k_t^μ is space-like, is called the ergoregion and is physically very interesting, as its features enable the Penrose process [36].
It's also worth to mention that the inner horizon r_- is effectively considered of scarce physical interest, since as $r \to r_-$ perturbations are infinitely blueshifted, which leads to divergences in the curvature scalars [37].

All these interesting features of the Kerr metric pertain to a region of space $r < 2\,m$, which we can consider to be the Schwarzschild radius associated to the Kerr black hole (it has no physical meaning in itself, but it's an easy reference parameter). In short, they have no effect on the phenomena we've described, as we've operated in the $b \gg 2\,m$ limit.

Bibliography

[1] S. Carroll, "Spacetime and Geometry: An Introduction to General Relativity", Pearson, 2004.

[2] A. Zee, "Einstein Gravity in a Nutshell", 2013.

[3] C. R. Keeton and A. O. Petters, "Formalism for testing theories of gravity using lensing by compact objects: Static, spherically symmetric case", *Physical Review D* **72** nov (2005) 104006, arXiv:0511019.

[4] R. M. Wald, "General Relativity", University of Chicago Press, 1984.

[5] S. V. Iyer and E. C. Hansen, "Strong and Weak Deflection of Light in the Equatorial Plane of a Kerr Black Hole", 0908.0085.

[6] A. B. Aazami, C. R. Keeton, and A. O. Petters, "Lensing by Kerr black holes. I. General lens equation and magnification formula", *Journal of Mathematical Physics* **52** feb (2011) 092502, 1102.4300.

[7] V. Bozza, "Comparison of approximate gravitational lens equations and a proposal for an improved new one", *Physical Review D* **78** nov (2008) 103005, 0807.3872.

[8] M. Bartelmann and P. Schneider, "Weak gravitational lensing", *Physics Reports* **340** jan (2001) 291–472, arXiv:9912508.

[9] M. Meneghetti, "Introduction to Gravitational Lensing", tech. rep., 2006.

[10] A. Heavens, "Cosmology with Gravitational Lensing", 1109.1121.

[11] D. B. Thomas, C. R. Contaldi, and J. Magueijo, "Rotation of galaxies as a signature of cosmic strings in weak lensing surveys.", *Physical review letters* **103** oct (2009) 181301, 0909.2866.

[12] M. Bartelmann, "Gravitational Lensing", arXiv:1010.3829.

[13] L. Van Waerbeke and Y. Mellier, "Gravitational Lensing by Large Scale Structures: A Review", arXiv:0305089.

[14] H. Kodama and M. Sasaki, "Cosmological Perturbation Theory", *Progress of Theoretical Physics Supplement* **78** aug (1984) 1–166, 10.1143/PTPS.78.1.

[15] S. Weinberg, "Cosmology", 2008.

[16] R. Durrer, "Cosmological perturbation theory", *arXiv:astro-ph/0402129* **i** (2004) 77–100, arXiv:0112551v1.

[17] C. R. Contaldi, "Cosmology", 2000.

[18] N. Y. Vilenkin and Y. A. Smorodinsky, "Harmonic Function Expantions", *Sov. Phys.* **19** (1964) 1209.

[19] A. Stebbins, "Cosmic Strings and the Microwave Sky .1. Anisotropy from Moving Strings", *Astrophysical Journal* **327** (1988), no. 2, 584–614, 10.1086/166218.

[20] M. Visser, "The Kerr spacetime: A brief introduction", 0706.0622.

[21] L. Gualtieri and V. Ferrari, "BLACK HOLES IN GENERAL RELATIVITY", Universita' degli studi di Roma "Sapienza", 2011.

[22] R. H. Boyer and R. W. Lindquist, "Maximal Analytic Extension of the Kerr Metric.", *J. Math. Phys.*, 1967.

[23] R. C. Henry, "Kretschmann Scalar for a Kerr Newman Black Hole", *The Astrophysical Journal* **535** may (2000) 350–353, arXiv:9912320.

[24] M. Visser and S. M. Scott, "The Kerr Spacetime, Part 4", Victoria University of Wellington, 2009.

[25] O. James, E. von Tunzelmann, P. Franklin, and K. S. Thorne, "Gravitational lensing by spinning black holes in astrophysics, and in the movie Interstellar", *Classical and Quantum Gravity* **32** mar (2015) 065001, 1502.03808.

[26] A. B. Aazami, C. R. Keeton, and A. O. Petters, "Lensing by Kerr black holes. II: Analytical study of quasi-equatorial lensing observables", *Journal of Mathematical Physics* **52** feb (2011) 102501, 1102.4304.

[27] A. Stebbins, "Weak Lensing On the Celestial Sphere", arXiv:9609149.

[28] U.-L. Pen and S. Mao, "Rotation in gravitational lenses", *Monthly Notices of the Royal Astronomical Society* **367** apr (2006) 1543–1550, arXiv:0506053.

[29] H. Sigurdarson, "Gravitational lensing by galaxy clusters", 2010.

[30] J. Binney and S. Tremaine, "Galactic Dynamics", 1950.

[31] ESA, "Planck Mission Objectives", 2013. *link*→

[32] ESA, "Euclid Mission Status", 2015. *link*→

[33] W. Gressler, "LSST Optical Design Summary", 2009. *link*→

[34] R. Laureijs, J. Amiaux, S. Arduini, et al., "Mapping the geometry of the dark Universe", *Esa/Sre 2*, 2009, no. July, arXiv:0912.0914.

[35] D. Munshi, P. Valageas, L. van Waerbeke, and A. Heavens, "Cosmology with weak lensing surveys", *Physics Reports* **462** (2008), no. 3, 67–121, arXiv:0612667.

[36] M. Bhat, S. Dhurandhar, and N. Dadhich, "Energetics of the Kerr-Newman black hole by the penrose process", *Journal of Astrophysics and Astronomy* **6** (1985), no. 2, 85–100. 0250-6335

[37] F. Dowker, "Black Holes Lectures", 2014.